Red blood cells under flow: blood rheology and effect of vascular endothelial cells on haemodynamics *in vitro*

Ing. Antonio Carciati

PhD in Industrial Production and Process Engineering - XXIX Cycle

Dipartimento di Ingegneria Chimica, dei Materiali e
della Produzione Industriale
Università degli studi di Napoli Federico II

Tutor
Prof. Stefano Guido

Co-Tutor
Ing. Giovanna Tomaiuolo

May 2017

... the essence of our life is ultimately not blood
but the fluidity of blood.

Zamir, Haemodynamics

Contents

List of Figures

Abbreviation

ACD	Acid citrate dextrose solution
CLSM	Confocal laser scanning microscope
DNA	Deoxyribonucleic acid
ECGM	Endothelial cell growth medium
G’	Elastic modulus
G’’	Viscous modulus
GCX	Glycocalyx
hRBC	Healthy red blood cells
Htc	Haematocrit
HUVEC	Human umbilical vein endothelial cells
ID	Inner diameter
iRBC	Infected red blood cells
mRNA	Messenger ribonucleic acid
Oligos	Oligonucleotides
PBS	Phosphate buffered saline
RBC	Red blood cells
Re	Reynolds number
RI	Refractive index
RPM	Rotation per minutes
SA	Sialic acid
SI	Shape index
Tan δ	Loss tangent
WGA	Wheat germ agglutinin

Abstract

Understanding rheological properties and flow behavior of human blood is the object of a large body of literature related to both biomedical and clinical field of cardiovascular disorders as well as to the development of microfluidic platforms for blood testing. Hemorheology and haemodynamics are the areas of research related to these topics. The former deals with all the aspects of the flow properties of blood via classical bulk rheology testing while the latter investigates the relationship among physical properties influencing blood flow through the vessels (i.e. flow rate, shear stress, vessel architecture, driving pressure). Although hemorheology and haemodynamics seem to have the potential to describe complex physiological phenomena, there is still uncertainty regarding the exact applicability to specific issues. For example, the rheological characterization by common rheological protocols of a complex biological fluid such as human blood is a difficult task, especially the investigation of viscoelastic properties. Furthermore, the experiments on blood fluid dynamic *in vitro* might be unreliable due to the differences between the micro-environment present *in vivo* and the simplified conditions typical of *in vitro* systems.

Human blood shows unusual, and for certain aspects, unique properties: it is a concentrated suspension of cells among which red blood cells (RBC or erythrocytes) dominate in terms of number over the others (i.e. white blood cells and platelets). Furthermore, RBC are highly deformable cells and tend to aggregate reversibly under static or very slow flow rates. From a rheological point of view, blood mechanical response to continuous stress, i.e. shear thinning and yield stress, are strictly related to RBC peculiar features. Moreover, blood is also a time-dependent material and presents viscoelastic properties

Here, an extensive rheological characterization under both continuous and oscillatory conditions is presented, demonstrating that human blood shows a peculiar viscoelastic behavior. In particular, the viscous character prevails over the elastic one even if the latter gives a significant contribution to the mechanical spectra. In addition, the effects of increasing RBC volume fraction and of the addition of dextran, an aggregating agent, has been studied, showing a gel-like response.

Regarding haemodynamics, blood flow in human body shows uncommon phenomena compared to other fluids, such as the Fahraeus effect, axial migration of RBC, etc. Literature papers focus on the study of blood flow by using *in vitro* models able to mimic the *in vivo* conditions of the human vascular system. The microfluidic paradigm has been mostly used to resemble human microvasculature, either analyzing blood flow behavior under microconfined conditions or studying the effect of flow on endothelial cells lining microchannel walls. However, both the approaches present some limits: in the first case, the endothelial contribution and its interaction with blood cells are lacking, whereas in the second case, although channels are lined with endothelial cells, there is no blood flow but only cell culture medium flow. Moreover, the properties

and the role of endothelial glycocalyx (GCX), a negatively charged hairy layer of proteoglycans and glycoproteins located on the inner surface of the vascular endothelium, is far from being fully elucidated. Thus, none of the strategies can be considered as reliable models of *in vivo* microcirculation, and discrepancies between *in vitro* studies and physiological conditions have been observed. In this work, the two approaches have been coupled, allowing the study of blood flow in microchannels lined with endothelial cells, including the GCX to better model real microvasculature. Microchannels dimensions and flow conditions have been chosen to mimic big arterioles and venules regions. Velocity profiles of RBC in endothelialized microchannel have been compared with bare ones, suggesting a marginal role of the endothelial layer. Moreover, the electronegativity of endothelial GCX seems not to influence RBC flow. A case study that uses the mentioned approach is addressed to the analysis of malaria infected RBC by *Plasmodium falciparum* parasite. Indeed, the pathogenicity of *Plasmodium* parasite results from its ability to adhere to endothelium during its life cycle, preventing removal by the spleen. Preliminary results regarding dynamics of a single RBC are in good agreement with previous numerical simulation works, while the cytoadhesion has shown that both healthy and infected RBC adhere on endothelial cells.

These findings could be useful for the understanding of the human blood flow behavior. In particular, viscoelastic characterization could help in elucidating the role of hemorheological alteration in pathologies such as myocardial infarction, hypertension, and diabetes. On the other hand, RBC-endothelial cell flow assay can serve as starting point to design blood-on-chip platforms aimed to study drug transport in blood stream.

1. Introduction

In this chapter, a general overview of the main contents of the thesis is reported, highlighting important results present in the literature, in order to allow a better understanding of chapters 2, 3, 4.

First of all, the main hemorheological properties are discussed, focusing on the aggregation of RBC and on the viscoelasticity of blood. Then, a brief presentation of the flow behavior of human blood through the vessels is presented. In particular, blood flow in human body and *in vitro* models are discussed.

1.1 Human blood

Blood is the most important biological fluid in the human body. Under physiological conditions, blood consists of a concentrated suspension of cells, called corpuscles or formed elements, divided into RBC, white blood cells and platelets, immersed in a water-based fluid called plasma. The latter contains 92% of water and several solutes such as proteins (mainly fibrinogen, cholesterol, albumins, and globulins), and electrolytes (Figure 1.1A). Blood is defined as a fluid connective tissue, specialized in performing many important functions within the body, such as transporting oxygen, nutrients and hormones to cells and tissues all over the body, removing waste, regulation of body pH and temperature, and coagulation [1].

Due to their predominant presence and special features, RBC rule properties and fluid dynamic of blood, RBC volume percentage in blood (called hematocrit - Htc) typically varying between 40-50%. Erythrocytes are nucleus-free cells and, in health and if not subjected to external stress, present a biconcave disc shape with a diameter of 6-8 μm, thickness of 2 μm, and mean corpuscular volume ranging from 80 to 100 μm^3. The cell membrane can be related as a composite material consisting of a phospholipid bilayer and an underlying two-dimensional network of spectrin molecules which serves as the membrane skeleton. At the interface membrane-environment, a coating of glycolipids and glycoproteins, called glycocalyx (i.e. GCX) protrudes from the membrane surface (Figure 1.1B).

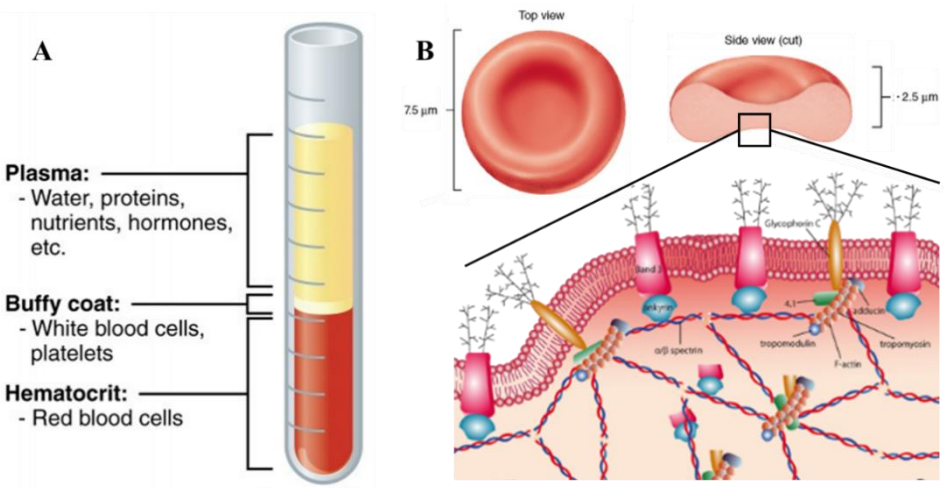

Figure 1.1 - (A) Human blood composition; (B) Erythrocyte morphology and membrane structure

1.2 Hemorheology

Hemorheology [2] is the branch of rheology that focuses on the study of the flow properties of blood. It is becoming an issue of growing interest, for both research and clinic field, for blood storage [3, 4], for industrial biotechnologies (e.g. in the formulation of fluids of biological interest [5]), and in the design of diagnostic devices [6].

Blood flow behavior has been long recognized as a fundamental problem in physiology and biomechanics and a number of works describe in detail the macrorheological behavior of human blood [2, 7, 8]. In general, blood can be defined in several ways: as a two-phase liquid, as a solid-liquid suspension, where the formed elements represent the solid phase, and as a liquid-liquid aggregating emulsion, considering the high deformability and aggregability of RBC under shear [2]. It has been widely demonstrated that erythrocytes exert the most significant influence on the mechanical properties of blood, mainly due to their high concentration compared to the other formed elements. Thus, human blood can be seen as a non-Newtonian, viscoelastic fluid, in which RBC behave as neutrally buoyant, aggregating microcapsules with high deformability but small area stretchability [9] suspended in plasma.

At a fixed value of temperature and shear rate, the rheological properties of the blood are determined by the characteristics of the plasma and the cellular phase, as well as aggregation and deformability of RBC. In particular, plasma viscosity affects directly whole blood viscosity, and alterations of normal values are common in acute or chronic disease or in tissue lesions. Plasma acts as a Newtonian fluid in shear flow measurement, while it shows a viscoelastic behavior under uniaxial extensional flow [10]. Its viscosity ranges from 1.16 to 1.35 cP in physiological condition, exponentially decreasing with temperature [11]. Regarding RBC volume fraction (Hct), it is the major determinant of blood viscosity. In general, bi-phasic systems present viscosity that increases with the volume fraction of the particles dispersed in the matrix, although the relationship differs between one system to another (Figure 1.2). Blood viscosity increases exponentially

with Htc up to 99% whereas a suspension of rigid spheres at 50% in the same conditions is not able to flow.

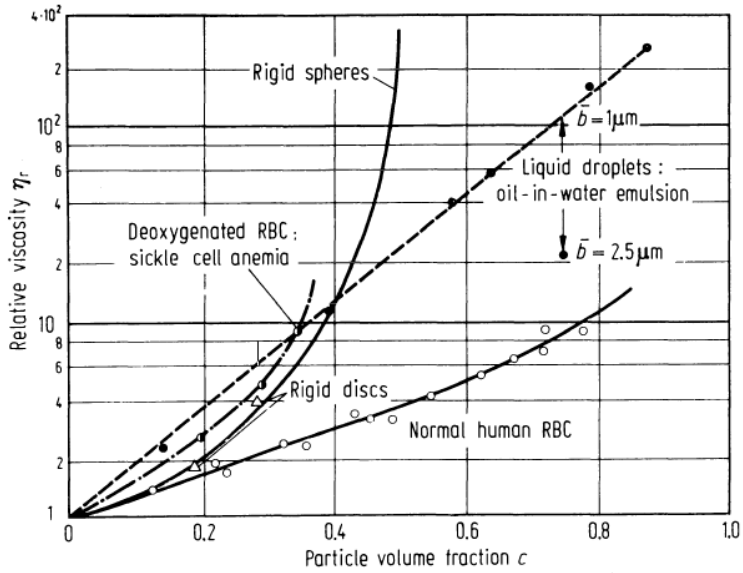

Figure 1.2 - Relative viscosity as a function of volume fraction of normal human RBC compared to that of suspensions of rigid latex spheres, rigid disks, droplets [12]

RBC aggregability reflects the intrinsic tendency of RBC to form aggregates. The presence of some plasma proteins, in particular fibrinogen and globulins, makes RBC capable to adhere one to each other to form rod-shaped stacks of individual cells called rouleaux. Conversely, RBC aggregation does not occur in simple salt solutions. One of the most important features for rouleaux formation is the typical biconcave disk-shape, which is considered a prerequisite for aggregation process. Electron microscopic investigations showed the existence of an intercellular space of about 25 nm between two RBC, and the almost constant interfacial distance was associated with a deformation of the cell surfaces [13] (Figure 1.3). Changes of RBC shape lead to alteration of physiological aggregation behavior [14]. In static conditions and at very low shear rate, rouleaux can interact among them to form secondary structure of branched three-dimensional aggregates. This phenomenon is driven by the interplay between aggregating and disaggregating forces. The factors affecting RBC aggregation can be divided into intrinsic (i.e. Htc, shear rate and amount of plasma proteins) and extrinsic (i.e. RBC shape, deformability and membrane surface properties).

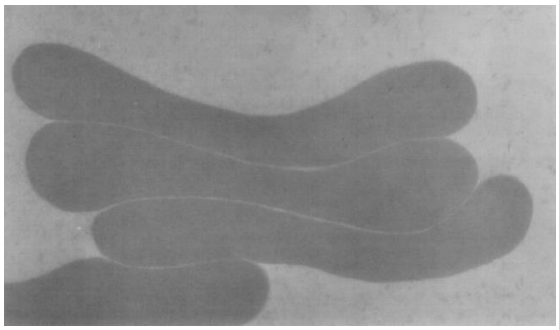

Figure 1.3 - Transmission electron micrograph of a rouleau in plasma [13]

Several macromolecules are capable of inducing RBC aggregation, including, various polymers and plasma proteins [14, 15]. Fibrinogen is the most important protein involved in RBC aggregation mechanism. It is a glycoprotein synthesized by the liver with a molecular mass of 340 kDa that binds specifically RBC. The physiological concentration in plasma is 150-300 mg/dl, but higher levels have been measured in cardiovascular disease and during inflammation states. Fibrinogen affects directly RBC aggregation and hence hemorheological parameters (e.g. yield stress, blood viscosity, and RBC sedimentation rate). In addition, other large plasma proteins are involved in RBC aggregation process, although there are contradictory results regarding their influence [14, 16, 17] (Figure 1.4). It should be considered that such proteins could interact one to each other, resulting in unpredictable effects [18]; a synergistic effect of fibrinogen and albumin has been observed resulting in an enhancement of the aggregation process [19].

Plasma Protein	M_m (kDa)	Plasma concentration (mg/ml)	Effects on Aggregation
Fibrinogen	340	1.5–3.0	↑
Immunoglobulin G	150	8	↑, no effect
Immunoglobulin M	900	1.5	↑
C-reactive protein	25	<0.01	↑
Transferrin	80	2.0–3.6	no effect
Haptoglobin	38	0.5–2.5	↑, no effect
Ceruloplasmin	151	0.2–0.4	no effect
α_1-acid glycoprotein	40	0.5–1.0	↑, no effect
Albumin	66	20–50	↓,↑, no effect

Figure 1.4 - Effect of some plasma proteins on RBC aggregation [14]

The tendency of RBC to aggregate can also be enhanced by the addition of various polymers and macromolecules such as gelatin, ficoll, starches, poly(ethylene glycol) (PEG), polyvinylpyrrolidone (PVP), and dextran [14]. The latter belongs to a group of glucose neutral polymers made by certain bacteria and it is widely used as model macromolecules for RBC aggregation studies [20]. Moreover, it is worth to mention that the interaction energy between cells depends not only on fibrinogen or dextran concentration, but also on the molecular weight of such macromolecules [21]. The mechanism at the base of RBC aggregation is controversial and not yet fully elucidated.

Besides attractive forces, electrostatic repulsive forces are present while Van der Walls forces are neglected. Two main models have been proposed to describe RBC aggregation both related to the presence of macromolecules, based on bridging and depletion, respectively. The bridging model assumes that macromolecules act as a bridge between two adjacent RBC; in fact aggregation occurs when the adsorption of the macromolecules generates bridging forces that exceed disaggregating forces due to electrostatic repulsion, mechanical shearing, and membrane strain (Figure 1.5A). It has been observed that the intercellular distance between adjacent cells is less than the size of the hydrated molecules, suggesting that the terminal portions of the polymers are adsorbed on the cell surface. Moreover, Chien has demonstrated that cell-cell separation distance increases with polymer size [22]. On the other hand, in the depletion model the presence of macromolecules in the suspending medium induces a gradient of osmotic pressure, leading to depletion interaction [20, 23, 24] (Figure 1.5B). The disaggregation forces are the same of the bridging model. These models are in disagree about the nature of the aggregating forces between RBC, and hence they are considered as exclusive. Even though the validity of the models has been the topic of long controversies, the most credited one, which presents recent experimental validations, is the depletion model [20, 23-25].

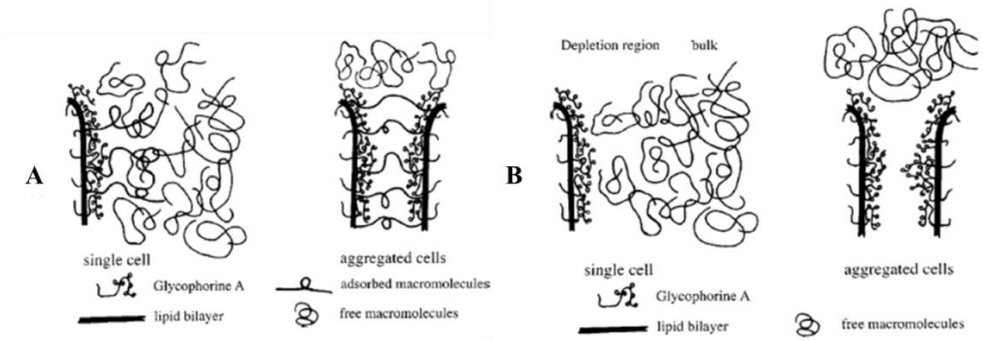

Figure 1.5 - Schematic drawing of the models. (A) Bridging model; (B) Depletion model. Re-adapted from [24]

The depletion concept was pioneered by Asakura and Osawa [26] and it is applied in general to the field of colloid chemistry [27]. Several previous reports have investigated the depletion mechanism from both experimental and theoretical point of view [23, 28]. Since RBC surface is characterized by the presence of a soft surface (i.e. GCX) that can be penetrated by the free macromolecules in the solution, for two RBC at a distance d, a GCX thickness δ, a depletion layer thickness D, and a penetration of the polymer into the GCX p, the depletion interaction energy w_D can be approximated by:

$$W_D = -2\Pi(\Delta - \frac{d}{2} + \delta - \mathrm{p}) \qquad \textit{Equation 1}$$

when $\left(\frac{d}{2} + \delta - \mathrm{p}\right) \leq \Delta$, and is zero when $\left(\frac{d}{2} + \delta - \mathrm{p}\right) > \Delta$ [28].

These models lead to two different dynamics of rouleaux formation. In the case of bridging model, the free end of the macromolecules adsorbed on one cell surface can adsorb onto the adjacent RBC, leading to their cross-link (Figure 1.6I). Such effect is

possible only if the distance between cells is far enough to minimize electrical repulsion. Subsequently, further bridges are formed when cells are in close proximity. Deformability plays a key role in this process; in fact, the surface area in close contact is maximized through cell deformation (Figure 1.6II) leading to an increasing in bridges formation (Figure 1.6III) [13, 14].

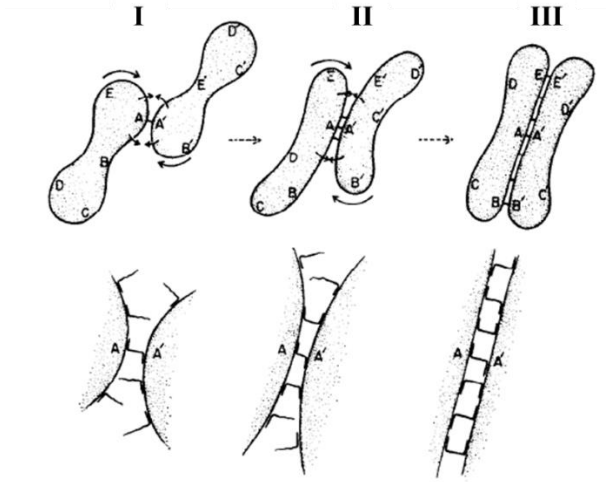

Figure 1.6 - Illustration of the dynamics of rouleau formation in the bridging model [13]

Regarding depletion model, a depletion layer could be formed near cell surface when the loss of configuration entropy of macromolecules at the surface is not balanced by adsorption energy (Figure 1.7I). The depletion layer leads to the displacement of solvent into the bulk phase (grey arrow in Figure 1.7) due to the osmotic pressure difference between the intercellular polymer-poor depletion zone and the bulk phase. So adjacent cells slide along each other in order to maximize the contact area and thus the loss in free energy (black arrows in Figure 1.7). The result is the rouleaux formation (Figure 1.7III). In contrast to the bridging model, rouleaux formation via depletion does not require cell deformations since adjacent RBC can slide one along each other [14].

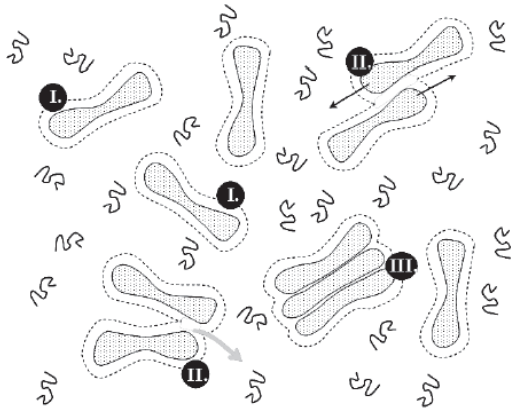

Figure 1.7 - Illustration of the dynamics of rouleau formation in the depletion model [14]

RBC deformability refers to the ability of RBC to recover their discoid shape and it is crucial for flowing through capillaries with diameters smaller than their size at rest, thus guaranteeing optimal gas exchange between blood and tissues [29] (Figure 1.8). The high flexibility and deformability of RBC are due to three characteristics [30]: (i) their fluid-filled bag-like structure has large surface area-to-volume ratio. In fact, the excess surface area is 40% larger than the area of a sphere having the same volume [30]. The biconcave shape of a RBC presents a mean surface area (~135 μm^2) significantly greater than the surface area of a sphere enclosing the same volume (~90 fl) [31]; (ii) inside the cells, a concentrated hemoglobin solution behaves as an incompressible viscous fluid. The intracellular fluid viscosity is 6-7 mPa·s; (iii) the viscoelastic properties of the cell membrane, a composite structure made of an external layer (GCX), a lipid bilayer capable of resisting bending, and a membrane skeleton composed of a protein network located on the inner surface of the lipid bilayer [32, 33]. RBC morphological changes have been observed both *in vivo* [34] and *in vitro* [29, 35]. Pathological alterations are associated with reduced RBC deformation such as malaria [36], hereditary disorders [37], and myocardial infarction [38].

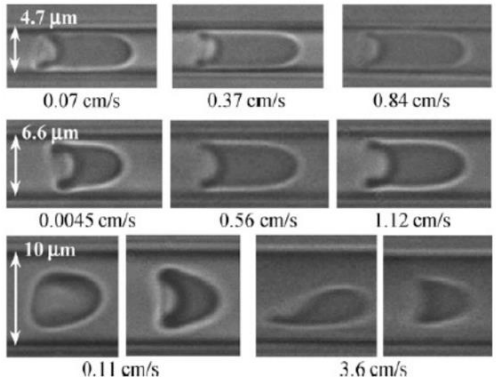

Figure 1.8 - Image of RBC flowing in microcapillaries. Re-adapted from [29]

In summary, the unique characteristics of RBC and their interactions result in a complex rheological response which is reflected in the whole blood shear thinning behavior [7], the presence of a yield stress value [39-41], viscoelasticity properties [9, 42], and memory effects (i.e. thixotropy) [43, 44]. These phenomena depend on the magnitude of the applied deformation and therefore may be present or strengthened in some flow regimes such as at low shear rates; non-Newtonian character is also influenced by the type of deformation (shear or elongation) [45].

The formation and breakup of RBC aggregates at rest and under very weak flow fields, as well as the deformation and recovery of cell shape, lead to shear thinning behavior of whole blood. At rest, blood exhibits a solid-like structure which reflects the viscosity values of about one hundred times higher compared to water. Such structures can be broken into three-dimensional networks of various sizes by the action of a flow field and each network is able to move as individual units reaching an equilibrium size for a fixed shear rate [44]. Chien [46] demonstrated that the average length of RBC aggregates decreases with increasing shear rate, until their disappearance, resulting in viscosity decreasing. Shear rates values between 1 and 100 s^{-1} prevent aggregates

formation as well as induce deformation and orientation of RBC. At very high flow velocities, RBC are dispersed and aligned in the direction of flow; viscosity of blood decreases by two orders of magnitude until 4-5 mPa·s (Figure 1.9). In order to understand the behavior of blood under flow, the combined effects of aggregation and deformation of RBC is not sufficient. It has been demonstrated that the dynamics of individual cells in flow are linked to bulk viscosity of blood. In fact, Forsyth et al. [47] report that shear thinning is due to tumbling-to-tank treading transition, whereas deformation plays a marginal role. Recently, Lanotte et al. [48] show that blood shear thinning is governed by RBC dynamic; in detail they found that increasing shear rate induces RBC to tumble, roll, deform into stomatocytes, and finally, adopt highly deformed polylobed shapes.

Moreover, it has been also observed that by stiffening the RBC or removing proteins responsible for the aggregation, whole blood viscosity at low shear rates is lower than that in physiological conditions. The deformability of erythrocytes allows them to align with the flow at high values of shear rate, reducing the viscosity. Suspension of hardened RBC behaves as a Newtonian fluid, but with a viscosity up to 100 times higher than that of the untreated blood [46]. Instead, aggregation contribution is significant only at very low shear rate. Figure 1.9 resumes how RBC properties influence blood rheology under steady-state shear flow.

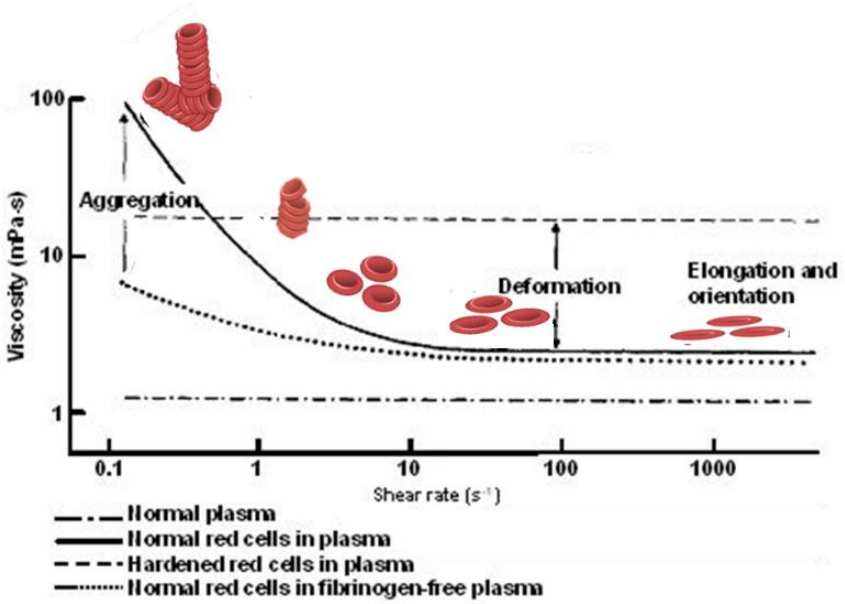

Figure 1.9 - Influence of RBC properties on blood viscosity at different shear rates. Re-adapted from [2]

The presence of a microstructure, although weak, can be related to a yield stress, i.e. the applied stress needed to initiate flow. Yield stress can be seen as the manifestation of attractive forces between particles suspended in a continuous medium. These forces lead to the formation of a network in the absence of flow, but are weak enough to allow network disruption following the application of an adequate stress [41]. Whole blood yield stress ranges from 3 to 5 mPa [11] and, in physiological conditions, it is a function

of fibrinogen concentration and Htc [49, 50]. In order to measure blood yield stress experimentally, two approaches have been mostly used: (i) direct methods, where the shear stress at which blood starts flowing is measured and (ii) indirect methods by using a constitutive model or linear fitting [9]. In particular, the most frequently used model for describing blood flow is the Casson model [51] given by:

$$\tau^{1/2} = (k\dot{\gamma})^{1/2} + \tau_y^{1/2} \qquad \textit{Equation 2}$$

where τ is the shear stress, $\dot{\gamma}$ is the shear rate, k is the Casson model constant, and τ_y is the yield shear stress. Note that when the yield stress τ_y vanishes, Equation 2 reduces to the constitutive equation of a Newtonian liquid. In order to extrapolate the yield stress, viscosity data should be rearranged in the so-called "Casson plot", i.e. square root of shear rate and shear stress. Subsequently, straight lines obtained via linear regression with their intercepts being the square root of yield shear stress. High shear rate data should not be applied to the Casson equation, because this yields an incorrect result. Moreover, it should be noted that the measurement of yield stress, but also the existence itself, is a somewhat controversial issue [43].

Rheological properties of blood are time-dependent since interaction, deformation and alignment of RBC are not instantaneous; in particular, rouleaux formation depends on the intensity and the duration of the applied stresses. Thus, blood exhibits a thixotropic behavior, i.e. viscosity decreases with time due to shear-induced changes in the fluid microstructure [11]. It is not possible to find an unequivocal definition of thixotropy in the literature but, in general, a material is defined thixotropic when a reversible change in the rheological properties of the system (e.g. the viscosity, elasticity, normal stress) occurs, depending on the application time of a constant shear [43]. After a certain time and for a fixed shear rate, a dynamic balance between growth and destruction of the aggregates is established whereas, the balance evolves in a greater dispersion at the higher shear rate. Gaspar-Rosas and Thurston [52] investigated the aggregation rheology of RBC in a wide range of shear rates (0-500 s^{-1}) reaching the important consideration for which the recovery of the structure requires approximately 50 seconds, while at high shear rate recovery takes place faster.

In order to describe the rheological behavior of blood, many models have been proposed, even though the big majority has been developed for steady state conditions. The most used models are the power-law model, the Quemada model and the Casson equation [53], although no one can fully describe the rheological behavior of blood. Apostolidis and Beris undertook a systematic investigation of blood rheology and demonstrated that the Casson model gives the best approximation of available experimental data [39]. In addition, the same authors proposed a parameterization of the Casson model parameters, the yield stress and the viscosity, in terms of quantities that define the physiological state of blood [39, 44].

1.2.1 Viscoelasticity

Blood viscoelasticity was described for the first time by Thurston [42] and Chien [54]. Due to complexity of blood microstructure, the storage and recovery of the elastic energy and the dissipation of the viscous energy may occur in several ways. Indeed, transient conditions are often encountered *in vivo*, such as in going from larger to smaller

vessels, in vascular bifurcations, and due to the pulsatile nature of cardiovascular circulation. Although the source of blood viscoelasticity is not completely understood, the main role is assumed by morphological and elastic properties of RBC. Drasler and coworkers [55] suggested that the elastic response is associated with the presence of RBC aggregates and with the ability of the erythrocyte membrane to store reversibly energy. On the other hand, the viscous response depends on the hemoglobin solution into the cells, the suspending medium (e.g. plasma) and the viscous contribution of RBC membrane. By applying an oscillatory flow in a tube (i.e. pushing and withdrawing the fluid alternately), Thurston [42] measured blood viscosity and elasticity, and consequently how the cellular arrangements are affected by the flow rate. The viscous component predominates over the elastic one in the entire range of velocity gradient examined; when the amplitude of the shear strain exceeds the unit value, elasticity goes down due to an onset of change in blood microstructure. In order to explain the structural changes, Thurston asserts that increasing shear strain the volume occupied by cells is reduced, leading to the release of trapped plasma and to the formation of viscous fluid layers on which cells can slide [56]. Only more recently, blood viscoelastic behavior has been investigated by using cone-plate and parallel plate geometries at high deformation, where RBC microstructure could be altered [57]. Moreover, passive microrheology [58] and large amplitude oscillatory shear [59] have been used. All data confirm the predominance of the viscous component, albeit an elastic contribution being present as well.

1.3 Haemodynamics

Human body fights disease and maintains a stable internal environment thanks to a vast network of organs and vessels named circulatory system. The study of the relationship among physical properties influencing blood flow through the vessels is defined haemodynamics. Circulatory system includes both the lymphatic system that moves lymph (a clear fluid that resembles plasma), and the cardiovascular system [60] whose main role is the transport of blood throughout the body. The latter consists of the heart, which acts as a pump due to its rhythmic contraction pushing blood in the blood stream, and of a network of branched vessels of decreasing size, that carries blood across the body (Figure 1.10). In particular, arteries transport oxygenated blood and nutrients while veins return carbon dioxide and waste to the heart. The exchange of such substances with body tissues and organs occurs in the capillaries, where oxygen and nutrients move from the blood into the cells, and waste and carbon dioxide from the cells move into the capillaries.

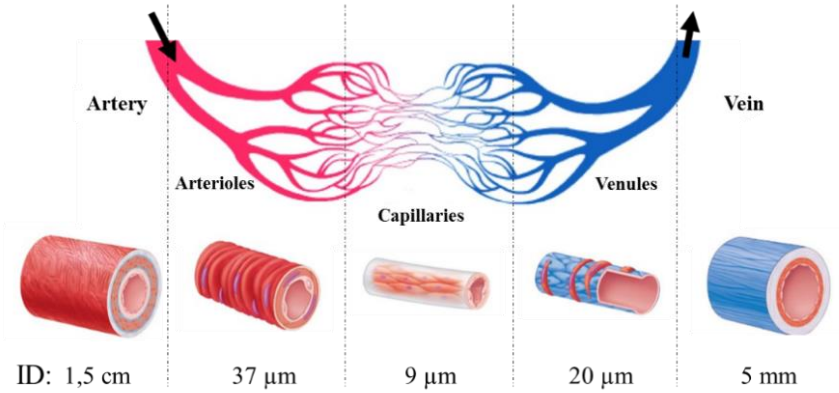

Figure 1.10 - Hierarchy of the circulatory system and average lumen diameter of human blood vessels

As reported in Figure 1.10, the diameter of macrovascular vessels (i.e. the large arteries and veins) ranges from cm to mm while the microcirculation, consisting of arterioles, capillaries and venules, has diameters smaller than 100 µm; in particular, the capillaries present diameters of only a few microns [61].

The system of blood vessels resembles a branching tree leading to large changes in the cross-sectional area. From arteries to capillaries, the total cross-sectional area increases reaching its maximum in the capillary bed; conversely, when venules join to form veins, the total cross-sectional area becomes smaller than capillaries (Figure 1.11A). As consequence, blood flow velocity is inversely proportional to the vascular cross-sectional area: velocity of blood flow decreases as blood flows from the arteries to arterioles and capillaries, and increases as it moves into the venules and returns to the heart (Figure 1.11B). The circulatory system works thanks to the pressure that fluctuates between 120 mmHg (systolic pressure) and 80 mmHg (diastolic pressure). Pressure drop decreases and levels off progressively moving away from the heart; at microcirculation level (arterioles and capillaries) blood pressure is about 35 mmHg and fluctuations vanish due to branching conformation. At the venules inlet, pressure is about 16 mmHg and decreases going towards the veins (Figure 1.11C). In microcirculation, the total cross-sectional area is about 4500-6000 cm^2, and the velocity of blood flow ranges between 0.1 cm/s in capillaries and 20 cm/s in arterioles and venules [61].

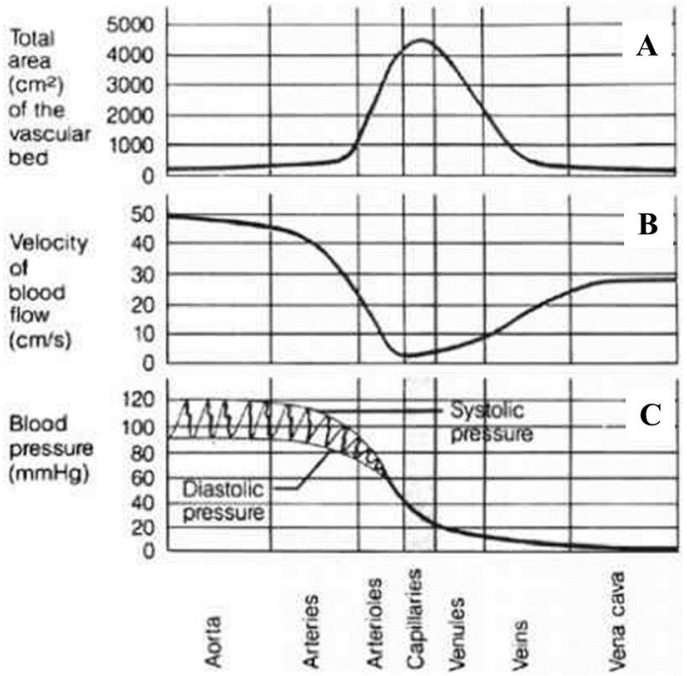

Figure 1.11 - Total cross-sectional area (A), velocity of flow (B), and blood pressure of the systemic human circulation. Re-adapted from [61]

1.3.1 Fluid flow principles in human body

In general, the flow of fluid through rigid tubes is governed by the pressure gradient and resistance to flow which depends on fluid viscosity and channel geometry. Poiseuille's law (sometimes referred to as the Poiseuille-Hagen law) links these properties as follows:

$$Q = \left(\frac{8\eta L}{\pi r^4}\right) \Delta P \qquad \textit{Equation 3}$$

where ΔP is the pressure losses, L and r are respectively the capillary length and radius, η is the suspending fluid viscosity and Q is the flow rate. The term in brackets is the resistance to blood flow which is a function of viscosity, vessel radius, and vessel length. In the human body, small changes in vessel radius cause large changes in the flow to a tissue or organ since flow is related to the fourth power of the radius whereas fluid viscosity and vessel length rarely changes enough to have a significant effect on resistance. In the body, variations in blood flow is usually due to changes in radius.

Poiseuille's law is the basis of much current understanding of blood flow in larger vessels and in microcirculation although the cardiovascular system does not strictly meet the criteria necessary to apply the law. In fact, Poiseuille's law is valid under the following conditions:

- the tube is a uniform, rigid, circular cylinder;
- the flowing fluid is Newtonian;

- the flow is steady, i.e., constant in time, and laminar;
- the flow is not subject to entrance effects, i.e., non-uniformities associated with the entrance of the fluid into the tube.

In many situations of practical interest, including blood flow in human body, such conditions are not always respected. First of all, our circulatory system is composed of branching elastic tubes rather than rigid tubes of constant diameter. However, such properties cause only small discrepancies from Poiseuille's law. Moreover, Poiseuille's law requires steady flow rather than pulsatile and laminar flow conditions characterized by smooth streamlines and highly ordered motion. In addition, as reported in the previous paragraph, human blood presents several non-Newtonian features although it is assumed that viscosity of blood is independent of velocity. Even though the above mentioned restrictions are not satisfied at all, Poiseuille's law succeeds to describe blood flow with a good approximation and it is essential for the understanding of the haemodynamics of the circulation [11].

Laminar flow condition is identified by the Reynolds number, a dimensionless quantity which quantifies the tendency for turbulence (i.e. chaotic changes in pressure and flow velocity). Reynolds number is derived from non-dimensionalization of the Navier-Stokes equations and it is given by the ratio between inertial forces and viscous forces:

$$Re = \frac{Inertial\ forces}{Viscous\ forces} = \frac{vd\rho}{\eta} \qquad \textit{Equation 4}$$

Where v is the mean velocity, d is the tube diameter, ρ is the fluid density, and η is the fluid viscosity. Low Re number ($<10^3$) signifies viscous laminar flow where fluid streamlines are steady and predictable; turbulent flow occurs when Reynolds number exceeds a critical value ($\sim10^4$) which is rarely exceeded in a normal cardiovascular system, but it is altered in several pathological states. Between these two regimes lies a third region ($10^3 < Re < 10^4$) where flow transitions from laminar to turbulent [62].

In the human body, blood flow in large arteries is governed by inertial forces due to very high Reynolds number. However, the total cross-sectional area of the vessel increases going from arteries to capillaries resulting in a decrease of both pressure and velocity. In arterioles and capillaries, Reynolds number is less than 1 indicating the predominance of viscous forces over inertial forces (Figure 1.12).

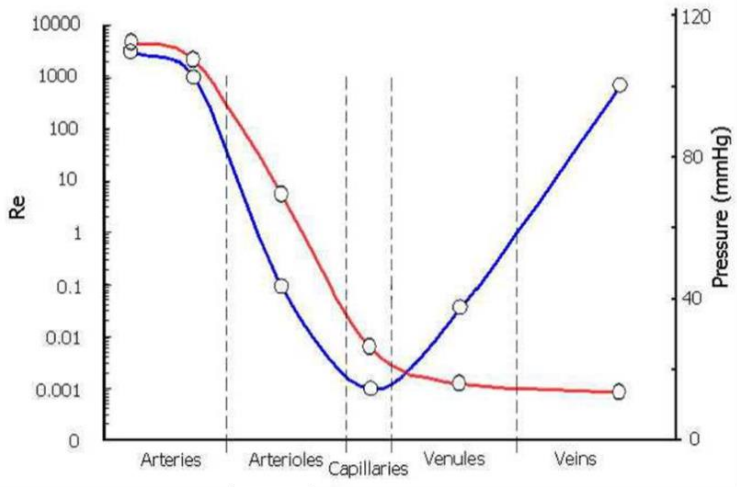

Figure 1.12 - Changes in blood pressure (red line) and Re (blue line) across human body. Re-adapted from [63]

In cross section and under laminar flow, the velocity is zero at the vessel wall due to no-slip condition and increases parabolically with flow, reaching its maximum at the vessel centre (Figure 1.13). The law that governs the rate of a Newtonian fluid at each point in a cylindrical channel is given by the formula:

$$V(r) = \frac{\Delta P}{4L\eta}(a^2 - r^2) \qquad \textit{Equation 5}$$

where a is the channel radius and r is the radial position. In general, this formula can be applied to blood. The peak velocity, which occurs on the centre-line, is given by:

$$V_{max} = \frac{\Delta P a^2}{4L\eta} \qquad \textit{Equation 6}$$

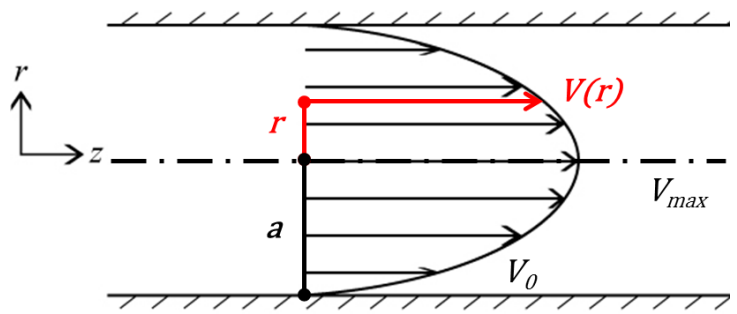

Figure 1.13 - Parabolic velocity profile in Poiseuille flow where a is the tube radius and r is the radial position

The volume flow rate Q in the tube can be calculated by integrating the velocity across the circular cross-section of the tube:

$$Q = \int_0^a V(r) 2\pi r \, dr = \frac{\pi \Delta P a^4}{8 L \eta} \qquad \textit{Equation 7}$$

which is equivalent to Poiseuille's law with r=a.

1.3.1.1 Flow in rectangular channel

Microfluidic channels used in *in vitro* studies can be modelled as orizontal parallel plates, for which there is an analytical solutions for velocity and pressure. In this case, the Navier-Stokes equation can be simplified as:

$$0 = -\nabla p + \mu \nabla^2 \vec{v} \qquad \textit{Equation 8}$$

where p is the pressure and $\vec{v}$ the velocity.
The flow can be treated as a standard pressure-driven flow between two infinite parallel plates (Figure 1.14). The steady velocity profile v(y) is uniform along the length of the plate in the x-direction, and Equation 8 becomes:

$$0 = -\frac{dp}{dx} + \eta \frac{d^2 v}{dy^2} \qquad \textit{Equation 9}$$

integrating Equation 9:

$$v(y) = -\frac{1}{2\eta} \frac{dp}{dx} (hy - y^2) \qquad \textit{Equation 10}$$

which is the parabolic velocity profile of Figure 1.14 for no slip conditions at walls. Since the wall shear stress τ_w is defined as:

$$\tau_w = \eta \frac{dv}{dy} \qquad \textit{Equation 11}$$

the slope of the velocity profile from Equation 10 can be calculated to obtain τ_w at the wall via Equation 11:

$$\tau_w = -\frac{h}{2} \frac{dp}{dx} \qquad \textit{Equation 12}$$

Moreover, the volumetric flow rate can be calculated integrating Equation 10 over the gap between plates:

$$Q = w \cdot \int_0^h v(y) \, dy = -\frac{w h^3}{12\eta} \frac{dp}{dx} \qquad \textit{Equation 13}$$

Combining Equation 12 and Equation 13 it can be possible to obtain a very simple algebraic equation for wall shear stress in terms of volumetric flow rate, fluid viscosity, and flow chamber dimensions:

$$\tau_w = \frac{6\eta Q}{wh^2} \qquad \textit{Equation 14}$$

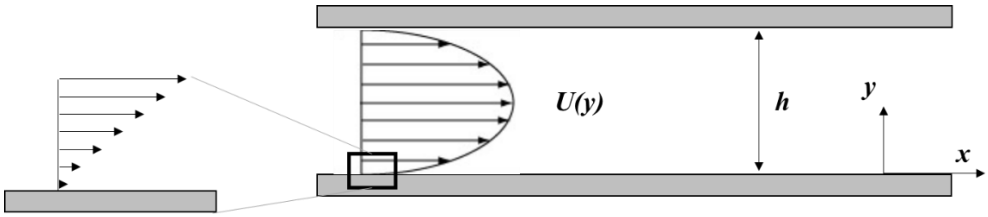

Figure 1.14 - Parabolic velocity profile between the flat parallel plates in the x-z plane

Equation 14 can be applied to a rectangular duct considering the confinement by side walls with some deviations. The extent of the deviations depends on the cross-sectional aspect ratio α = h/w. Low aspect ratio (α→0) implies a slit-like geometry which is close to the ideal bi-dimensional model of Equation 14; on the other hand, geometries with high α (α→1, e.g. square-like geometry) alter flow profile due to wall effects. In this case, Equation 14 can be modified as follows:

$$\tau_w = \frac{2\eta Q}{wh^2}\left(\frac{m+1}{m}\right)(n+1) \qquad \textit{Equation 15}$$

In Equation 15, m and n are empirical constants, with m = 1.7 + 0.5 $\alpha^{-1.4}$ and n = 2 for α < 1/3. It is worth to mention that wall effects will be more pronounced as aspect ratio increases.

The solution for the velocity of Equation 8 can be generalized for rectangular channel having length (L), width (w) and height (h). The velocity along channel width and height is given by a Fourier series expansion:

$$v(y,z) = \frac{4h^2}{\pi^3\eta}\frac{dp}{dx}\sum_{n\ odd}^{\infty}\frac{1}{n^3}\left[1 - \frac{\cosh\left(n\pi\frac{y}{h}\right)}{\cosh\left(n\pi\frac{w}{2h}\right)}\right]\sin\left(n\pi\frac{z}{h}\right) \qquad \textit{Equation 16}$$

where x, y, and z are the coordinate axes along the channel length, width and height respectively. Equation 16 is valid for –w/2<y<w/2 and 0<z<h. The velocity profiles along channel height and channel width are reported respectively in Figure 1.15C and Figure 1.15D. It can be noticed that the profile along h has a parabolic shape whereas it is flattened along w due to the fact that dimension h is smaller than w.

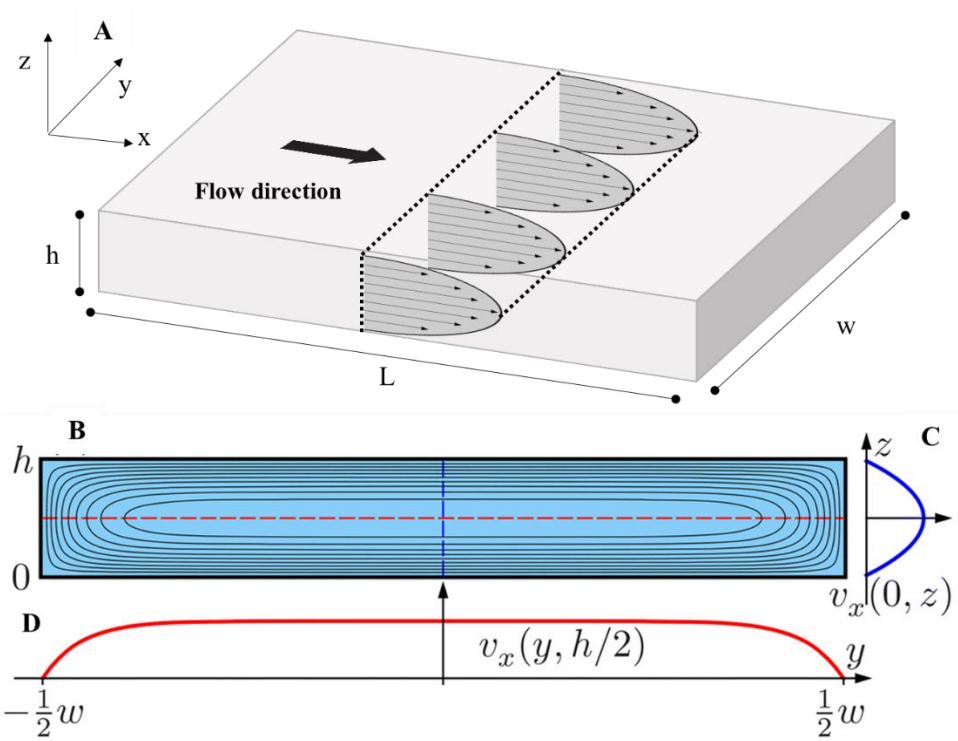

Figure 1.15 - (A) 3D view of the velocity profile for laminar flow in a rectangular microchannel with h<<w. (B) Cross section view of the channel. (C) Plot of the velocity along the height and (D) along the width. B, C, and D re-adapted from [64]

The flow rate can be found by integrating Equation 16 along y and z axes:

$$Q = 2\int_0^{w/2} dy \int_0^h dz\, v(y,z) = \frac{h^4}{12\alpha\eta}\frac{dp}{dx}\left[1 - \sum_{n\ odd}^{\infty} \frac{192\alpha}{(\pi n)^5}\tanh\left(\frac{n\pi}{2\alpha}\right)\right] \qquad \textit{Equation 17}$$

where (α=h/w) is the aspect ratio of the channel. For channels with low aspect ratio (α→0), the flow rate can be approximated by:

$$Q \approx \frac{h^4}{12\alpha\eta}\frac{dp}{dx}(1 - 0.63\alpha) \qquad \textit{Equation 18}$$

Regarding resistance to flow in rectangular geometries, it can be approximated by using Equation 18:

$$R = \frac{12\alpha\eta L}{h^4}\frac{1}{(1 - 0.63\alpha)} \qquad \textit{Equation 19}$$

Wall shear stress can be calculated for channel region where the flow is fully developed. Near the channel inlet, there is a portion of the channel where the flow is characterized by non-parabolic velocity profiles. In fully developed region the pressure gradient and the shear stress in flow are in balance and hence velocity profile does not change. The entrance length depends on Re and channel height h:

$$L_e = ahRe$$ *Equation 20*

1.3.2 Blood flow in microcirculation

From a macroscopic perspective, blood in large arteries can be related as a homogenous fluid, even though it is a suspension of viscoelastic cells in a viscous medium. In microcirculation, the flow behavior of blood at macroscopic level is regulated by individual RBC properties and the interaction among them. For this reason, it is fundamental to approach the study of blood flow in microcirculation at cellular level [63].

The most surprising features of blood flow are the Fåhræus effect and Fåhræus - Lindqvist effect. These two effects are strongly related to the microtube diameter and they were also observed *in vivo* experiments. The flow of a suspension of RBC in channel having dimensions less than 300 μm exhibits a peculiar radial distribution which leads to the migration of RBC toward the center of the channel, and consequently to the formation of a cell-depleted layer near the vessel walls (cell-free layer) [65, 66]. The mechanism of RBC axial migration results from a wall-induced lift enhanced by RBC deformability, which is related to the tank-treading motion of RBC membrane under the velocity gradient by tension and compression forces acting on the cell [67] (Figure 1.16). The wall-induced lift is, in turn, counterbalanced by a shear-induced diffusion that arises due to cell-cell collisions.

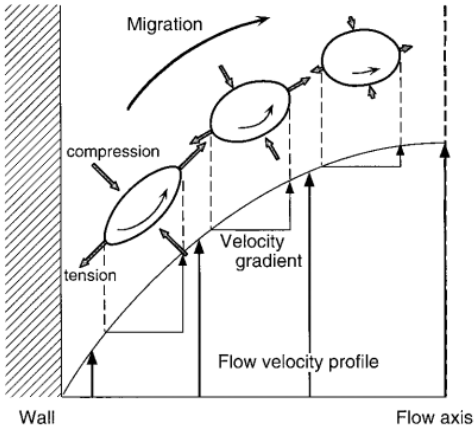

Figure 1.16 - Mechanism of the axial migration of RBC [67]

However, the formation of the cell-free layer has not yet completely demonstrated mainly due to the complex relationship between hemorheological factors [63].

The cell-free layer is thin, but influences the relation between flow rate and pressure drop, acting as a lubricating layer. As a consequence, the concentration of RBC increases in proximity of the center of the channel resulting in a faster motion of the cells when compared with the suspending medium. An increasing average speed of RBC leads to a reduction of the transit time of the RBC through a given tubular segment, and thus to a decreased Htc content in the segment (hematocrit in the tube, H_T) compared to the Htc of the blood entering or leaving it (discharge hematocrit, H_D). This mechanism, known

as the Fahraeus effect [68, 69], suggests that the Htc decreases as the blood proceeds through narrower microvessels (Figure 1.17A).

The Fåhræus-Lindqvist effect is related to the behavior of viscosity as a function of tube diameter, as reported in Figure 1.17B. The apparent viscosity of blood presents a strong decrease with decreasing diameter of the tube until it reaches a minimum of about 7 μm, corresponding to the diameter of the capillary blood vessels. Several experimental works have demonstrated that viscosity continues down to diameters of about 10 μm up to 5 to 7 μm where the effect is reversed. The viscosity increases again in diameters less than 3.5 μm approximately to the levels seen in large vessels [70-72]. This phenomenon endorses that viscosity is affected not the only by Htc, but also by the plasma layer and the microscopic motions of RBC. It should be emphasized that in rotational rheometers these effects have never been observed.

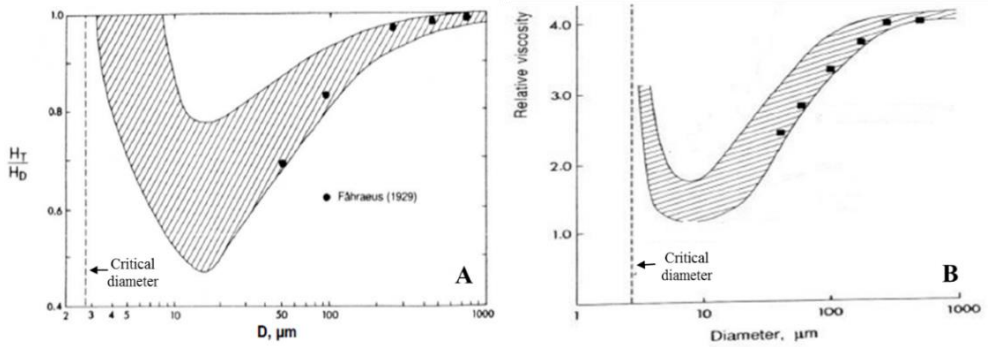

Figure 1.17 - Fåhræus effect (A) and Fåhræus-Lindqvist effect (B) as function of channel diameter [11]. The shaded area contains all published data in the literature until 2006. Data points are the original data

1.3.3 Physiologically relevant *in vitro* models

Over the past decades, the development of microfluidic techniques has contributed to the understanding of the haemodynamics, providing more physiologically relevant models, and creating a novel research field named as *Blood-on-chip* [73]. The main feature of microfluidics is the possibility to manipulate fluids at the microscale level, with high precision and by using small quantities of samples and reagents. Moreover, microfluidic systems show many advantages, such as low fabrication cost, rapid sample processing, and high resolution and sensitivity of the outputs. In microfluidic channels, the flow is finely controlled allowing to predict in a very reliable way the transport of particles (e.g. cells, drug carriers) in the fluid [74].

A lot of papers have focused on the study of blood flow by using *in vitro* models able to reproduce, partially, *in vivo* conditions. These models can be divided in two categories according to their final aim. The first category is made up of models that reproduce complex vessel geometries controlling, in a very accurate way, blood flow conditions and behavior of blood components. Several types of microchannels (i.e. glass, PDMS, plastic) have been used to reproduce microvascular environment allowing a precise control over the experimental variables. Blood flow in microchannels has been widely investigated over years by using several techniques [75-78]. Velocity profiles reported are parabolic in some cases [78, 79] whereas blunt in others [80, 81]. For

example the degree of blunting decreases with the flow rate, likely due to the decreasing of blood viscosity resulting from cell disaggregation and deformation; on the other hand blunting increases with Hct being related to the largest number of interactions of the suspended RBC in shear flow [63]. Although microchannels are fundamental to understand the behavior of RBC under flow, they present significant discrepancies with physiological conditions. For example, in glass capillaries viscosity values are lower [82] and RBC deform less than *in vivo* conditions [83]. These discrepancies have not yet been understood and a variety of explanations have been proposed such as the irregularity of vessel diameters [82], vascular bifurcation [84] and the absence of the endothelial layer lining the lumen surface [85] *in vivo.* On the other hand, models that recreate the inner surface of human vessel by lining microchannels with endothelial cells (EC) belong to the second categories. In this case, the main goal is to replicate human vascular endothelium in order to study cells properties such as morphology, proteins expression or to test drug therapeutic efficacy.

In general, under physiological conditions, blood vessels are exposed to a continuous unidirectional flow that generates a pressure and a shear stress directed respectively normally and parallel to the vessel wall (Figure 1.18A). The pressure results in circumferential stretching of the vessel wall while shear stress exerted longitudinally in the direction of blood flow [86]. In particular, the apical surfaces of the EC layer are subjected to a wall shear stress (Figure 1.18B) which mediates vessel permeability [87], arterial remodeling [88] and pathophysiological processes [89]. Depending on vascular district in human body, EC are subjected to different hemodynamic environments resulting in heterogeneous structures and functions [90].

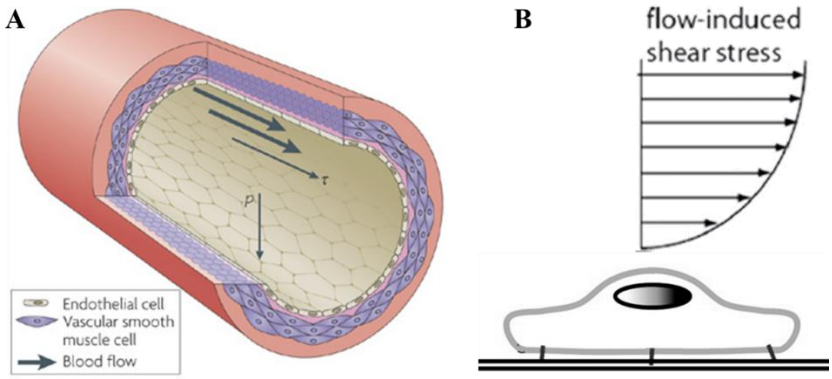

Figure 1.18 - (A) A section of a vessel wall. Re-adapted from [86]. (B) Shear stress acting on the apical surface of an EC

Fiddes et al. [91] suggest an innovative method to fabricate circular microchannel lined with EC to mimic *in vivo* conditions. A cross-section of a 3D circular PDMS microchannel entirely covered with EC is reported in Figure 1.19A-B where cells nuclei and actin filaments are stained respectively in blue and green and visible thanks to confocal imaging. It is interesting to note that cells are able to grow in a uniform manner on the microchannel walls. Unfortunately, flow studies have not been carried out on this model. Similarly, a three-dimensional gelatin chip has been developed for the same purpose but in addition a controlled flow on the EC monolayer has been applied. Authors

suggest their model to mimic *in vitro* physiological environment related to haemodynamics, atherosclerosis, tumor metastasis, and drug screening [92]. By using a similar fabrication process, Wong and Searson [93] have created a perfusable endothelialized microchannel embedded in a extracellular matrix. The authors proposed a new tool for studying the invasion and intravasation of metastatic cancer cell in an artificial microvessels platform (Figure 1.19C). It has to be emphasized that both categories are not complete, i.e. they are lacking in some aspect of physiology and hence of questionable relevance *in vivo*. However, the main drawback is the absence of blood flow [94].

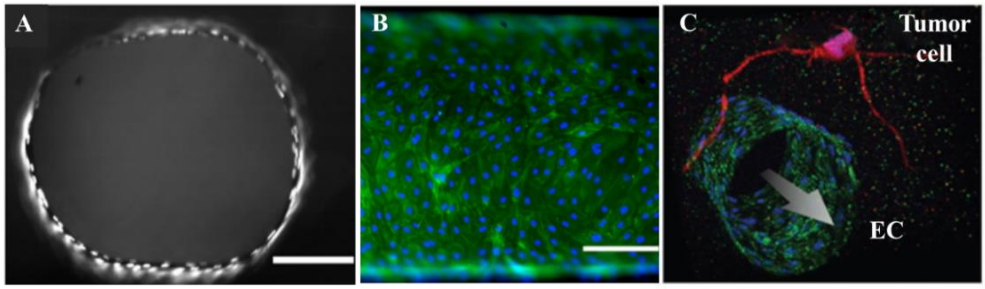

Figure 1.19 - (A) Cross section of a channel lined with EC. (B) Fluorescent image of actin filaments (green) and nuclei (blue) of the same cells. Scale bars 200 µm. Re-adapted from [91]. (C) 3D projection of a confocal z-stack of an endothelialized channel with a cancer cell in the extracellular matrix. Re-adapted from [93]

Moreover, the endothelial GCX is considered to affect blood flow, especially in microcirculation. GCX is a negatively charged brush-like layer of proteoglycans, glycosaminoglycans and glycoproteins located on the inner surface of the vascular endothelium with a thickness ranging from 100 to 1000 nm [95, 96] (Figure 1.20). The negative charge is given by sialic acid (SA) [97] which contributes to the formation of a protective electrostatic shield that ensure antiadhesive forces between circulating cells and vessel walls [98]. In general, GCX components are continuously modified and have a dynamic relation with the blood plasma proteins and molecules that affect the shape and size of the GCX layer [99].

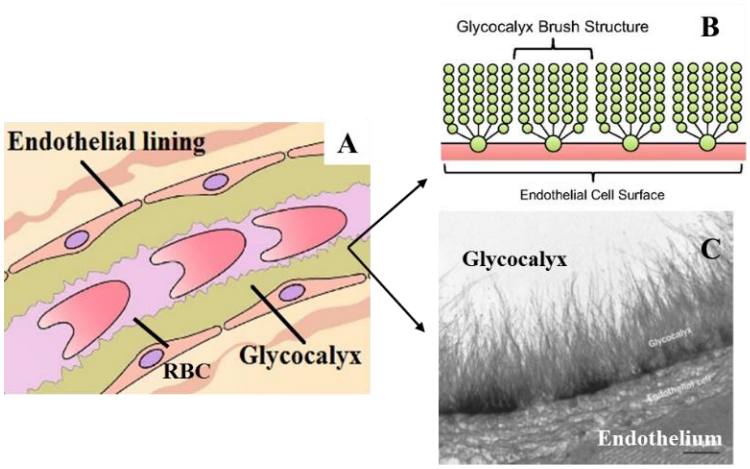

Figure 1.20 - (A) RBC flowing in a capillary covered by GCX; (B) Schematics of the endothelial. Re-adapted from [100]; (C) Electron microscopy image of the endothelial glycocalyx in a coronary capillary. Re-adapted from [101]

In physiological conditions, GCX acts as a protective barrier determining vascular permeability and plays a key role in the vascular mechanotransduction of biomechanical stimuli, such as shear stress, into biochemical signals on the EC [102-104]. Several vascular diseases, such as diabetes, ischemia, and atherosclerosis are associated to GCX alterations [105].

In the case of microcirculation, the GCX layer and its interaction with RBC were modelled by both theoretical and numerical works [106-109]. It was found that flow resistance is lower in glass microcapillaries (i.e. without GCX) compared to microvessels *in vivo* [82]. To overcome this limit, Lanotte et al. [110] proposed an experimental model of the GCX coating glass capillaries with a polymer brush providing support to the hypothesis that GCX influences blood flow in microvasculature. However, there it is still not clear what role GCX plays in mediating blood flow.

1.3.4 Case study: *Plasmodium falciparum* malaria

Malaria is responsible for hundreds of thousands deaths every year in many countries where it is endemic. *Plasmodium falciparum* induced malaria is the most widespread parasitic disease in humans, with a mortality of 15–20%, mostly children in sub-Saharan Africa [111-114]. Over the years, effective treatments have been used against malaria but every time the parasite has been able to develop resistance [115]. A better understanding of the molecular and physiological processes through which the parasite is able to proliferate inside the blood stream and evade the immune system is an open issue related to the development of a viable and efficient vaccine [116].

The complex life cycle of malaria parasites is reported schematically in Figure 1.21. The parasites enter into human body in the form of sporozoites through the bite of a female *Anopheles* mosquito arriving to the liver. The asexual reproduction of the sporozoites produces free forms of parasite called merozoites which are released in the blood stream. Then, parasites start repeated rounds of multiplication progressing in ring, trophozoite and schizont stages [115]. For its development, parasite digests hemoglobin

inside the host cell and after 48 hours the rupture of RBC occurs, releasing 15-30 daughter merozoites ready to infect new nearby RBC. Generally, the invasion is consummated within few minutes after the parasite releasing due to the limited capacity of the falciparum merozoites to live outside the host cell [117]. A small part of parasites (less than 10%) differentiate into gametocytes which are the sexual form of the parasite [118]. They are responsible of the transmission to the mosquito where undergo a sexual cycle in the gut, before entering the salivary gland as sporozoites to complete the cycle [119].

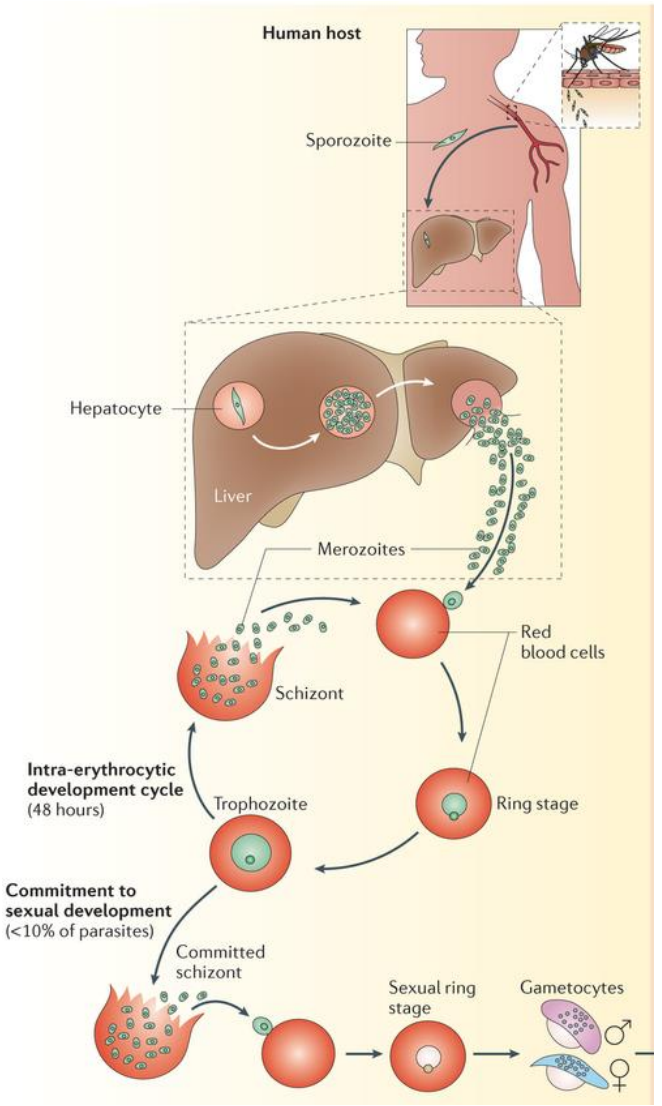

Figure 1.21 - Life cycle and pathogenesis of malaria in human body. Re-adapted from [118]

The pathogenicity of *Plasmodium* parasite involves the ability of mature infected RBC (iRBC) to undergo several adhesive interactions, defined cytoadhesion. In

particular, iRBC can bind endothelial cells (sequestration), and adhere to healthy RBC (hRBC) (rosetting) and with other iRBC (auto-agglutination) [120]. It is well known that such phenomena lead to the development of severe malaria, i.e. potentially fatal manifestation or complication, due to clogging of the vessels [120] and the lack of identification of iRBC by the spleen [121]. Furthermore, *Plasmodium falciparum* expresses proteins that are transported to the RBC membrane causing changes in rigidity and shape of the iRBC [122].

Among them, the sequestration phenomenon is the most investigated in literature although the question of how it develops is still unclear. Several hypotheses have been proposed such as changes of RBC rigidity [112, 123], induction to release pro-inflammatory receptors [124], binding of iRBC to specific adhesion receptors on endothelial cells [125], and activation of endothelial receptors [126, 127]. Recent finding reports the possible role of platelets and coagulation cascade [128, 129].

The work of MacPherson et al. [130] has provided further clarification on the mechanism identifying the contact point for iRBC *in vivo* as knob-like structure, which had previously been demonstrated in *in vitro* studies. Knobs are adhesive protrusions that the parasite induces on the surface of the host cell around 16 hours after injection. Such structures contain several proteins including PfEMP-1 (*Plasmodium falciparum* Erythrocyte Membrane Protein-1) which is largely considered responsible for iRBC adhesion [131].

Under physiological flow conditions, the cytoadhesion of iRBC may be mediated sequentially by a number of endothelial adhesion molecules which lead iRBC undergoing typical dynamic behavior, e.g. rolling; this behavior is similar to leukocytes in the first step towards extravasation during an acute inflammation [132, 133]. In fact, leukocytes use selectin receptors for rolling, localized on many microvilli rather than knobs. The majority of the studies about the behavior of iRBC cytoadhesion under flow have been carried out by numerical simulations. Fedosov et al. [134] investigated the dynamic of iRBC in cylindrical capillaries varying some parameters as cell stiffness, flow conditions, tube dimensions and Htc. The results has releveled several types of cell dynamics such as solid adhesion, slow slipping along the wall, and intermittent flipping. Moreover, by using the same multiscale model, blood flow resistance and adhesive dynamics of individual iRBC has been evaluated [135, 136]. Experimental data available in literature are fewer than simulation results. The reason is the difficulty to recreate an *in vitro* model that allows both a high level of similarity to the real case and that it is not extremely complicated. Indeed, several authors have preferred to create coated microchannel with some of the adhesion molecules which is believed to be involved in the pathway (e.g CD36, V-CAM1, I-CAM1) [137, 138] rather than cultivate endothelial cells.

Recently, Hempel et al. [139] focused attention on the role of endothelial GCX in malaria pathogenesis. It has been suggested that the initial contact between iRBC and the vascular endothelium occurs via GCX due to the ability of infected erythrocytes to bind GCX components such as heparin sulfate and chondroitin sulfate [131, 140]. Studies on the loss of endothelial GCX as a consequence of malaria has so far not been investigated in humans. Therefore, only hypothesis on the mechanisms through GCX influences the binding of iRBC to endothelial cells have been proposed, based on the

ability of parasite itself to produce substances with sheddase-like activities, such as enzymes [141]. However, there it is still not clear what role GCX plays in mediating adhesion of iRBC.

1.4 Aim of this work

Rheological properties of blood are extremely important in the regulation of *in vivo* blood flow. The main goal of this work is to provide elucidations on some of the not well understood issues related to blood flow.

To date, the majority of both research and clinical investigations in the field of hemorheology are based on steady shear measurements in particular in physiological conditions. However, they can elucidate only a part of the non-Newtonian characteristic of human blood. To overcome this limit, the first aim of this thesis is a deep investigation of blood rheology under both steady and oscillatory shear conditions by using bulk rheology. The steady conditions give information about viscosity while the oscillatory experiments provide information on the blood viscoelasticity behavior in the linear viscoelastic regime. Such investigation could help in elucidating the significance of hemorheological alterations in pathological situations, where increased hematocrit levels and aggregability are found. In addition to rheological studies, current haemodynamics investigations still present discrepancies between *in vitro* studies and physiological conditions. The second aim of this work is the study of the interaction between RBC and endothelial cells under flow. To achieve this purpose, a simple *in vitro* model which is closer to physiological conditions, is developed. Endothelial cells are subjected to a continuous flow for several days in order to induce alignment as well as occurs in human vessels.

In conclusion, all the proposed approach aspires to supply novel information that could be helpful for a complete comprehension of blood flow in human body and for the development of microfluidic platform to study drug delivery of carriers in blood circulation.

1.4.1 Overview

More in detail, in chapter 1 a general background of blood rheology and haemodynamics is presented. Chapter 2 shows a systematic characterization of human blood by using conventional bulk rheology under both steady and oscillatory shear conditions. The former gives information about viscosity while the latter provides information on the blood viscoelasticity behavior in the linear viscoelastic regime. Effect of increased RBC volume fraction and effect of adding aggregating media are shown. In chapter 3 methods developed to create a simple *in vitro* model that mimics medium size human vessels are reported. In particular, human endothelial cells, cultured in a microchannel and subjected to a continuous medium flow are used to recreate physiological flow conditions. Once the basic concepts for the *in vitro* culture of endothelial cells are implemented, in chapter 4 RBC-endothelial cell interaction are studied. Velocity profile of RBC suspensions is the main parameter monitored during experiments varying flow conditions and positions along the width and the height of the microchannel. The effect of the endothelial GCX on RBC velocity is also considered. Finally, an interesting case study about adhesion of RBC infected by malaria parasite

Plasmodium falciparum to endothelial cells is presented. Finally, in the appendix A, a preliminary study on the development of oligonucleotides-functionalized surfaces for fluorescence-based biosensing applications is reported.

2. Rheology of blood

Main results reported in this chapter are the topic of a peer-review article in Rheologica Acta [9]. Rheological characterization of human blood both under steady and oscillatory state is reported. Blood is characterized both in physiological conditions and in RBC aggregating media. The latter ones is obtained by the addition of a polymer and by increasing the Htc above the normal physiological levels.

Blood samples with Htc values ranging from 8% to 99% are investigated under steady state deformation.

Moreover, a systematic set of oscillatory shear measurements by conventional bulk rheology is carried out in order to evaluate storage and loss moduli of whole human blood. The viscoelastic behavior is evaluated in the linear regime imposing small deformation in order to keep the sample microstructure unaffected.

2.1 Materials and methods

2.1.1 Blood samples

Blood samples were processed according to the standard protocol for hemorheological tests [142]. Human blood was obtained from healthy volunteers (male and female, age ranging between 26 and 52 years, Hct ranging from 40 and 50%). Venous blood was drawn from the antecubital vein and collected into Vacutainers (BD) containing ethylenediaminetetraacetic acid (EDTA) and stored at room temperature.

Regarding RBC aggregation studies, blood samples have been centrifuged for 15 minutes at 1600 RPM and plasma and buffy coat discarded. The RBC were then washed twice with isotonic phosphate-buffered saline (PBS, pH 7.4). Dextran (MW 500 kDa from *leuconostoc mesenteroides*, Sigma-Aldrich) solutions have been prepared dissolving dextran powder in PBS. Then, washed RBC were added to dextran solution at the Htc value desired.

On the other hand, in order to obtain rheological reference curves of human blood, the samples were used as such (i.e., at the Htc at the moment of collection). The effect of the RBC volume fraction on blood rheological properties has been investigated centrifuging blood samples for 15 minutes at 1600 RPM. The suspended plasma was aspirated through a large-bore needle and saved. Subsequently, RBC were re-suspended in autologous plasma at the desired Htc values. RBC aggregation properties have been studied by adding dextran to whole blood at two concentrations: 1.5 and 3 $mg_{Dextran}/ml_{blood}$. Each step of the experimental protocol was performed at room temperature.

Before and after experiments, RBC viability was checked by monitoring cell morphology by using a microscope with a high magnification objective.

2.1.2 Rheological measurements

Rheological tests were performed within 6 hours from blood collection by using a stress-controlled Physica rheometer MCR 301 (Anton-Paar) equipped with a titanium double-gap measuring system (DG 26.7, inner cup diameter: 24.267 mm, inner bob diameter: 24.666 mm, outer bob diameter: 26.663 mm, outer cup diameter: 27.053 mm and bob height: 40.000 mm). The bob rotates inside the cup, which is still and maintained at a constant physiological temperature of 37°C by a Peltier system. This assembly, presenting a high surface area and requiring small amount of sample (i.e. 1.8 ml), is ideal for low viscous biological materials, such as blood.

In each test, blood samples have been gently agitated before loading, in order to homogenize the sample. After loading, the blood surface exposed to air (i.e. in the upper part of the assembly) was covered by an oil film to avoid the formation of a protein layer at fluid–air interfaces that generates mechanical strength.

In order to prevent RBC sedimentation and to disrupt any aggregates, possibly formed during the loading step, each test was preceded by a pre-conditioning phase, at a constant shear rate of 200 s^{-1} for 20 s, followed by a rest phase of 5 s, needed to allow sample relaxation.

Steady shear experiments were performed from low to high shear rates (and back in some cases, up-down curves) and viscosity curves were recorded by using at least 30 measuring data points with sampling time of 10 s.

Oscillatory shear tests have been performed in order to evaluate blood storage modulus G' and loss modulus G''. Each oscillatory measurement has been preceded by strain amplitude sweep test at 1 rad/s and 10 rad/s for strain amplitudes from 0.1 to 100%, in order to determine the linear viscoelastic regime. The frequency sweep tests were performed from 30 to 0.1 rad/s and strain amplitude from 7% to 10%, depending on the data provided by amplitude test. The number of data points per interval ranged from 8 - 16, depending on the type of sample examined.

2.2 Results

2.2.1 Whole blood steady-state behavior

In Figure 2.1A is reported the master curve of blood viscosity of 5 healthy donors performed in physiological conditions (T=37°C and Hct about 45%). The average viscosity of 20 tests is plotted as a function of shear rate and the error bars represent the standard deviation. It is possible to observe the well-known shear thinning behavior of whole blood (black circles) which is typical of aggregating suspensions, such as whole blood. At very low shear rate RBC tend to aggregate but increasing shear rate induces first disaggregation of RBC structures, and then a subsequent cell deformation.

Blood presents time dependent effects due to disruption and formation of RBC aggregates under flow and for this reason, in the development of the experimental protocol, blood samples have been subjected to a pre-shear step (200 s^{-1} for 20 s) in order to promote the homogeneity of the sample and to reduce any memory effects [143]. At low shear rates, with the pre-shear step, viscosity values are higher than the ones in the sample without pre-shear, indicating the presence of memory effects and the (partial) breakage of the static microstructure made by RBC aggregates (Figure 1.16A, open

circles). At shear rates higher than about 5 s^{-1} the pre-shear effect disappears, likely due to flow-induced disruption of RBC aggregates. Moreover, sedimentation and possible syneresis (phenomenon leading to the formation of a plasma layer near the surface) have been investigated by increasing and subsequently decreasing the imposed shear rate (black and grey triangles, respectively in the inset of Figure 2.1A) without reloading the sample and without pre-shear. When the flow rate decreases from high to low values, the onset of sedimentation can be noticed. It is due to RBC aggregation promoted by flow conditions, which in turn leads to a slight discrepancy between the down-up and up-down curves, often referred to as the thixotropic behavior of blood. In order to avoid this effect, only the increasing shear rate flow behavior (down-up curve), without the pre-shearing step, will be considered.

Another peculiar signature of non-Newtonian behavior of blood is the presence of a yield stress. Whole blood yield stress has been confirmed experimentally by direct measurements [40] and by using the Casson model [144]; the latter can be applied to experimental data recorded at low shear rates. For this purpose, data reported in Figure 2.1A have been rearranged in the so-called Casson plot (i.e. square root of shear stress *vs* square root of shear rate), as shown in Figure 2.1B. Data points have been fitted by linear regression (r^2>0.99), and extrapolation to zero shear rate returned the square root of the yield stress. The yield stress values for samples with and without pre-shear have been estimated equal to 5.2 mPa and 3.8 mPa respectively. These values are in good agreement with previous works (ranging from 1.5 mPa to 5 mPa), both experimental [145] and theoretical [146]. The variation of yield stress values has been attributed to artifacts arising from experimental procedures followed by each investigator as well as the interactions between RBC and surfaces of the rheometer [44].

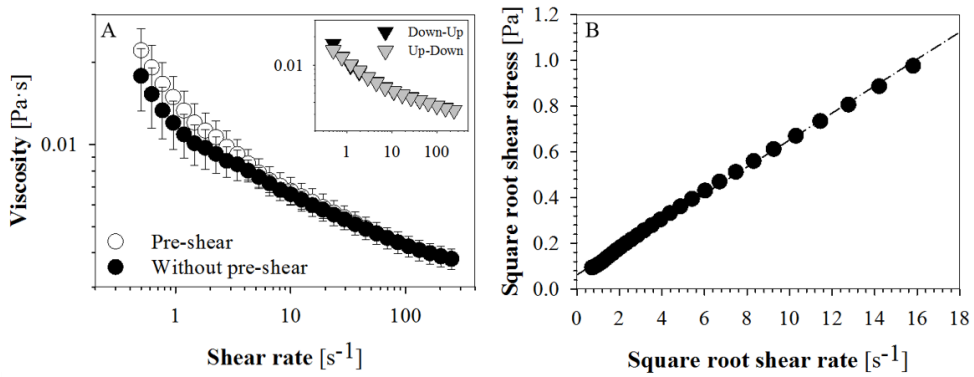

Figure 2.1 - (A) Master curve of whole blood viscosity as a function of shear rate: by applying a pre-shear (open circle) and in absence of pre-shear (dark circle). In the inset, black triangle represents the down-up curve, grey triangle represents up-down curve. (B) Casson plot of the data presented in Figure 2.1A, without pre-shear. The continuous line is a linear fit of the experimental data [9]. The error bars represent the standard deviation

2.2.2 Whole blood linear viscoelasticity

The viscoelasticity of blood has been characterized via frequency sweep test in which the frequency is varied while the amplitude of the deformation is kept constant.

Amplitude sweep tests have been carried out before each oscillatory measurement (Figure 2.2B) in order to evaluate the linear viscoelastic region, and consequently which value of deformation to be used in the experiments. It is possible to note that the onset of the nonlinear regime is around 5 mPa for the elastic modulus, a value very close to the yield stress. Such measurement confirms that blood microstructure is "at rest" in the linear viscoelastic region. In Figure 2.2A, G' and the G'' as a function of angular frequency, are reported. The loss modulus predominates over the storage one across the entire tested range of frequency and both moduli increase with frequency in a parallel manner. A similar trend can found in other complex fluids such as weak gels and weak attractive suspensions/emulsions [147-149]. The predominance of G'' over G' indicates the main role played by viscous dissipation in blood viscoelasticity whereas the absence of a crossover probably indicates that no major change in the structure of the RBC network occurs in the frequency and deformation range investigated.

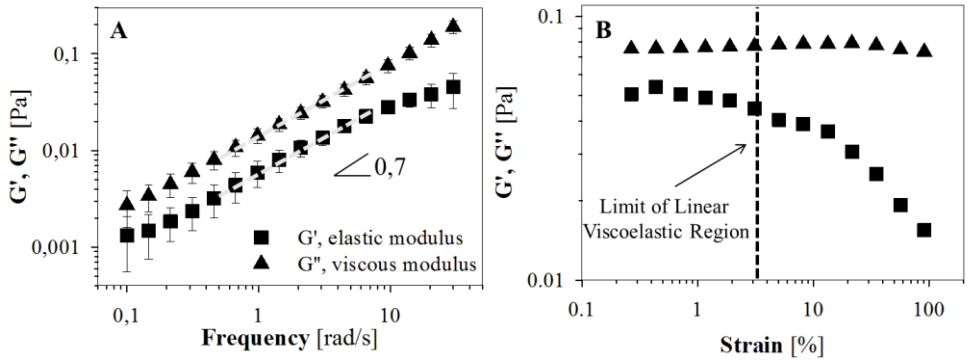

Figure 2.2 - (A) G' (squares) and G'' (triangle) as a function of angular frequency. The grey dashed lines represent a power law fitting of the experimental data (R^2=0.99), the exponent for both G' and G'' being 0.7. (B) Strain amplitude sweep test (G' and G'' as a function of strain) at 10 rad/s for strain amplitudes from 0.1 to 100%. Re-adapted from [9]. The error bars represent the standard deviation

Thurston [42, 107, 150] demonstrated that blood viscoelasticity in tube flow is characterized by the presence of 3D networks of RBC only at very small deformations (about 1%). These deformation values are beyond instrumental sensitivity due to the low viscosity of blood, and the higher deformations in our experimental conditions could lead to (partial or full) breakage of 3D structures. In particular, RBC become arranged in 2D structures flowing in layers separated by the suspending medium, which acts as a lubricant in between (Figure 2.3) [56]. So, the elastic contribution might be due to the tendency of two adjacent RBC layers to interact because they are close enough to be affected by each other, also thanks to the presence of plasma proteins, which can enhance RBC interactions. Thus, RBC aggregation tendency is related to two opposing forces: the adhesion forces between adjacent RBC layers promoted by plasma proteins, and shear flow which tends to disaggregate RBC aggregates. It is important to note that under physiological conditions, blood flow is strong enough to break RBC aggregates, allowing optimal microcirculation and tissue perfusion.

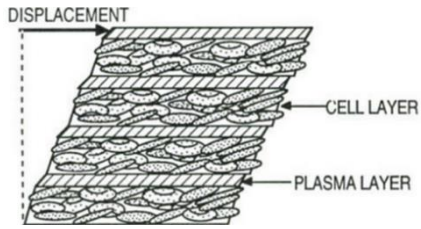

Figure 2.3 - Plasma release cell-layering theory [56]

Figure 2.2A shows the high reproducibility of the measurements, despite the difficulty in handling a complex biological fluid such as blood. In fact, one of the main issues to take into account is the role of RBC sedimentation. The impact of RBC sedimentation has been investigated measuring G' and G'' as a function of time, as reported in Figure 2.4A. It can be noticed that G' and G'' variations with time are rather limited (12.5% for G', 6.7% for G''), indicating that kinetic of RBC sedimentation is negligible during rheological test (about 13 min). In addition, the average of data points of each frequency has been plotted on the moduli master curve of Figure 2.2A; in Figure 2.4B one can observe that there is a good agreement between data. This result is supported by Fabry [151], who reports that sedimentation becomes significant only after 20 minutes in static conditions. Thus, the higher magnitude of error bars at the lower frequencies in Figure 2.2A could be related to the instrument detection limit due to the low viscosity of blood.

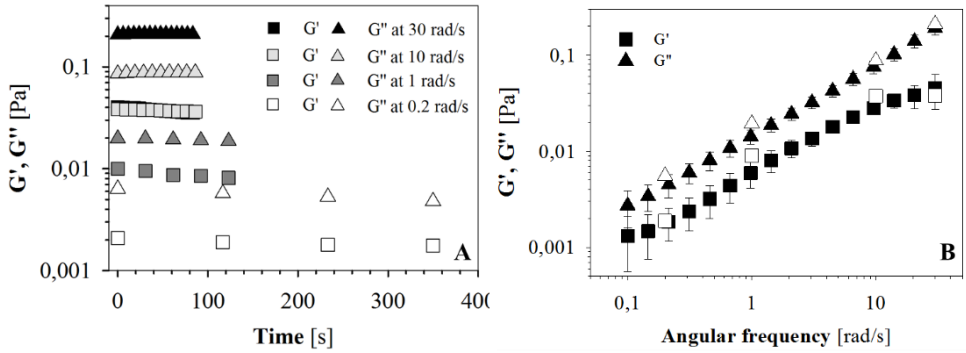

Figure 2.4 - (A) G' and G'' as a function of time for four different angular frequencies. (B) Data average of Figure 2.4A (white symbols) plotted on Figure 2.2A. Re-adapted from [9]

The viscoelastic characterization of human blood under oscillatory shear flow is a novelty of this work and only few authors reported similar results. For this reason, the mechanical spectra obtained in this work is compared with some literature data [57, 58] in Figure 2.5 where black symbols refer to this work, grey symbols to Alves et al. [57] and open symbols to Campo-Deano et al. [58]. Alves et al. performed experiments by using rotational rheometer equipped with cone-plate geometries under oscillatory flow. Data were obtained with an amplitude of 20% which is beyond the linear viscoelastic regime according to Figure 2.2B Although Campo-Deano et al. used passive microrheology techniques, a reasonable agreement can be found, at least in the range 1-10 rad/s. The comparison confirms that blood microstructure is essentially the same both in the static conditions encountered in microrheology and at low frequencies in bulk

rheology, in other words it consists of more or less aggregated RBC. It is worthwhile to mention that passive microrheology is based on the motion of a bead; so one could speculate that the source of viscoelasticity found by Campo-Deano et al. is due to confining effect resulting from RBC aggregates in the sample. Furthermore, RBC aggregates in bulk rheology are probably disrupted at high frequency; for this reason after about 10 rad/s, the data deviate between them. Campo-Deano et al. found a crossover of the moduli while in the bulk rheology G' and G'' tend to separate. In general, there is a significant agreement between the three data sets especially considering that the results refer to different experimental techniques and on blood samples treated in different ways [9].

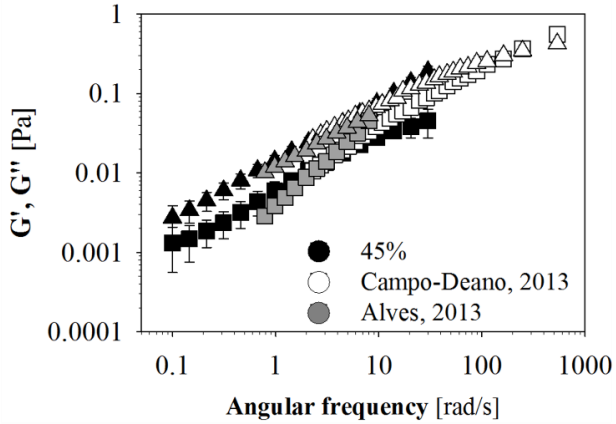

Figure 2.5 - Comparison between whole blood mechanical spectra and results from the literature [9]. The error bars represent the standard deviation

2.2.3 Effect of RBC volume fraction

The contribution of Htc values on blood rheology has been investigated varying RBC volume fraction from 8% to 99%. This range allows to understand the rheological behavior of human blood from the semi-diluted up to the highly concentrated regime.

In particular, rheology of semi-diluted RBC suspensions is interesting because Htc in microcirculation is less than the physiological value of 45% [152]. On the other hand, the rheological behavior of concentrated RBC suspensions (i.e. Hct higher than 45%) is important in order to elucidate some aspect of blood disorders such as polycythemia and myeloproliferative neoplasm in which Hct values are about 60%, causing impaired blood flow at the microcirculation level and thrombotic events [153-155]. Moreover, RBC stored in blood bags used for RBC transfusion can undergo rheological alterations. In such bag, Htc is higher than 90% [156, 157].

The increase of RBC volume fraction with respect to the physiological value of 45% (black circles in Figure 2.6) induces an upward shift of the viscosity curves and the typical shear thinning behavior of blood is preserved. It should be emphasized that Htc of 99% means that the suspending medium (i.e. plasma) is only 1%; despite there is almost fluid suspending, blood viscosity decreases maybe due to dynamic change of RBC morphologies [48]. For Htc lower than 45%, it should be noted that viscosity curves

reach a Newtonian plateau around 10 s^{-1}, especially 8% and 16%. Therefore, RBC volume fraction affects both viscosity and the degree of non-Newtonian behavior.

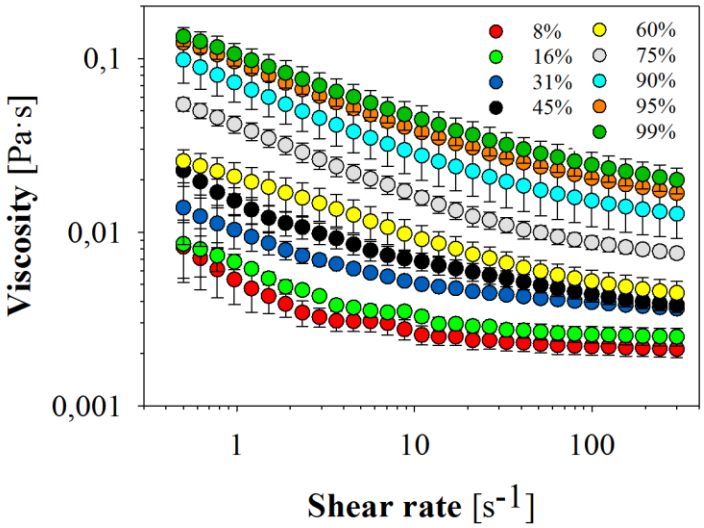

Figure 2.6 - Viscosity as a function of shear rate of RBC suspensions at 9 different Htc. The error bars represent the standard deviation

Moreover, Figure 2.7 presents viscosity at four selected shear rates (i.e. 0.5, 1.5, 11 and 193 s^{-1}) for the Htc values of Figure 2.6. The dependence of viscosity on RBC volume fraction can be fitted with an exponential law with exponent ranging from 0.034 (shear rate 0.5 s^{-1}) to 0.024 (shear rate 193 s^{-1}).

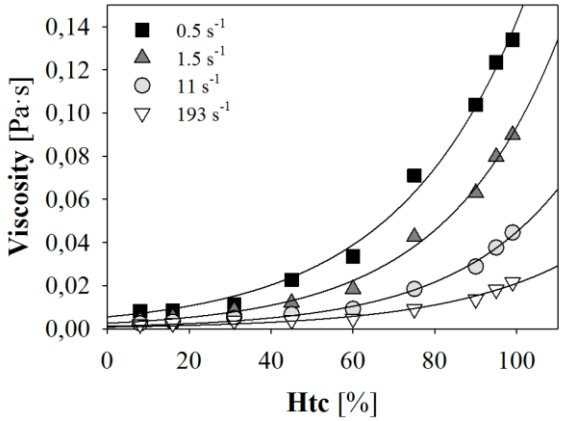

Figure 2.7 - Viscosity as a function of Hct at four different shear rates

For data reported in Figure 2.6, it has been extrapolated the yield stress values according to Casson's law (black circles in Figure 2.8). The value at Htc 8% was not reliable due to the very low viscosity of the sample and hence it has not been reported here. Experimental data of this work have been compared with previous papers with which we are in good agreement. Our data have been fitted with a power law having an exponent of 3.6 (r^2=0.996); this value is very close to the ones of other works (ranging

from 2.9 to 3.3). The little overestimation could be related to the wide range of Htc used that nobody has ever investigated.

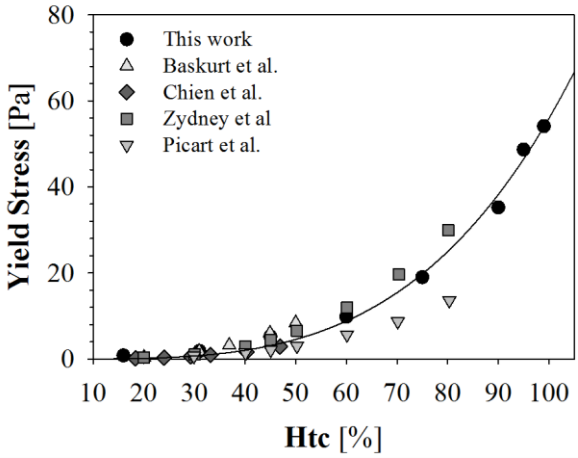

Figure 2.8 - Yield shear stresses obtained from Figure 2.6 plotted versus Htc (black circle). Curved line through points is a power law regression (exponent = 3.6, r^2 = 0.996). Triangle up [11], diamond [145], square [158], and triangle down [40] are data from previous works

Regarding viscoelasticity, the effect of Htc (60% and 90%) on RBC suspension moduli is shown Figure 2.9. Preliminary amplitude sweep tests have been performed for each Htc values (Figure 2.9B). The linear viscoelastic region has never exceeded 10% of strain. Appling oscillatory deformations it can be noticed that increasing Hct induces G' and G'' to approach one to each other and to be less dependent on frequency. Furthermore, they are shifted up suggesting a trend towards an elastic-solid like behavior (Figure 2.9A).

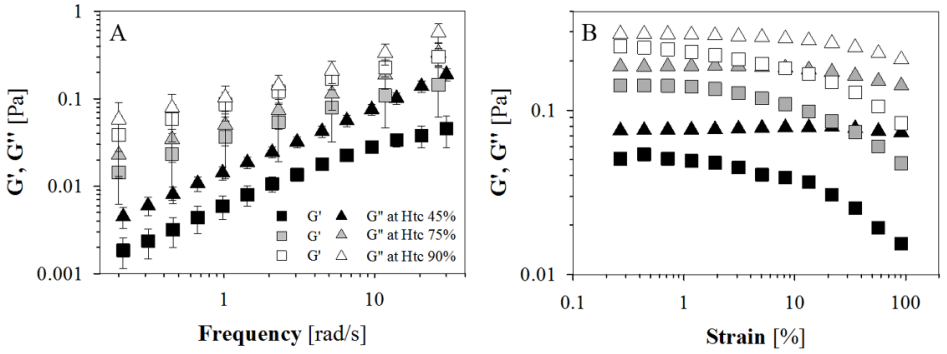

Figure 2.9 - (A) G' and G'' as a function of angular frequencies for RBC suspensions at 60% and 90%; (B) Strain amplitude sweep test at 10 rad/s for RBC suspensions of different volume fraction [9]. The error bars represent the standard deviation

Mechanical spectra of 60%, 95%, and 99% were also carried out. In Figure 2.10 it is reported the dependence of G' and G'' from Htc at 1 rad/s and 11.7 rad/s. Viscous component is always higher than the elastic one except for Htc 99% at 1 rad/s.

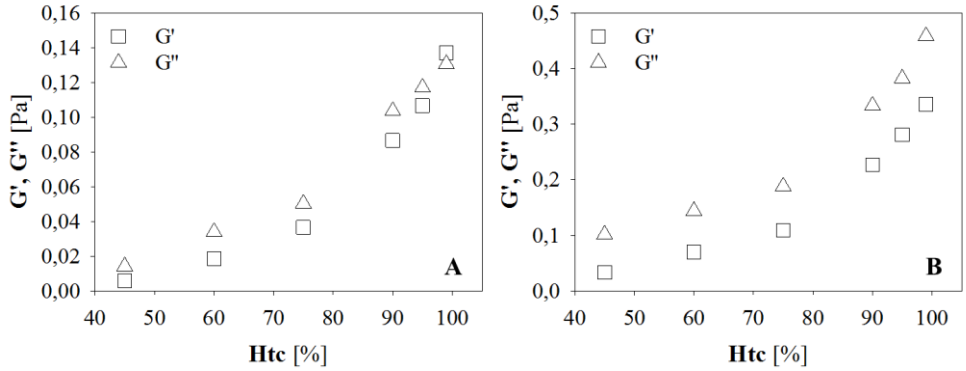

Figure 2.10 - G' and G'' as function of Htc at 1 rad/s (A) and 11.7 rad/s (B)

This inversion is more evident looking at the plots of Figure 2.11. Loss modulus G'' against storage modulus G' as function of angular frequency is reported for six Htc values (Figure 2.11A). G'' values are higher than the ones of G' indicating that the viscous response of the material prevails on the elastic one, this trend decreasing at increasing Hct. Only in the case of Htc 99%, G' results higher than G''. Moreover, the higher is Hct, the more the curves are shifted rightward, making the response of the material closer to the one of an elastic solid. In addition, tan δ that represents the ratio of the viscous to the elastic response (energy loss/energy stored) of the materials is reported in Figure 2.11B. It decreases with RBC volume fraction and at the highest Htc (i.e. 99%), the loss tangent is smaller than 1 indicating that G' is bigger than G''. As in the case of G' vs G'' plot, the trend of tan δ clearly indicates that very high concentrated suspension of RBC approaches to an elastic solid behavior.

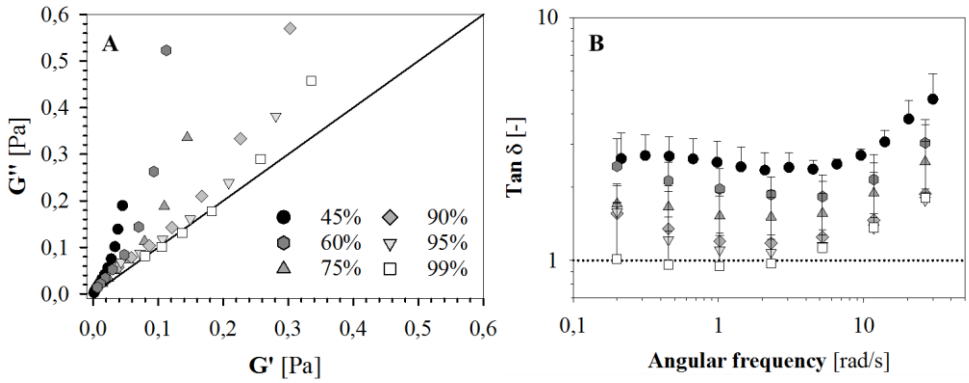

Figure 2.11 - (A) G'' vs G' and (B) loss tangent as a function of angular frequency for six RBC suspension of different volume fractions. Re-adapted from [9]. The error bars represent the standard deviation

Cox-Merz rules has been applied to compare oscillatory and steady shear conditions for four Htc values. Figure 2.12 shows viscosity and the magnitude of complex viscosity as function of shear rate and angular frequency, respectively. For all Htc values, viscosities show a good agreement leading to further support to the hypothesis that in both continuous and oscillatory flow, the disruption of the 3D RBC network occurs.

Complex viscosity values are slightly higher than viscosity ones at low shear rates/frequencies; such discrepancies could indicate the presence of some 3D structures in the low frequency range.

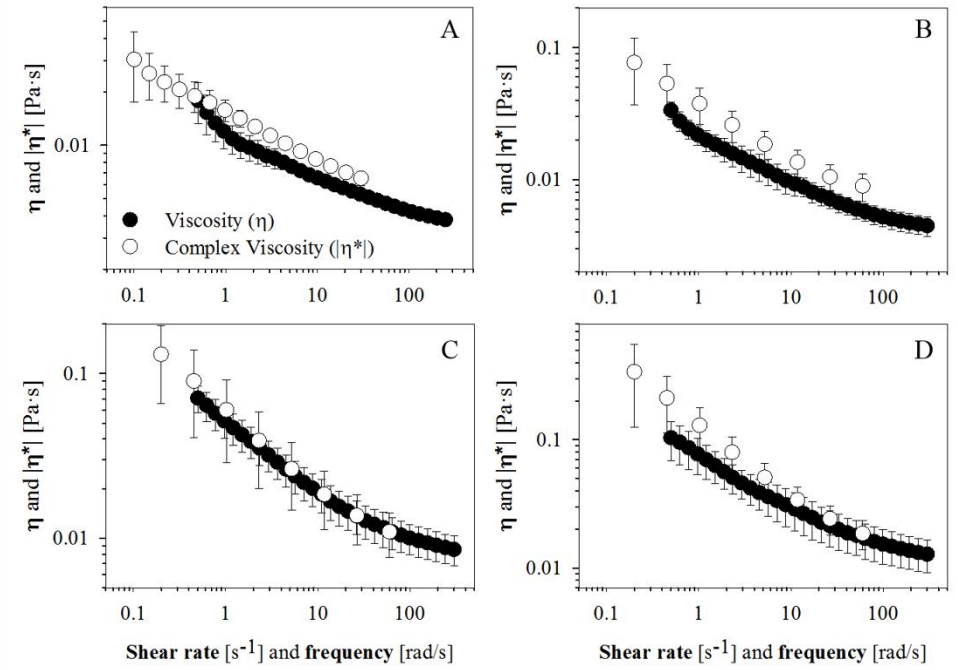

Figure 2.12 - Comparison of viscosity and magnitude of complex viscosity by applying the Cox-Merz rule for A. Hct=45%; B. Hct=60%; C. Hct=75% and D. Hct=90% [9]. The error bars represent the standard deviation

2.2.4 Effect of RBC aggregation

The tendency of RBC to aggregate in packed structures in important issue in the regulation in blood flow, mainly because it causes an increase of blood viscosity, especially at low shear rates. The formation of complex 3D structures of RBC is dependent on both the number of RBC involved in the process and the cohesive forces within aggregates; the latter is usually expressed in terms of the shear stress/shear rate required to disperse the aggregate. In physiological conditions, RBC aggregation is promoted by several plasma proteins, primarily fibrinogen, whereas in vitro it is induced by the addition of model polymer, such as dextran [25, 159].

The effect of dextran addition (two concentration, 1.5 and 3 $mg_{Dextran}/ml_{blood}$) on whole blood viscosity is reported in Figure 2.13.Figure 1.10 It can be noticed that viscosity of blood samples with the addition of dextran is very close to the control one; in fact the two sets of dextran data superimposing to each other and also to the control curve indicating that even small shear rates break aggregates induced by dextran. Nevertheless, a particularity is present in both dextran curves indicating a change of the samples microstructures: a small hump (from 5.6 to 11 s^{-1}) in which viscosity is nearly independent on shear rate. A possible explanation could be the breakage of 3D networks formed at low shear rates due to the fact that shear rates increase from low to high values.

In the inset of Figure 2.13, it has been reported the viscosity curves increasing (down-up curve) and then decreasing (up-down curve) shear rate for sample with 3 $mg_{Dextran}/ml_{blood}$. The lowering of the viscosity in the up-down curve could be attributed to the onset of sedimentation of larger clusters which is related to an increased tendency to form RBC aggregates due to dextran addition. Comparing the trend of down-up and up-down curves in the inset of Figure 2.13 (enhanced aggregation) and Figure 2.1A (whole blood with physiological aggregation) it should be noticed the discrepancy.

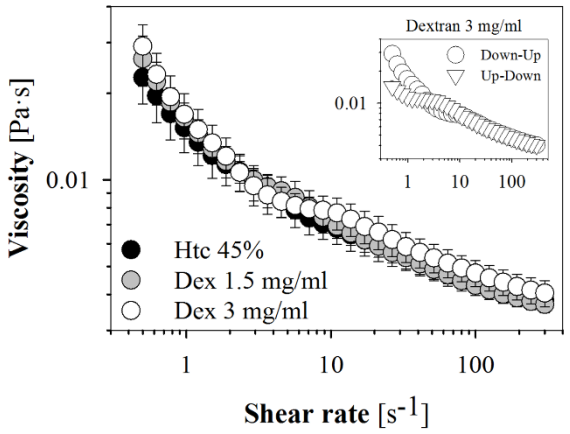

Figure 2.13 - Viscosity as function of shear rate for whole blood master curve and whole blood added with dextran at two concentrations (1,5 and 3 mg/ml). In the inset, circle represents the down-up curve, triangle represents up-down curve [9]. The error bars represent the standard deviation

Regarding the mechanical spectra of RBC suspensions with dextran, Figure 2.14A shows a trend similar to Figure 2.9A; the increase of dextran concentration induces an upward shift of both G' and G'', and in the approach of the them. The presence of an aggregating agent makes G' and G'' more independent on frequency, thus suggesting an elastic-solid like behavior. As report for the Htc dependence, amplitude sweep test have been carried out to characterize the linear viscoelastic region (Figure 2.14B).

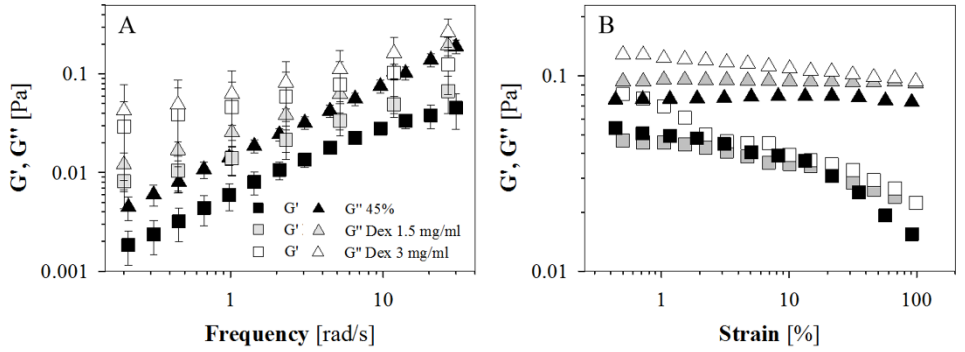

Figure 2.14 - (A) G' and G'' as a function of angular frequencies for whole blood and whole blood with dextran addition at two concentration. (B) Strain amplitude sweep test at 10 for the same samples [9]. The error bars represent the standard deviation

Also in this case, by applying the Cox-Merz rule on the data of Figure 2.13 and Figure 2.14A, a little gap between steady state and oscillatory sets of data is found at low shear rates/frequencies, with complex viscosity values slightly higher than viscosity ones (Figure 2.15). This could indicate that at higher RBC volume fraction it is still possible to find some 3D structures in the low frequency range.

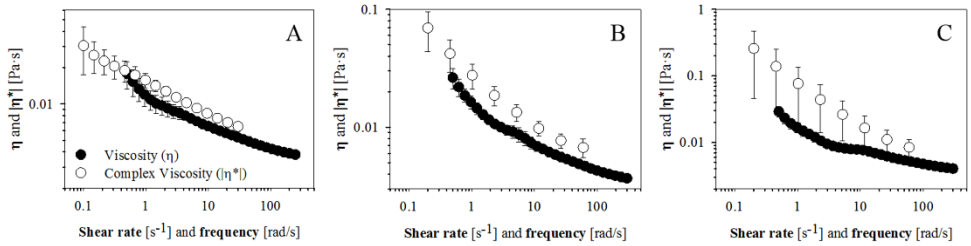

Figure 2.15 - Comparison of viscosity and magnitude of complex viscosity by applying the Cox-Merz rule for (A) Hct=45% and for whole blood added with dextran at 1,5 mg/ml (B) and 3 mg/ml (C) [9]. The error bars represent the standard deviation

In the plot of G'' *vs* G', the three sets of data lie on curves of different slopes. Therefore, the presence of dextran influences the rheological behavior of the samples in terms of microstructure. In fact, for an elastic network, the number of elastically active crosslinks and the concentration of high molecular weight species are strictly related to G' and G''. Moreover, tan δ values decrease with dextran concentration although they are higher than 1 for the two dextran concentration in the entire range of frequency. This confirms that the behavior of RBC suspensions approaches the one of elastic solids when the adhesion strength, promoted by the presence of dextran, increases.

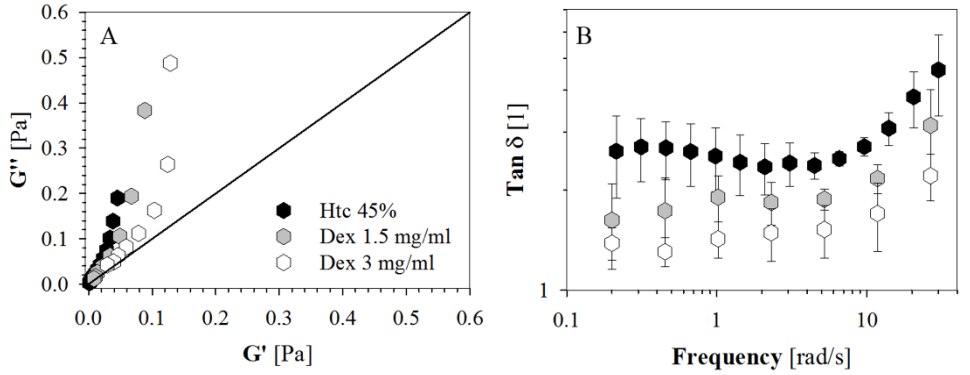

Figure 2.16 - (A) G'' vs G' and (B) the loss tangent as a function of angular frequency for whole blood and whole blood added with dextran at two concentrations (1,5 and 3 mg/ml). The solid line represents the line bisector [9]. The error bars represent the standard deviation

2.3 Summary

In this chapter, an extensive rheological characterization of human blood has been performed.

Firstly, the master curves of flow curve (i.e. viscosity as a function of shear rate) and mechanical spectra (i.e. elastic and viscous moduli as function of angular frequency)

have been obtained in order to have a reference values for whole blood at physiological Htc. For both curves, the experimental protocol was tuned until reaching the best experimental procedure due to the difficult to manage a biological fluid such as blood.

Flow curve shows the typical shear thinning behavior of blood which is intimately related to the dynamics and interactions among RBC.

The main results is the blood linear viscoelasticity characterization by small amplitude oscillatory flow. Elastic and viscous moduli were measured in the range 0.1-30 rad/s and G'' was found to prevail on G'. Amplitude sweep tests suggest that blood microstructure is not significantly perturbed in the linear viscoelastic regime. This would point to the reversible deformation of the RBC network as the main source of blood linear viscoelasticity. However, some authors have related blood viscoelastic moduli at high Hct to RBC membrane rheological properties [160], which is known to exhibit a viscoelastic behavior [161, 162].

The effects of RBC volume fraction and of the addition of dextran have been also investigated under both steady state and oscillatory deformations. The Cox-Merz rule was essentially valid, with some deviations at lower frequencies/shear rates. Regarding RBC volume fraction, a very wide range of Htc values (from 8% to 99%) was characterized. Flow curve data were used to extrapolate yield stress values which are in good agreement with previous works. In addition, the data of this thesis cover an Htc range never investigated before.

The results of this chapter could help in the understanding of blood viscoelasticity although its source is still to be fully understood.

3. Vascular endothelial cells

This chapter describes the methods and experimental protocols developed for the endothelialisation of a microchannel. Cell culture protocols and a home-made perfusion system features are reported. Subsequently, results on cell morphology in static and flow conditions are shown. Staining protocol of GCX is also presented as well as the effect of an enzymatic treatment aimed to the remove negative charge of the GCX.

3.1 Materials and methods

3.1.1 Cell culture

Primary HUVEC (Sigma-Aldrich) was cultured at 37°C in a 5% CO_2 incubator on uncoated tissue culture polystyrene flasks. ECGM (Sigma-Aldrich) was changed every day. After reaching 85% confluence, HUVEC were sub-cultured using trypsin (0.25 % trypsin-EDTA, Sigma-Aldrich). ECGM was removed and cells were gently washed with PBS for few seconds. After discarding PBS, 4-5 ml trypsin was added and gently distributed on the whole flask surface to ensure the solution covers all the cells. After 3-4 seconds, 4.5 ml of trypsin was removed and the flask was put in the incubator for 2-3 minutes. To verify the trypsinization progress, cells were monitored under an inverted microscope until they become rounded. About 5 ml of ECGM was added to the flask to inhibit further tryptic activity. Cells were transferred in conical tube and centrifuged at 1200 RPM for 5 minutes. Supernatant was aspirated from the tube without disturbing the cell pellet which was re-suspended by a desired ECGM volume. By using a Neubauer camera, cells were counted and subsequently placed in new flasks. ECGM was changed every 1-2 days and HUVEC discarded after 8 passages.

3.1.2 Flow chamber

A commercial slide made up of 6 microchannels (µ-Slide VI, Ibidi) were used to apply a controlled flow to HUVEC monolayer. Each microchannel is coated with collagen type IV and has a rectangular geometry with height (h) 0.4 mm, width (w) 3.8 mm, and length (L) 17 mm. The hydraulic diameter of such rectangular ducts is 723 µm.

In steady laminar flow and being h much smaller than w, it is possible to control in a very easy way the wall shear stress acting on the cells. The wall shear stress can be determined using the following equation:

$$\tau = \frac{6\eta Q}{wh^2} \qquad \textit{Equation 21}$$

where τ is the wall shear stress (dyn/cm^2), η is viscosity of the culture medium (Pa·s), Q is the flow rate (ml/s), h and w are the microchannel dimensions.

HUVEC were seeded into the microchannel starting from a suspension of about 10^6 cells/ml. A volume of 60 µl is quickly dispensed in the channel, covering its whole

bottom surface. After 2-3 hours, cells were attached on the bottom side of the channel and ECGM can be added to fill the reservoir of the flow chamber. Cells were cultivated in the incubator for 1-2 days in order to allow HUVEC growth until reaching confluency. A complete medium exchange was made every 24 hours.

3.1.3 Perfusion systems set-up

HUVEC were subjected to shear stress stimulation through custom made flow setup shown in Figure 3.1. Two different perfusion systems, namely A and B, have been developed. The flow circuits are closed and ECGM is pushed through the tubes by the action of a peristaltic pump.

The system A is shown in Figure 3.1; starting from point A, the ECGM enters the system and arrives on the HUVEC monolayer into the Ibidi flow chamber. After that, the fluid flows into the pump, passes through a Y-junction and returns in the reservoir. Tubes are made of PVC or Teflon, and have an ID of 1/16".

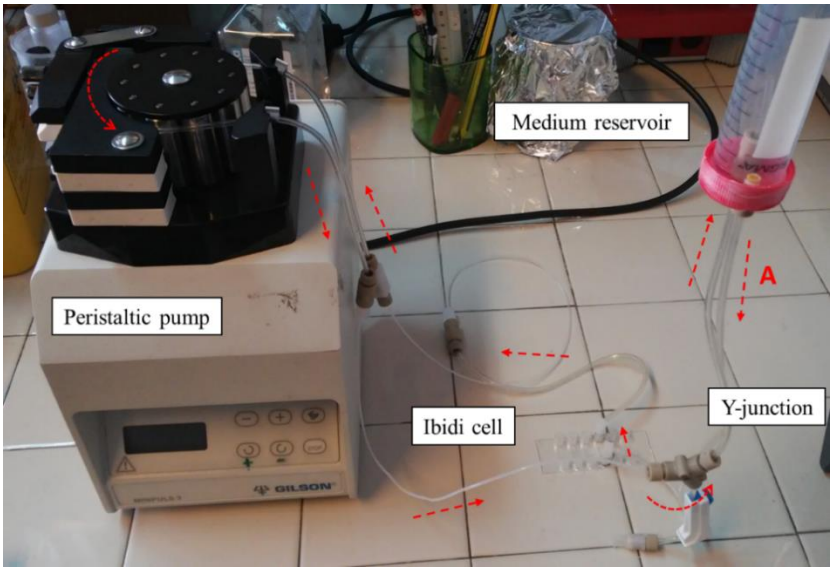

Figure 3.1 - Perfusion system A

One of the main problem with such systems is the formation of air bubbles which can be pushed into the tubing system causing damage to the cells. For this reason the reservoir was placed upside, so any air bubble that is formed goes upward (Figure 3.2A); the feeding tube is located on the bottom and the drain tube is placed in an upper position.

A Y-junction was added just before the reservoir in order to foresee the possible addition of fluids, without the need to stop the experiment. A valve allows the coupling to the system when necessary; in addition, a syringe adapter is provided in order to connect common plastic syringes (Figure 3.2B).

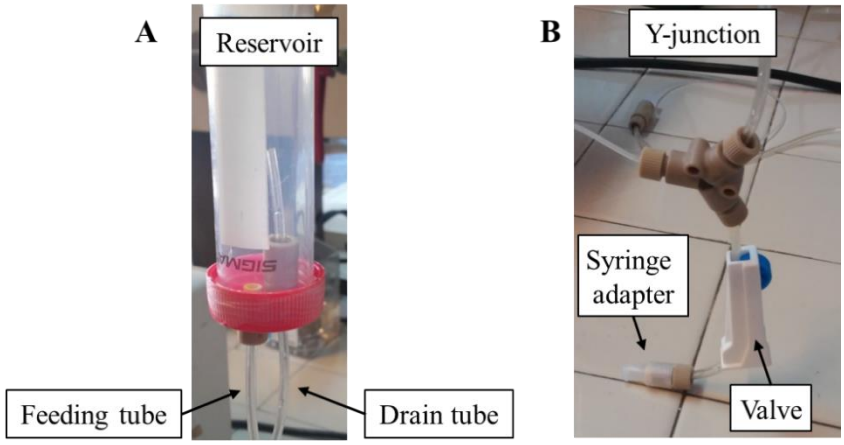

Figure 3.2 - Details of (A) reservoir and (B) Y-junction

The perfusion system B presents the same features of system A, except for the ID which is 1/8" and for the total tube length. Moreover, peristaltic pump is different allowing higher RPM values.

3.1.4 Perfusion systems characterization

The systems were calibrated for predicting the relation between RPM and flow rate. In order to calculate the flow rate, a solution of 1 µm polystyrene beads (Polybead, Polysciences) was pumped through the system. The flow chamber was placed on an inverted microscope and images were acquired for data analysis. Average beads velocity was obtained by tracking the positions frame by frame at the centre of the channel (i.e. the fluid streamline are constant) for at least 20 beads. The velocity was determined by plotting the bead displacement as a function of time. As expected, these plots were linear and the slope was taken as velocity. Then, flow rate was calculated multiplying the average beads velocity for the channel area. A calibration curve is reported as an example in Figure 3.3.

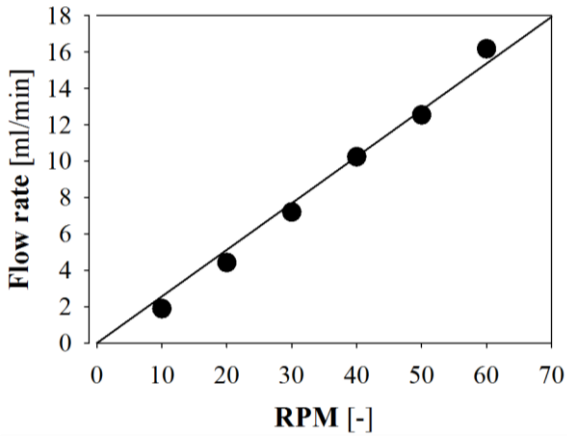

Figure 3.3 - Perfusion system B calibration

During the experimental campaign, systems A and B were implemented continuously (e.g. tubing length was modified, components position were changed, etc.). For each perfusion system, a separate calibration curve was measured. The maximum flow rate achievable is about 5 ml/min for system A and about 16 ml/min for system B. In some cases, calibration curves were calculated by weighing the volume of liquid pumped at fixed intervals.

In addition, at the maximum flow rate achievable with the systems, Reynolds number, entrance length and pressure drop were calculated (Table 1). Re values indicate that the experimental conditions ensure the laminar regime in the microchannel. The fully developed flow is at 1.10 and 4.11 mm respectively for system A and B from the inlet of the microchannel which is 17 mm long; every experiment was carried out beyond such values. Pressure drops are negligible being in the order of magnitude of mbar.

	System A	**System B**
Re	34.4	128
L_e *[mm]*	1.10	4.11
ΔP *[mbar]*	6.10	1.67

Table 1 - Reynolds number, entrance length, and pressure drop for both systems

3.1.5 Flow experiment

Once HUVEC reached confluency in static condition, shear stimulation was applied. Before starting the experiment, the whole system and the ECGM were equilibrated overnight in the incubator in order to avoid the formation of gas bubbles over time.

Flow chamber, medium reservoir and tubing were placed inside the cell incubator while the peristaltic pump was placed outside close to the incubator.

Cells were incubated under either static conditions (no shear) or shear stress for up to 8 days. The steady shear stress applied was of 19 dyn/cm^2, which is a typical value of human circulatory system [163].

3.1.6 Microscopic imaging and cellular morphology analysis

Greyscale TIFFs images of HUVEC in static and under flow conditions have been captured by using an inverted phase-contrast microscope (Nikon) equipped with 10x and 20x objectives.

Image analysis was carried out by using a commercial software package (Image Pro Plus 6.0). The morphology of single cells in the monolayer was detected automatically by subjecting images to contrast enhancements and smoothing functions to optimize cell border (Figure 3.4A). Subsequently, a threshold was applied to binarize the image, removing small particles and artefacts (Figure 3.4B). Measurement tools allow to count each cell and characterize several morphological parameters such as areas, perimeters, lengths, major and minor axes, angles etc. (Figure 3.4C). Objects having area less than 50 piexl^2 were automatically excluded.

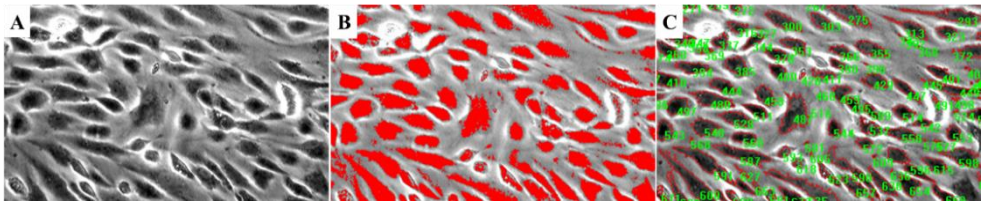

Figure 3.4 - Image analysis process. (A) Image with contrast enhancement, (B) threshold application, (C) cell count

The orientation angle (ϑ) of the cells subjected to shear flow was measured considering the angle between the major axis of the cell and the orthogonal direction to the flow (Figure 3.5A). Figure 3.5A reports two examples: cell A presents an orientation angle ϑ_A of about 65° while cell B of about 105°. The value was calculated automatically with Image Pro Plus, as reported previously. By using *the polar plot function* of Matlab routine, the width of the channel has been divided into 25 equal slices of 7.2° each one (Figure 3.5B) in order to cover the whole angle range (0-180°). By this way it is possible to associate each cell angle into the appropriate slice obtaining an angle histogram in polar coordinates which gives information on how cells orientation is distributed along channel width.

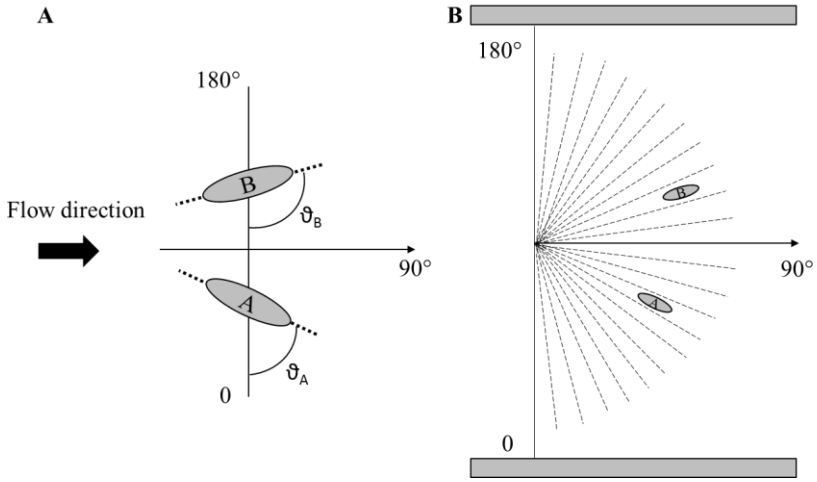

Figure 3.5 - (A) Scheme of the orientation angle calculation. Shapes A and B are two examples of cells with their angle calculation. (B) Partitioning of the channel width

Moreover, shape index was evaluated by using the following formula for each cell:

$$SI = \frac{4\pi A}{P^2} \qquad \textit{Equation 22}$$

where A is the cell area, and P is the length of the cell perimeter. Thus, SI values range from 0 for a straight line to 1 for a perfect circle. Area and perimeter were evaluated automatically.

Immunofluorescent staining of the GCX was obtained by using WGA-Alexa Fluor 488 (Molecular Probes), which excites at 495 nm and emits at 519 nm. WGA is a lectin that binds to SA an important component of endothelial GCX [164]. Cells were washed twice with PBS and then a WGA solution (0.01 mg/ml) was applied to live cells for 30-40 min at 37°C. Before visualization, another washing step was done.

The characterization of GCX layer was carried out with a CLSM (Leica TCS SP5). All CLSM images (512x512 pixels, 8 bit pixel depth) were acquired using a Leica HCX PL APO CS 63×1.4 NA oil immersion objective. To observe WGA specificity, an argon laser (λ=488 nm) was used in conjunction with a long-pass filter (λ=505 nm).

GCX contribution was assessed via enzyme digestion. HUVEC monolayer was incubated with 2.5 U/ml neuraminidase (Sigma-Aldrich) for 30 min at 37°C while the control group was kept in the ECGM. After incubation, PBS was used to wash the HUVEC twice before images acquisition.

In order to quantify the expression of GCX in cells in different experimental conditions, a z-stack was recorded from their apical to basilar surfaces. Then, the slices with the maximum mean fluorescence intensity was chosen for the quantification. To compare all samples, value of fluorescence intensity was normalized respect to the gain value, chosen during acquisition.

3.2 Results

3.2.1 Morphological analysis

HUVEC seeded in Ibidi microchannel were either kept in static culture conditions or exposed to shear at 19 dyn/cm^2 up to 8 days into cell incubator. Cells were cultured until a confluent monolayer for at least one day before the start of shear experiments. Ibidi slide allows to culture up to 6 microchannel simultaneously; another microchannel in which fresh ECGM was added and replaced every day during the subsequent days was used as control. Images of HUVEC under flow were acquired every day (Figure 3.6). The flow direction is from left to right and wall shear stress applied is 19 dyn/cm^2 which is typical value of arterioles and venules in human body [163]. It can be observed that HUVEC in static conditions are randomly oriented throughout the channel. On the other hand, the orientation of cells along flow direction increases as the days passes. Moreover, while there is not a significant morphology change after three days, from the fourth day the elongation is considerable. After eight days, HUVEC are completely elongated in shape and well aligned to the flow direction.

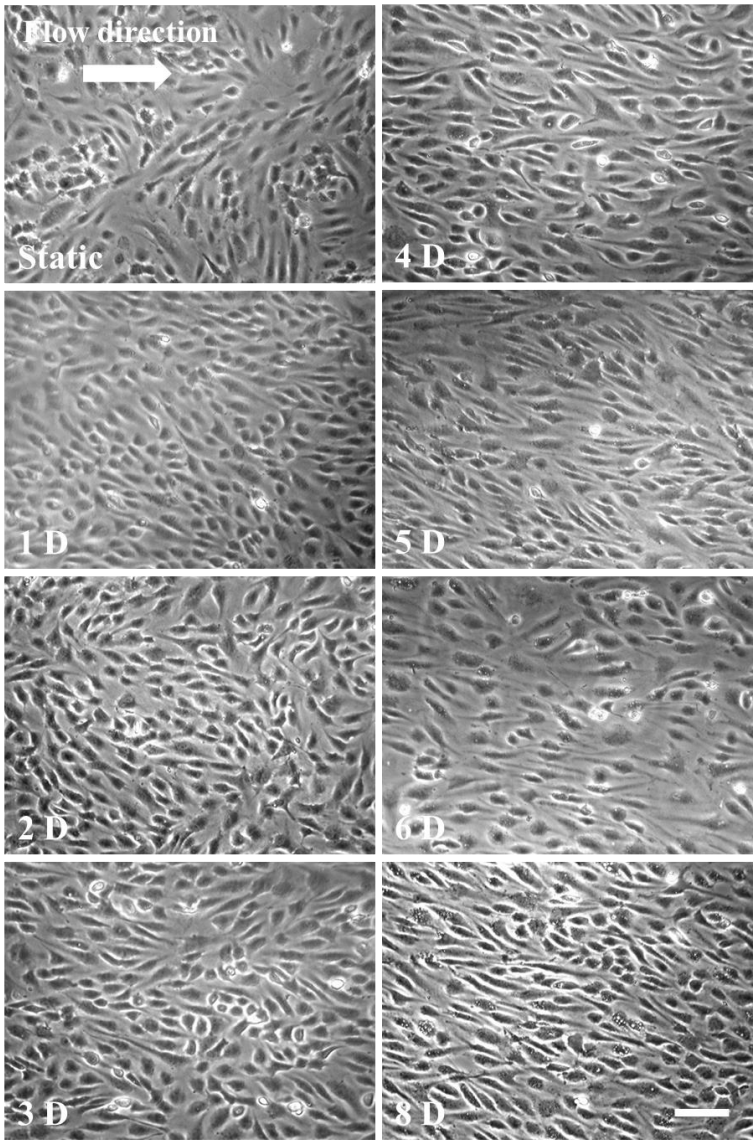

Figure 3.6 - Images of HUVEC under flow for eight days. Flow direction is from left to right. Objective 10x. Scale bar 100 µm

In order to quantify morphological parameters in Figure 3.6, a histogram plot in polar coordinates was created according to method in paragraph 3.1.6 (Figure 3.7). Polar plot is made of 25 slices of 7.2° each one. The red axis indicates the percentage of cells in a slice (e.g. 10 indicates 10% of all cells). Orientation angles of cells are distributed into belonging slice and plotted as relative frequency. Images were captured at multiple locations along the length of the microchannel resulting in at least 300 cells acquired for each day.

HUVEC in static condition are randomly oriented as can be observed from the open fan typical of a uniform distribution of values. Already after one day, an appreciable

alignment in the direction of flow is present, as already reported in previous works [165, 166]; about 80% of cells are in the range 60°-120°. The percentage of cells aligned in the flow direction increase as days pass. After 8 days, all cells show orientation angles in the range 60°-120°.

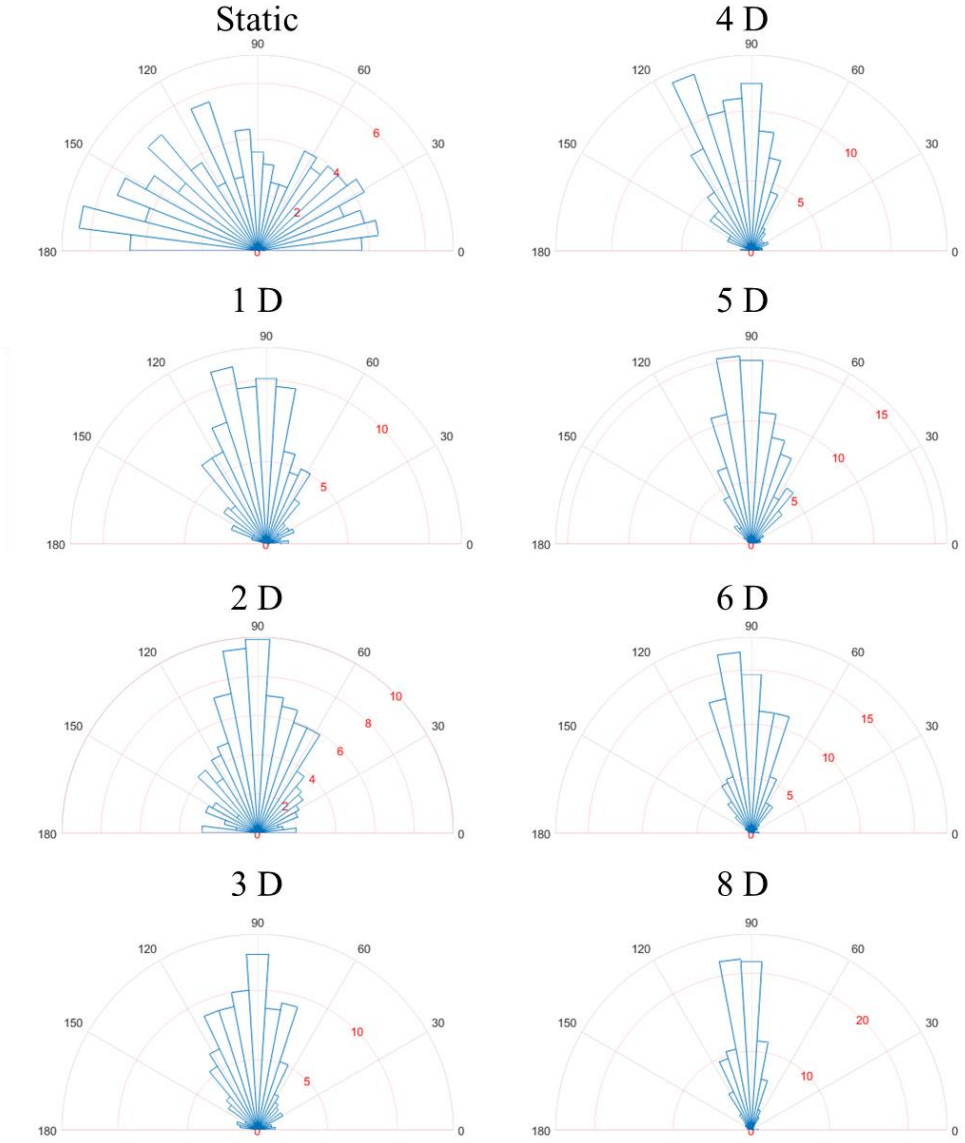

Figure 3.7– Polar plots of orientation angles. Flow direction is at 90°

The SI was evaluated following the Equation 22. In Figure 3.8, each point represents the SI of a cell. In static conditions (Figure 3.8A), SI values are randomly distributed between 0 and 1 indicating that cells have shapes ranging from elongated to rounded respectively. The average value (grey line) is about 0.5. On the other hand, after 8 days under flow (Figure 3.8B), a significant decrease of the SI is observed.

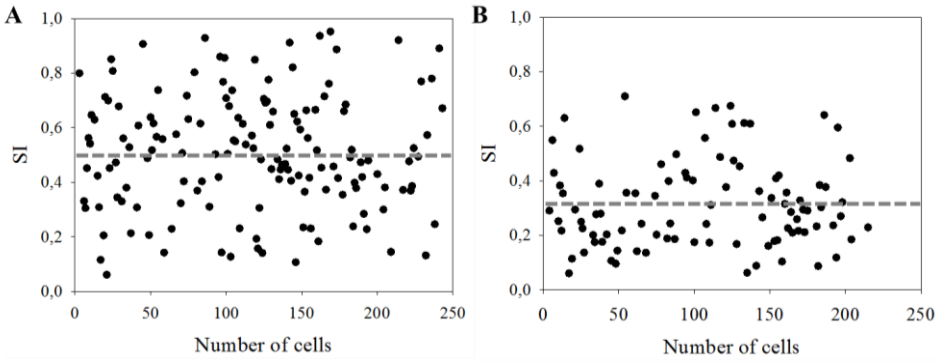

Figure 3.8 - SI counting for cells in static condition (A) and after 8 days under flow (B). Each point represents the SI value of a cell. Grey line highlights the average value of the SI

The average values of SI are reported in Figure 3.9. SI value is almost constant until the fifth day. A slight decrease is noticeable on the sixth day, while a further significant decrease is observed on the day 8; in fact, a statistically significant difference of the SI is detected between static and 8 days (P value≤0.001). Thus, it can be possible to assert a cell stretching after 8 days under flow.

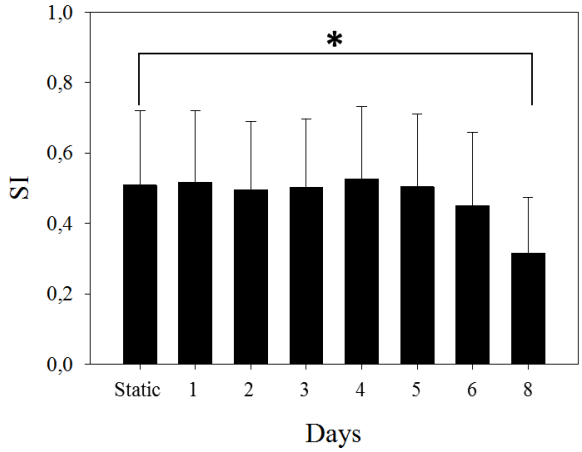

Figure 3.9 - Mean SI for all days. The difference between the sets of data in static and 8D is significant (P value≤0.001). The error bars represent the standard deviation

3.2.2 GCX characterization

Among the wide number of components of GCX (someone is still unknown), SA is the most commonly observed components and it is used as representative of the entire GCX [167]; SA is specifically bound by WGA.

In Figure 3.10A and Figure 3.10B, static and sheared cells, the latter subjected to 19 dyn/cm^2 for 8 days, have been stained by WGA. It is evident, as already demonstrated in Figure 3.6, that flow induces a strong change in the morphology of cells, which appear more elongated in the flow direction. Staining protocol results efficient in both cases, and has allowed the estimation of the thickness of the cell monolayer by a z-stack acquisition.

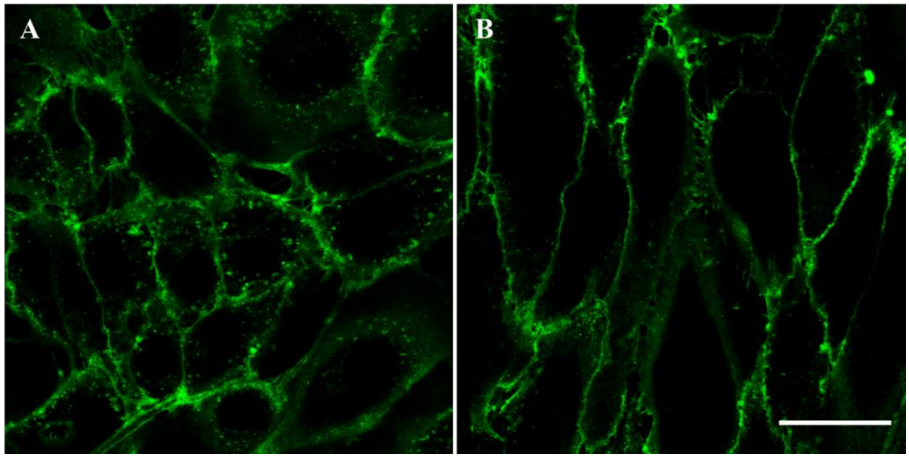

Figure 3.10 - Confocal images of HUVEC in (A) static (B) sheared conditions. Flow direction is from bottom to top. Green=SA stained by WGA. Scale bar 35 µm

From 3D reconstruction (Figure 3.11B), it is possible to observe that elongated cells show a finer monolayer compared to static cells (Figure 3.11A). In fact, observing planes x-z and y-z, the different thickness of the cells in the two cases is evident; sheared cells present thickness of about 5 µm whereas the static ones about 9 µm. The thickness has been calculated as the distance from the apical to basal surface. Moreover, the x-y plane shows the enface image at a given z depth that confirms the elongation in the direction of flow of the sheared cells compared to the static ones. Furthermore, the wavy fluorescent profile in the ortho images is indicative of the high specificity of WGA for molecules on the cell membrane. It is worth mentioning that working with cell culture is very complex and is almost impossible to recreate the same conditions.

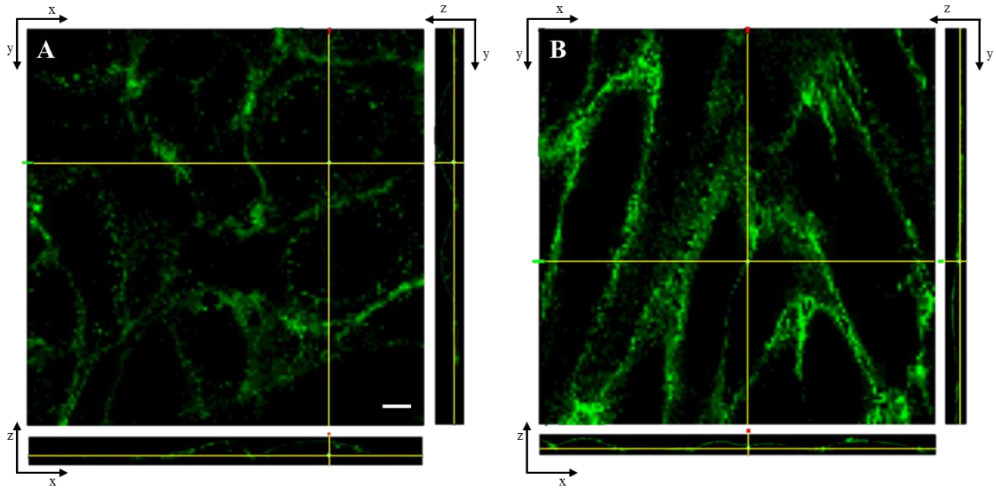

Figure 3.11 - 3D confocal ortho reconstruction of static (A) and sheared cells (B). Flow direction is from bottom to top. Green=SA stained by WGA. Scale bar 10 µm

Cells under flow has been then treated by the addition of an enzyme that cleaves SA (i.e. the component that gives the negative charge) on the GCX. The aim of this experiment is to investigate a possible key role of SA in the flow behavior of RBC. Being this component stained by WGA, the treatment with enzyme should influence the value of the fluorescence intensity, which could only due to the SA residues. Normalized mean fluorescence intensity has been calculated as reported in paragraph 3.1.6. Such experiments have been performed on aligned cells after eight days under flow.

A comparison between sheared cells, before and during treatment and after two washes with PBS has been shown in the histogram in Figure 3.12; in addition static cells without enzyme treatment has been reported as a control. Firstly, it can be seen that fluorescence value of sheared cells results double than the static ones. Such result leads to the consideration that in static conditions the GCX is not fully developed while the flow induces the highest expression as reported in previous works [168, 169]. Regarding enzyme treatment, it is clear that when enzyme acts, a decrease in the fluorescence intensity is noticeable, already during its action. Washing with PBS does not affect further the intensity which present a similar value. Although the fluorescence decreases, it does not reach zero because enzyme fails to cleave all SA. Measurements have been performed on three different fields of view and results are in good agreement, as visible from small error bars.

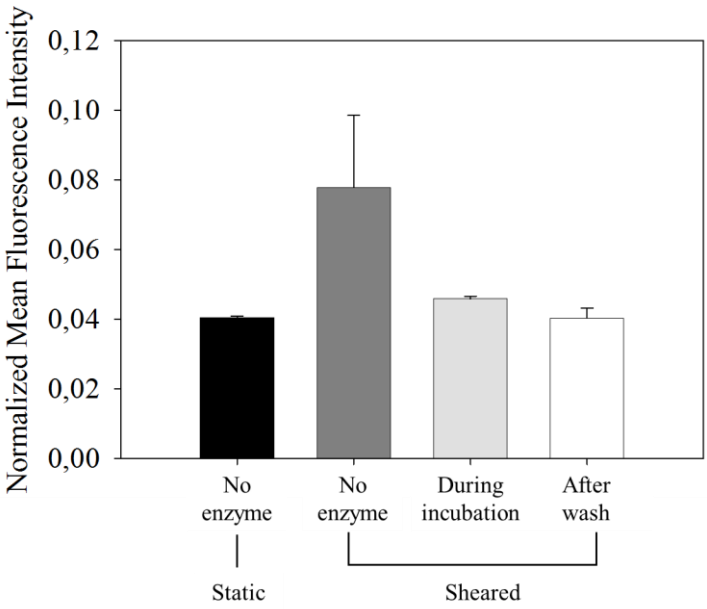

Figure 3.12 - Histogram of the normalized mean fluorescence intensity HUVEC in static (black), sheared before enzyme treatment (dark grey), sheared during enzyme incubation (light grey), and sheared after enzyme treatment (white). Mean values are calculated on three fields of view. The error bars represent the standard deviation

3.3 Summary

In this chapter the morphological characterizations of HUVEC in static and under flow condition have been performed.

The experimental protocol for endothelialisation of a microchannel has been developed either for the cell culture or for the reproduction of relevant physiological condition *in vitro*. Particular focus has been aimed to guarantee appropriate cell conditions up to 8 days. The wall shear stress applied was 19 dyn/cm^2, a typical value of human vasculature.

The monitoring of cell monolayer has been possible by acquiring images every day. Results show that orientation angle of cells has already been evident after one day under flow. As the experiment progressed, the percentage of cells orientated in the flow direction increase, reaching the maximum after 8 days; here all cells present orientation angle in the range 60°-120°.

The effect of flow on the shape index has been also evaluated. Values indicates that a significant elongation of cells is evident after the eighth day.

Finally, a quantification of the fluorescence intensity has been carried out by using CLSM in order to highlight the expression of GCX under static and flow conditions. One of the main GCX components (i.e. SA) has been selectively bound by WGA. Fluorescent images confirm the different cell morphology between static and flow condition and give information regarding cell thickness. In fact, it has been reported in ortho reconstruction that cells under flow are thinner than static ones, 5 and 9 µm respectively. In addition, GCX electronegativity has been reduced via enzymatic digestion of sialic acid.

Several techniques have been used to estimate GCX thickness and structure [170] although the most widely adopted is the CLSM [164]. Such approach is questionable due to the technical limitation of the CLSM; in fact, its maximum axial resolution is 0.7 µm which is a value very close to the supposed GCX thickness [103]. Recently, super-resolution microscopy has been used to characterize GCX dimension which has estimated in 1.33 µm [171]. However, it is necessary to emphasize that this is the only work that uses super-resolution microscopy for GCX investigation.

4. RBC-endothelial cells: flow assay

This chapter reports experiments aimed to examine the role of endothelial cells in RBC flow behavior. Firstly, the preparation procedures of the samples and the subsequent image analysis details are reported. Velocity profiles of hRBC suspension along the channel width and height are discussed. Moreover, the possible influence of the GCX is evaluated. Finally, preliminary results of *Plasmodium falciparum* infected RBC are reported.

4.1 Materials and methods

4.1.1 RBC samples

RBC were processed following the standard protocol for hemorheological tests [142]. Fresh venous blood samples were drawn from healthy donors and collected into Vacutainers (BD) containing EDTA. First blood was centrifuged at 1,600 RPM for 15 minutes to separate RBC from plasma; after centrifugation plasma and buffy coat were gently aspirated. Then, RBC were washed twice with PBS obtaining a pure RBC suspension without platelets, white blood cells and plasma proteins. RBC were stored at 4°C until the experiment began and used within 6 h of collection.

A solution made of ACD (0.6% citric acid, 2.3% sodium citrate, 1.1% anhydrous dextrose and 96% water) and bovine serum albumin (1 g of albumin in 5 ml of PBS) was used as suspending medium. ACD is mainly used as an anticoagulant to preserve blood whereas albumin is the most abundant blood plasma protein and it is useful to regulate the osmotic pressure of the medium. RBC viability was checked before each experiment by observing cell morphology under static conditions at high magnification.

RBC volume fraction was selected depending on each experiment. Htc values was varied from 0.5% to 10%; the latter was selected to match the Htc value in microcirculation [172]. Diluted blood samples were necessary during acquisition along the microchannel height; in fact higher Htc values did not allow the penetration of the light into the sample.

4.1.2 Malaria

Malaria infected cells by *Plasmodium falciparum* species were kindly provided by Pietro Cicuta's group at the University of Cambridge (UK). iRBC were cultured under a low-oxygen atmosphere by standard methods reported in Crick et al. [173], and Tiffert et al. [174]. IRBC were incubated at 37°C in growth medium (RPMI-1640 supplemented with 0.5% AlbuMAX II, Sigma-Aldrich). The medium was changed every day and healthy cells added appropriately to avoid saturation of parasitized cells. Htc in culture flasks was 1-2% while parasitemia (percentage of iRBC compared to hRBC) at most 5%. Cultures were routinely synchronized in order to keep the parasites within a narrow stage range.

IRBC was labelled with Hoechst 33342 (Molecular Probes), a fluorescent dye that stains double strand DNA of living cells. Hoechst was added to iRBC at a concentration of 200 µg/ml and incubated for 30 minutes.

4.1.3 Vascular endothelial cells

Vascular endothelial cells were prepared as described previously (chapter 3). In order to recreate physiological conditions *in vitro*, primary HUVEC were cultured into Ibidi microchannel in static condition until a monolayer is formed. After that, a perfusion system was connected to the microchannel in order to apply a shear stress stimulation on the monolayer inducing cell alignment. The experiments of this chapter were carried out with HUVEC subjected to a steady shear stress of 19 dyn/cm^2 for 4 days.

4.1.4 Experimental apparatus

Images of the flowing RBC suspensions were captured with a Zeiss Observer Z01 equipped with a high-speed video camera (Phantom v711) using 20x, 40x and 100x objectives. The microscope was provided with a programmable motorized x-y-z stage that allows the movement of the sample to the desired position. For the experiments with malaria iRBC, an ATI-Eclipse inverted microscope (Nikon) was used. It was placed in a custom-built temperature-control stage to maintain the optimal culture temperature of 37°C during imaging experiments. Videos were acquired with an AVT Pike F100B camera at frame rate ranging from few fps up to 300 fps depending on the size of the acquisition window.

RBC suspensions were fed in the microchannel by using syringe pumps (Harvard Apparatus) by which it was possible to impose the desired flow rate. Moreover, knowing the geometry of the channel, it is possible to calculate the corresponding wall shear stress. Reynolds number, entrance length, and pressure drop were calculated in the microchannel at the maximum flow rate used for the experiment with RBC suspensions (Table 2). Reynolds number value ensures a laminar flow in the microchannel and it is a physiological value of arterioles. All data were obtained after 4.9 mm from the inlet of the channel (entire channel is 17 mm) in order to guarantee the fully developed flow. The pressure losses in the whole system are negligible.

Re	153.4
L_e *[mm]*	4.9
ΔP *[mbar]*	0.21

Table 2 - Reynolds number, entrance length, and pressure drop at maximum flow rate

Velocity profiles were obtained by a tracking procedure carried out by Image Pro Plus. It consists in a manual selection of the RBC whose x-y position is recorded by the software. This procedure is repeated for at least 20 RBC in the image and for at least 10 consecutive frames. Each position of RBC is automatically marked to facilitate the identification of the next position (Figure 4.1). Cell positions were plotted as a function of time, allowing the estimation of the RBC velocity (i.e. slope of the plot).

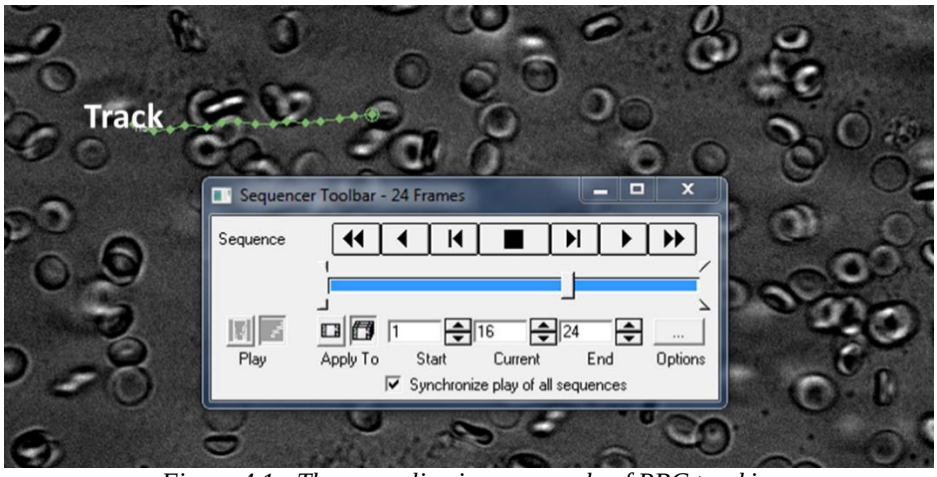

Figure 4.1 - The green line is an example of RBC tracking

The RBC velocities were stored and exported for subsequent data analysis. For each flow rate, at least 3 fields of view were recorded and the average value is reported in the following plots. The error in the manual image analysis was taken into account by tracking the same RBC several times and it resulted negligible, being about 0.3 μm for both x and y coordinates.

The acquisition procedure is affected by the refractive index of the oil between the front lens and the specimen cover glass (RI 1.52) and that of the suspending medium (RI 1.33). All data were hence corrected considering these values.

Due to the time consuming procedure to acquire the entire channel width and height, data were acquired on the half of each dimension. For the channel width, two fields of view were acquired: the former close to the channel wall and the latter in the centreline. Regarding axial dimension, the entire half-height was explored. In both cases, data were acquired on the first RBC layer in focus starting from the bottom of the channel.

To better visualize the velocity profile, data were reversed symmetrically respect to the centreline. It should be emphasized the importance of the acquisition position along the channel height because it can strongly influence the results.

4.2 Velocity profiles along channel width

The experimental velocity profiles along the channel width have been obtained by tracking and measuring the velocity of individual RBC flowing in the microchannel at a fixed height. The Htc has been chosen at 10% which is a physiologically relevant conditions. More concentrated suspensions have been tested but the turbidity of the sample has not allowed a clearly defined image acquisition.

The velocity profiles as a function of the channel width are reported in Figure 4.2 in which each point represents the velocity of a RBC. Figure 4.2A refers to bare channel, i.e. without endothelial cells, while Figure 4.2B refers to a channel with a HUVEC monolayer on the bottom without shear stimulation. As expected, for both cases it is possible to observe a flat (plug-like) fluid velocity profile and increasing wall shear stress induces a shift upward of the velocity values.

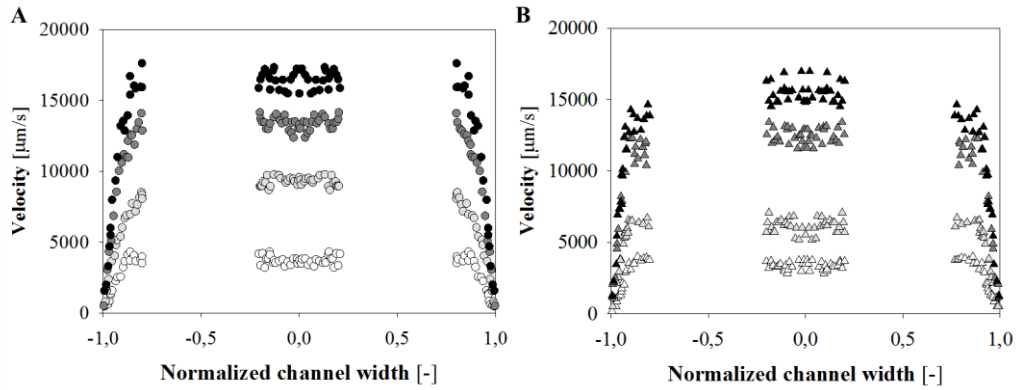

Figure 4.2 - Experimental velocity profile along the channel width in (A) bare and (B) endothelialized channel. Black=14.3 Pa, dark grey=10.7 Pa, light grey=6 Pa, white=3.6 Pa

A comparison between average values in the middle of the channel is reported in Figure 4.3. As visible, RBC velocity in bare channels has been always higher than endothelialized ones. The percentage difference for each wall shear stress are reported on the bars; excluding 6 Pa which seems to be unreliable, the decrease varies from 5.9% to 8.9%.

This results is reasonable if compared with previous fluid dynamic characterizations of small microcapillaries lined with polymer brushes [110]. A decreasing in RBC velocity in coated microchannels is expected compared to bare microchannel due to the dissipation caused by the presence of the brush. This observation can be extended to the case of a bigger channel such as in this work.

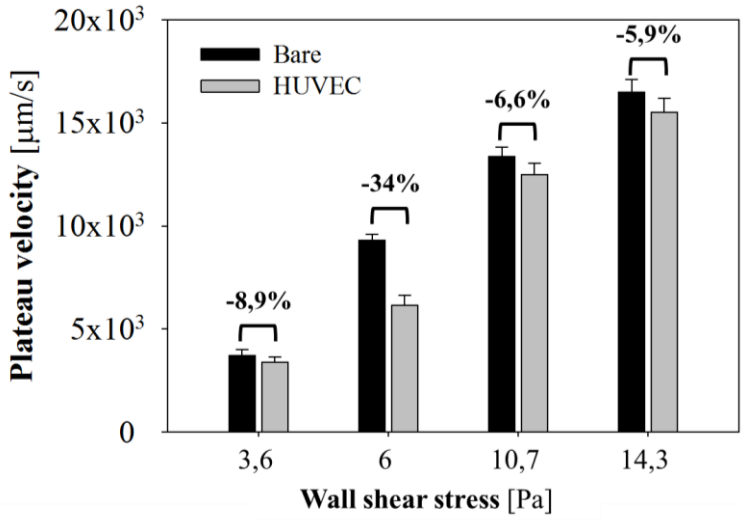

Figure 4.3 - Plateau velocity as function of wall shear stress for bare (black) and endothelialized (grey) channel. The error bars represent the standard deviation

By using Equation 19 it is possible to calculate the resistance to flow of bare and endothelialized channels. In the latter case, the HUVEC monolayer is approximated to a

flat surface having height half than the height of a single cell which has been estimated in 9 µm (see paragraph 3.2). Therefore, the channel with the HUVEC monolayer has a height of 395.5 µm instead of 400 µm. The resistance to flow results $1.79x10^{12}$ kg/m^{4}s and $1.88x10^{12}$ kg/m^{4}s for the bare and endothelialized channel respectively. The percentage difference is of 5% which is a value slightly lower than the velocity difference; thus the reduction of the channel lumen is not the only reason for the decreasing of the velocity. This discrepancy could be due to biochemical factors induced by the HUVEC monolayer.

4.2.1 GCX contribution

In order to investigate the possible role of GCX in the RBC flow behavior, HUVEC have been treated with neuraminidase (see paragraph 3.1.6). The enzyme cleaves selectively sialic acid which is responsible for the negative charge of the GCX.

Figure 4.4 shows the comparison of the plateau velocity for HUVEC untreated, i.e. used as control, and treated with enzyme. In both cases, cells have been subjected to a wall shear stress of 19 dyn/cm^2 for 4 days. It is not possible to appreciate a significant difference between control and enzyme treated sample leading to the conclusion that the GCX charge does not influence RBC flow behavior.

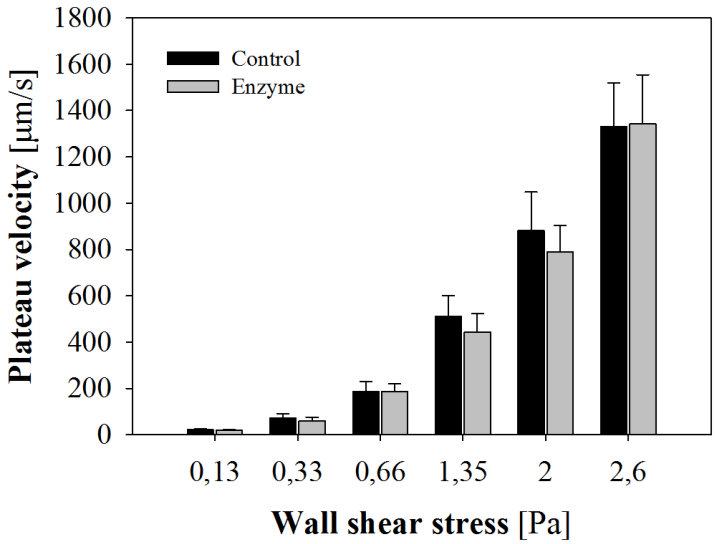

Figure 4.4 - Plateau velocity as function of wall shear stress for untreated HUVEC (black, control) and neuraminidase treated HUVEC (grey, enzyme). The error bars represent the standard deviation

4.3 Velocity profiles along channel height

Images at different axial position were captured on diluted blood samples to allow the path of light enters into the sample. In these experiments, blood has been tested at Htc value of 0.5%. Acquisitions have been carried out at different penetration depth by using a motorized microscope having axial resolution in the order of magnitude of few nanometres. Thus, the height was imposed automatically at fixed depth and two

magnification has been used, i.e. 100x and 20x. The latter was necessary to capture images in the middle of the channel (e.g. 200 µm from the bottom of the channel).

Velocity profiles as a function of the normalized channel height are reported in Figure 4.5A for bare channels and Figure 4.5B for endothelialized channels at four wall shear stress. The parabolic profile is evident and it is in agreement with the fluid dynamic theory being h<<w. By a first qualitative observation, a very similar trend between bare and endothelialized channel is noticeable.

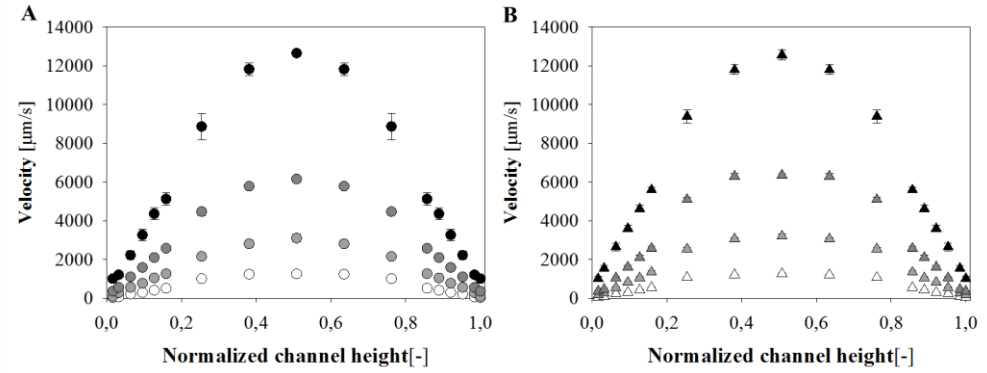

Figure 4.5 - Experimental velocity profile along the channel height in (A) bare and (B) endothelialized channel. Black=1.3 Pa, dark grey=0.66 Pa, light grey=0.33 Pa, white=0.13 Pa

Figure 4.6 reports the comparison between bare and endothelialized channel at 0.13 Pa (Figure 4.6A) and 1.3 Pa (Figure 4.6B). No significant differences are appreciable in the velocity profiles indicating that endothelial layer do not influence the flow behavior of RBC in the microchannel investigated.

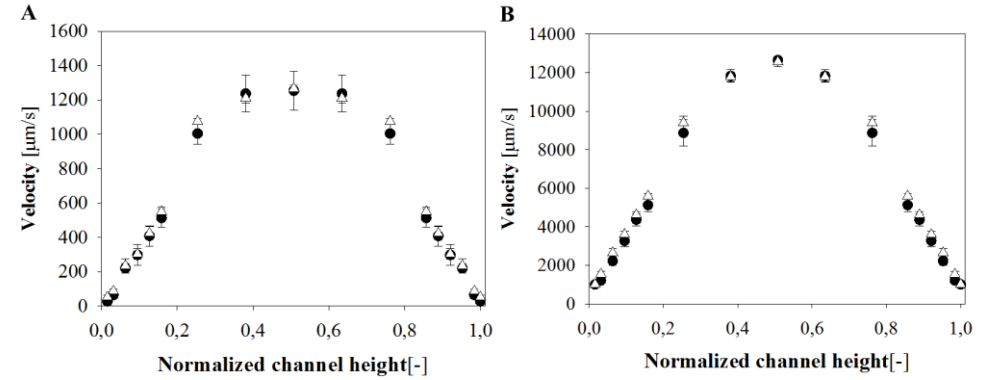

Figure 4.6 - Experimental velocity profile along the channel height in (A) at 0.13 Pa and (B) at 1.3 Pa. Black dots refers to bare channel, white triangle to endothelialized channel

4.4 Interaction between *Plasmodium falciparum* iRBC and endothelial cells

Here, preliminary results on *Plasmodium falciparum* iRBC flowing on HUVEC monolayer have been reported. Results reported in this paragraph have been achieved in collaboration with the Cicuta's group at University of Cambridge (UK).

Suspension of iRBC-hRBC were prepared at Htc of 0.5% and parasitemia up to 5%. HUVEC were aligned under flow as described previously and GCX was removed when necessary. In the experiments reported, only early stages iRBC have been considered and investigated.

iRBC can be easily identified by black dots visible into the cell. Examples of iRBC are reported in Figure 4.7A and Figure 4.7B. Identification of iRBC is facilitated when the sample is extremely diluted (i.e. Htc less than 0.1%) causing a reduced overlapping of cells. It becomes more difficult during experiments at Htc higher than 0.5% due to sample turbidity. For this reason, malaria parasite has been labelled with Hoechst 33342 which detects nuclear DNA (Figure 4.7C, red arrows). It is important to note that during flow experiments, unbound Hoechst into blood sample labels also HUVEC nucleus (Figure 4.7C, green arrows). However, this effect results useful to identify HUVEC clearly. Although the staining of malaria parasite has been previously reported in the literature [175, 176], this is the first time that the flow behavior of iRBC on endothelial cell monolayer is reported.

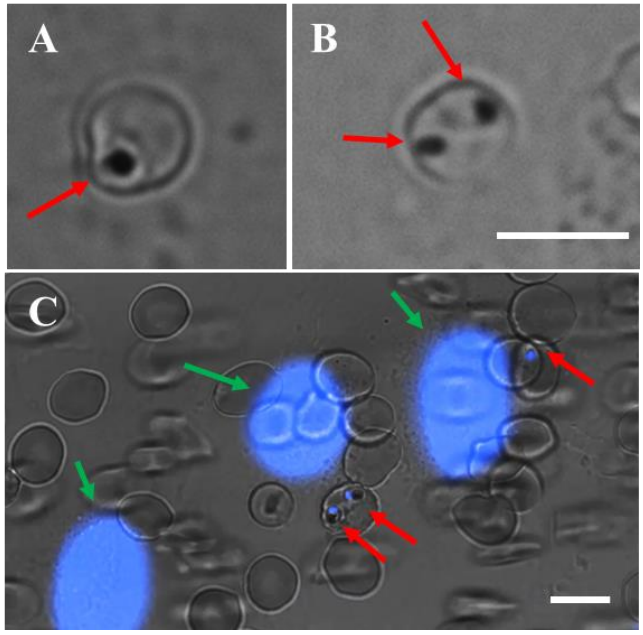

Figure 4.7 - two iRBC by one (A) and two (B) parasites. (C) DNA labelling of HUVEC nucleus (green arrows) and malaria parasite inside RBC (red arrows). Scale bars 10 µm

HUVEC treated and untreated with neuraminidase and both iRBC and hRBC have been considered for the analysis. Plateau velocity of iRBC-hRBC suspensions are reported in Figure 4.8. As in the case of hRBC (paragraph 4.2.1), no statistical difference can be noticed between treated and untreated cells. Moreover, data suggest that the overall behavior of the iRBC-hRBC suspension is not affected by the presence of iRBC. This is reasonable due to the low concentration of iRBC, i.e. parasitemia at most 5%.

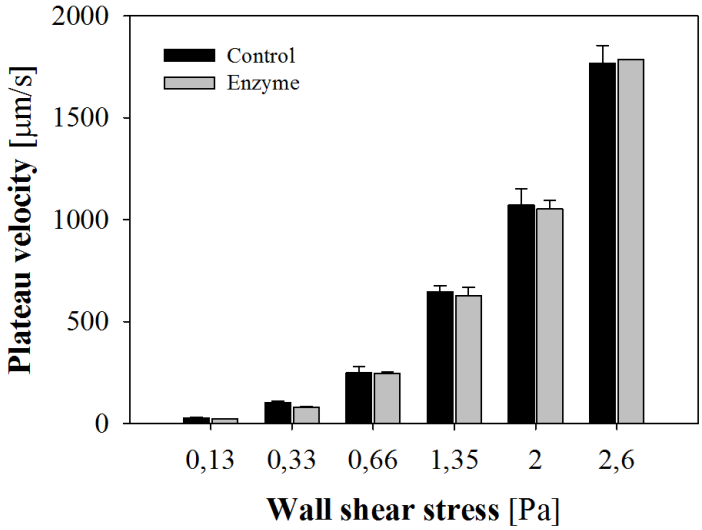

Figure 4.8 - Plateau velocity of iRBC suspensions as a function of wall shear stress for untreated HUVEC (black) and neuraminidase treated HUVEC (grey). The error bars represent the standard deviation

Focusing on singles RBC, dynamics of hRBC and iRBC flowing on a HUVEC monolayer are shown in the snapshot of Figure 4.9A and Figure 4.9B respectively. The applied wall shear stress was 0.13 Pa and the time between each frame was of 0.5 seconds in both cases. The hRBC glides on the HUVEC layer in a tank-treading motion while the iRBC flips on the cells. After 2 seconds, the latter makes a complete revolution on itself. Such behavior is very similar to simulation data reported by Fedosov et al. [134] (Figure 4.9C). Authors show that flipping motion is typical of iRBC and it is strictly related to Young's modulus of the membrane which is larger than hRBC.

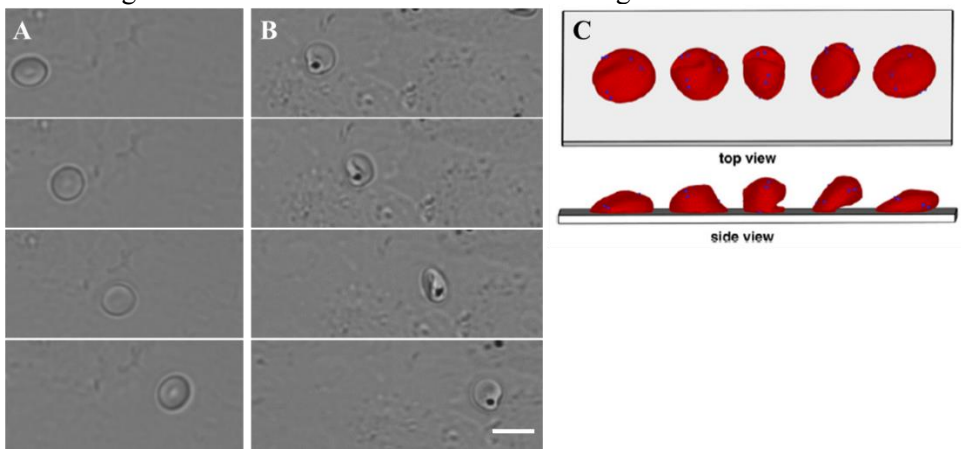

Figure 4.9 - (A) Sequence of snapshot of a hRBC (A) and an iRBC (B) flowing on endothelial cells. (C) Simulation of the phenomenon [134]. Scale bar 10 µm

It should be emphasized that dynamics of iRBC depends on the stage of parasite development; later stages (e.g. trophozoite and schizont) are characterized by a fivefold

increase in the membrane Young's modulus compared with that of hRBC. Unfortunately, iRBC in such stages have not been identified in this work.

Finally, adhesion of RBC on endothelial cells treated with neuraminidase were evaluated. RBC suspension has flowed on HUVEC for 1 hour at 0.33 Pa. Then, a washing step was applied to remove unattached RBC (1.5 ml/min for several minutes) by using fresh culture medium. Figure 4.10A and Figure 4.10B show images acquired after channel washing. The most important observation is the presence of both iRBC and hRBC adherent on HUVEC as clearly visible in the zoomed images. A quantification of attached RBC have been carried out and reported in the histogram of Figure 4.10C; the adhesion has been expressed as the number of adherent RBC/mm^2 for two wall shear stresses. The result shows that there is no difference between infected and healthy cells which is quite anomalous because hRBC should not interact with endothelial cells or at least the difference should be marked. It is interesting to observe the presence of haemozoin on the endothelial cells underlined by red circles in Figure 4.10D. Haemozoin is a crystalline pigment produced by the digestive vacuole of *Plasmodium* parasite as a product of haemoglobin catabolism [177]. It is well known that haemozoin is involved in several aspects of the pathology of the malaria in particular during inflammatory response in the acute phase [178].

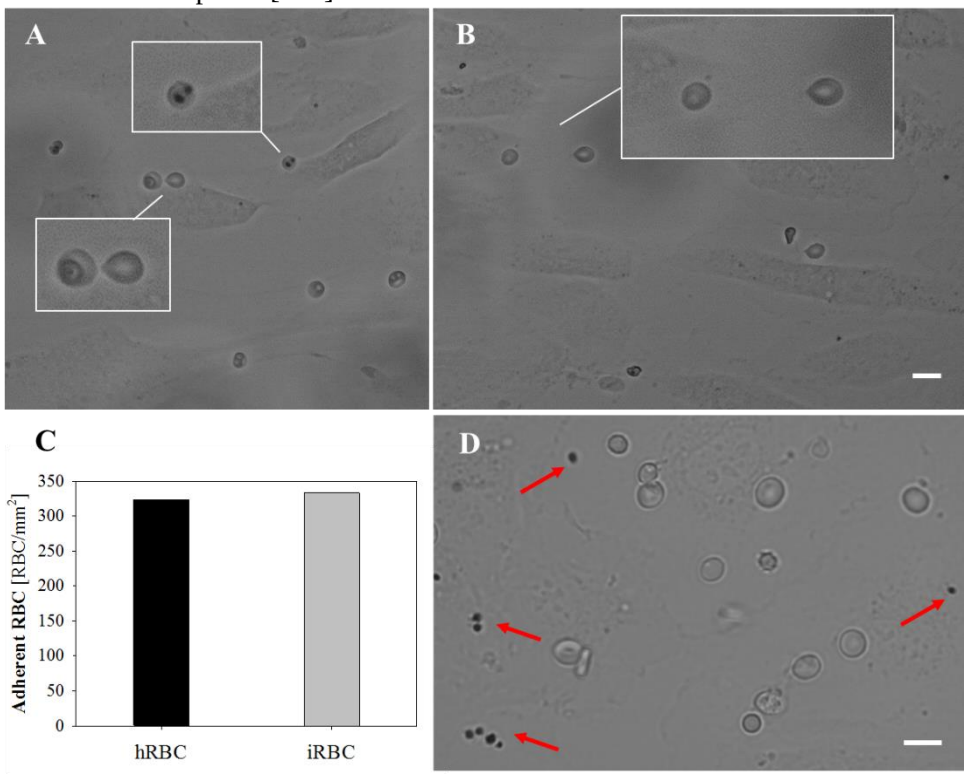

Figure 4.10 - Images of iRBC (A) and hRBC (B) attached on HUVEC. (C) Histogram of attached RBC. (D) Hemozoin residues on endothelial cells. Scale bar 10 µm

The adhesion of iRBC to endothelial cells is a well-known phenomenon that is described in the literature even though the mechanisms are still unclear. On the other

hand, the behavior of hRBC was not expected. Figure 4.11 reports the number of adherent RBC (both iRBC and hRBC) at two wall shear stress on a HUVEC monolayer with and without (i.e. control) enzyme treatment. No difference can be noticed between the number of adherent RBC with and without enzyme treatment. The adhesion of both RBC species in the control case could be explained considering the role of the extracellular methemoglobin. In fact, during malaria culture *in vitro*, parasite releases toxic products that develop a pro-coagulant microenvironment. RBC lysis releases haemoglobin that is oxidized to form methemoglobin. The latter promotes the adhesion of RBC (both infected and healthy) to endothelial cells due to the production of inflammatory markers and cellular adhesion molecules [179, 180]. Balaji and Trivedi [181] demonstrated that methemoglobin induce oxidative stress within RBC caused by the production of free radicals. As consequence phosphatidyl serine externalization occurs generating sticky patches on RBC that induce adhesion to endothelium. Regarding the case without the SA, recently Oberleithner et al. [182] demonstrated that sodium renders endothelial cells sticky for hRBC by shielding selectively the negative charge of the endothelial GCX. One can speculate that in our experiments neuraminidase performs the same action of the sodium and hence no difference can be appreciable between healthy and infected as reported in Figure 4.10C.

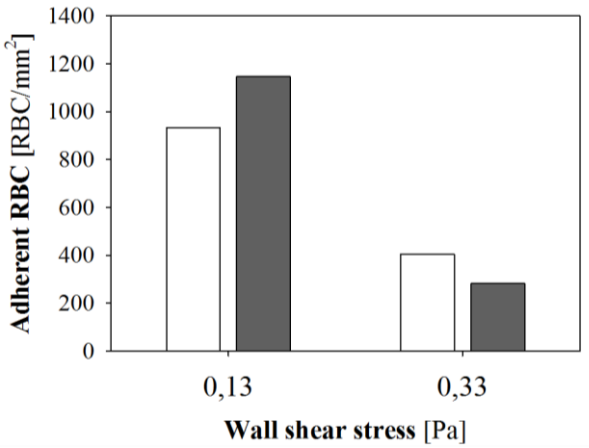

Figure 4.11 - Histogram of attached RBC (both hRBC and iRBC) for two wall shear stresses. White bars HUVEC without enzyme treatment, dark grey with enzyme treatment

4.5 Summary

To our knowledge, the measurements and results described in this chapter are one of the first attempts to study the flow behavior of human blood in the presence of endothelial cells.

Microchannels have been lined with human endothelial cells as described in chapter 3 and then velocity profiles of RBC suspensions have been evaluated along the channel height and channel width. In the former case, a typical flat parabolic profile has been reported. Plateau velocity of endothelialized channels has been found less than bare ones (from 5.9% to 34%). In order to explain the origin of this result, the resistance to flow has been estimated for both channels. The resistance to flow is about 5% higher in

endothelialized channel compared to the bare ones. Such value is slightly lower than the velocity difference leading to the conclusion that the interaction among HUVEC and RBC is not due to purely fluid dynamic reasons. Maybe, biochemical factors could regulate the flow behavior of RBC in such channels. Therefore, the contribution of the electronegativity of endothelial GCX has been investigated. Results show that GCX charge does not influence the velocity of RBC. Regarding the general trend of the velocity profiles along the channel height, no appreciable differences between bare and endothelialized channel have been found for all shear stress investigated. It should be emphasized that velocity profiles were acquired in different experimental conditions i.e. different experimental apparatus. In Figure 4.12, velocities obtained with the two apparatus are plotted as function of the wall shear rates. The reliability is confirmed by the collapse of all data on a single straight line.

Finally, preliminary results on the interaction between *Plasmodium falciparum* iRBC and endothelial cells have been evaluated. Cytoadherence of iRBC to endothelial cells is an important issue related to the severity of disease. In particular, the possible role of GCX has been investigated reducing its negative charge via enzymatic treatment (i.e. cleavage of SA). Velocity values show that there is no difference between HUVEC with and without SA. Focusing on a single RBC, it has been shown that both hRBC and iRBC tend to adhere to HUVEC even though in a different manner. hRBC slip on the HUVEC monolayer via tank-treading of the membrane whereas iRBC flip on the monolayer in agreement with Fedosov et al. [134]. While it is well known that iRBC stick on endothelial cells, adherence of hRBC is not expected. The reason could be related to the iRBC culture *in vitro*; in fact malaria parasite releases haemoglobin which is converted into methemoglobin. The latter renders hRBC in the culture sticky for endothelial cells due to the externalization of phosphatidyl serine that generates sticky patches. Quantifying the number of RBC attached on the HUVEC, it has been demonstrated that there is no difference between hRBC and iRBC.

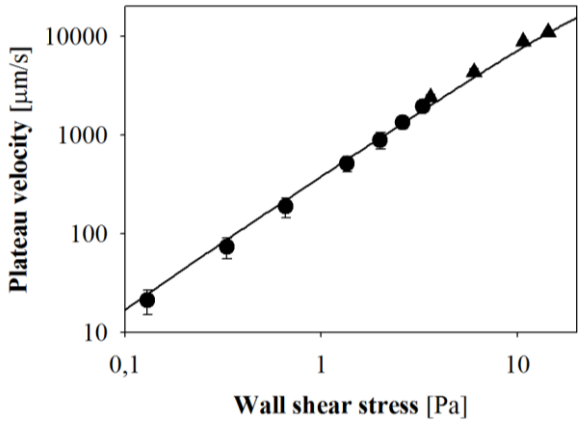

Figure 4.12 – Plateau velocity as function of wall shear stress. Circles and triangles refer to two different apparatus

5. Conclusions

During this PhD thesis, human blood flow properties have been investigated from both hemorheological and hemodynamic points of view. The unique composition of human blood leads to a very uncommon behavior under flow.

A deep rheological investigation under both steady and oscillatory regimes has been performed. The flow curves of blood are consistent with available experimental data, while the oscillatory experiments provide a rigorous viscoelastic characterization in the linear viscoelastic regime. The viscous response prevails on the elastic term over the entire test range of frequencies tested although the elastic contribution is considerable. In order to explain these results, the plasma release cell-layering theory can be applied [56]. The oscillatory deformation induces RBC become arranged in 2D structures flowing in layers separated by the suspending medium, which acts as a lubricant in between. Indeed, the source of blood linear viscoelasticity is still to be fully understood; in fact other authors believe that viscoelasticity arises from RBC membrane rheological properties [160], which is known to exhibit a viscoelastic behavior [161, 162]. In addition the effects of RBC volume fraction and of the addition of dextran have been also investigated. Such samples had the purpose to simulate situation of clinical interest such as polycythemia (Htc up to 60%), blood bags used for transfusion (Htc higher than 90%), and altered aggregation properties. In particular Htc values has been varied from 8% up to 99%, a range never reported before. Results have shown an evolution to a gel-like behavior increasing both Htc and aggregating agent. More work is still needed to fully elucidate rheological behavior of human blood and the related problem of the clinical significance of blood linear viscoelasticity. In fact. several clinical investigations highlight the correlation between alterations of hemorheological parameters and the incidence of diseases affecting the cardiovascular system [183]. It was demonstrated that impaired blood flow represents a risk factor of thrombosis and atherosclerosis [184] in pathologies such as myocardial infarction [185], hypertension [186], and diabetes [187].

The investigation of the flow properties of human RBC in a more physiological *in vitro* model is carried out. To this aim, methods and experimental protocols for the endothelialisation of microchannels have been developed by using human endothelial cells. A home-made perfusion system has been set up in order to recreate a physiological environment into the microchannel, i.e. a continuous unidirectional flow. Thus, alignment and elongation of endothelial cells in the direction of flow have been obtained as well as occurs in human vessels. By acquiring images of the cells every day, orientation angles and shape index have been calculated. Already after 24h, endothelial cells have exhibited an orientation along the flow direction while the elongation becomes appreciable only after 8 days. Labelling of the GCX with specific molecules (i.e. WGA-Alexa 488) has been also done in order to evaluate the presence and the expression of the GCX. It has been reported that cells under flow are thinner compared to cells without

shear stimulation. Moreover, enzymatic digestion of the GCX component that gives the negative charge (i.e. SA) has been evaluated by monitoring the mean fluorescence intensity before and after treatment.

All the results related to the endothelial cell characterization have been useful for the subsequent perfusion of endothelialized channel with RBC. Microchannels dimensions and flow conditions are chosen to mimic the vascular region of big arterioles and venules. Velocity profiles of RBC suspensions have been evaluated. A typical flat parabolic profile has been reported along the channel width. Comparing bare and endothelialized channels, plateau velocity has resulted higher in channel without cells (from 5.9% to 34%). In order to understand this finding, the resistance to flow has been estimated for both channels. It has found that the resistance to flow is about 5% higher in endothelialized channels than the bare ones which is a value slightly lower than the velocity difference. Therefore, one can speculate that the endothelial monolayer does not merely induce a simple reduction of the vessel lumen but it is also able to regulate RBC flow through biochemical factors. Regarding the trend along channel height, a parabolic profile has been found in both cases even though no significant differences have been noticed.

The mentioned approach has been used to investigate flow properties of malaria infected RBC by *Plasmodium falciparum* parasite. It is well known that malaria disease may evolve into severe malaria when infected RBC evade the splenic filter thanks to their ability to adhere to the endothelium. Images of single infected and healthy RBC flowing on endothelial cells have been acquired showing a different dynamic behavior. Healthy RBC slide on the endothelial cells by rearranging their membrane in the typical tank-treading motion; on the other hand infected RBC flip continuously. These results are in good agreement with previous numerical simulation work [134] in which it was found that the main parameter governing the dynamic are the RBC membrane stiffness. The possible role of endothelial GCX in the adhesion process of infected RBC have been evaluated. Removing the GCX an unexpected result has been observed that is no difference has been found in the number of infected and healthy RBC attached on endothelial monolayer. This findings can be explained considering the work of Oberleithner et al. [182]. They demonstrated that sodium renders endothelial cells sticky for healthy RBC by shielding selectively the negative charge of the endothelial GCX. One can speculate that in our experiments neuraminidase performs the same action of the sodium and hence no difference can be appreciable between healthy and infected.
It was obvious then do an experiment without enzyme treatment. Again, no difference was found. To explain this controversial result, it is appropriate to consider the role of the extracellular methemoglobin. During malaria culture *in vitro*, parasite releases toxic products that develop a pro-coagulant microenvironment. The process starts with RBC lysis that releases haemoglobin. The latter is oxidized to form methemoglobin that promotes the production of inflammatory markers and cellular adhesion molecules on RBC (both healthy and infected) to endothelial cells [179, 180]. Balaji and Trivedi [181] demonstrated that methemoglobin induce oxidative stress within RBC caused by the production of free radicals. As consequence phosphatidyl serine externalization occurs generating sticky patches on RBC that induce adhesion to endothelium.

As a concluding remark, this study presents new insights about some issues related to blood rheology and haemodynamics. More work is still needed to fully elucidate the source of blood viscoelasticity and its significance in the clinical applications. Moreover, flow assay that mimics blood flow in human vessels could help the development of new microfluidic platform for drug testing.

5.1 Future work

The obtained results could helpful to understand the behavior of RBC under flow. The source of blood linear viscoelasticity is still to be fully understood. Results obtained in the rheological campaign could be compared with other rheological techniques able to characterize or visualize blood structure at microscale level.

By using the protocols developed in the second part of the work, it would be interesting to investigate the interaction among RBC and endothelium in microchannel reproducing capillary or post-capillary regions, i.e. reducing channel dimensions. This simple and realistic experimental model could be used to explore a variety of questions about how blood cells interact with endothelial layer in the microcirculation region where other interesting phenomena occurs such as extravasation of drug carriers. Moreover, the preliminary results on malaria infected RBC are very interesting and require a deeper comprehension of the obtained results. For example, further investigation could be addressed to understand the flow behavior of infected RBC on brain vascular cells, reduce microchannel dimensions, and increases parasitemia levels. In general, the proposed endothelialisation protocols could be used for the development of lab-on-chip devices in the biomedical field.

Appendix A - Development of oligonucleotides-functionalized surfaces for fluorescence-based biosensing applications

In the last century, technological improvement in the field of life science has led to reach exceptional goals. One of the main breakthroughs is represented by biochips, small, microelectronics-inspired devices that are used for delivery, processing, analysis or detection of biological molecules and species. Biochips are able to manage extremely small amounts of sample (few microliters or less), processing it in an adequate manner to provide analytical results. These devices are manufactured from substrates such as silicon, fused quartz, glass, and plastic, manipulated with various techniques ranging from micromilling to lithography. Due to their small size, biochips presents several advantages over bench-scale methods: they are amenable for point-of-care diagnostics, using small amount of reagents, producing less waste, and reducing the time and the costs of the analysis.

Here, a part of a project aimed to develop a biochip for diagnostic applications is reported. In particular, the final device should be able to process a whole blood sample, extracting the nucleic acid content from white blood cells and detecting a specific mRNA sequence, providing the result in a digital form. The aim of this work is to provide a conceptual design of the device and to characterize the detection step, which is identified as limiting. Nucleic acid hybridization matched with confocal fluorescence microscopy imaging has been chosen as detection technique.

A.1 Background

Nucleic acid hybridization is the main technique used to detect nucleic acid sequences of interest. Hybridization event can be highlighted by several methods, such as mechanical methods (e.g. microcantilever), electrical methods (conductometric, amperometric, and potentiometric detection, etc.), and optical methods (fluorescence, interferometry, etc.). The latter ones are the most common due to their prevalent use in biology and life sciences. Hybridization is the process of establishing a non-covalent, sequence-specific interaction between two or more nucleic acids complementary strands into a single complex, named duplex. This process can involve DNA, RNA, or oligonucleotides (oligos). Hybridization of nucleic acids represents a fundamental tool for molecular genetics studies, and can be performed in several ways, having a common functioning principle: a characterized population of single stranded molecules is used to screen between a complex mixture of nucleic acids in a sample of medical or biological interest. In hybridization experiments, the characterized population of single stranded molecules acts as a "probe"; probes are used to scan the sample in order to find complementary molecules, named "targets". For this purpose, the probes and the targets can be mixed, allowing their annealing in liquid or solid phase.

It is important to consider that both DNA and RNA needs to be denatured to perform the hybridization reaction. Denaturation can be achieved by heat treatment or by the exposition to alkaline or highly polar conditions, e.g. using urea or formamide solutions.

Hybridization between probes and targets is affected by several variables. Stability of the DNA double helix depends on a fine balance of interactions including hydrogen bonds between bases and surrounding water molecules, and base-stacking interactions between adjacent bases. In a hybridization experiment, to obtain a good detection signal, stable formation of target-probe hybrids should be favored. On the other hand, a specific signal is needed, therefore non-specific interaction should be disrupted. Variables which are able to affect the hybridization reaction are temperature, probe design, environmental effects, and concentration [188]. These conditions must be highly controlled in order to screen between thousands of molecules and detect only the population of molecules of interest. Usually, the hybridization rate in liquid phase is better than solid phase. Moreover, solid phase hybridization allows to easily perform the washing steps required to obtain a specific signal. For this reasons, probes bonded to a solid support are preferred [189]. Generally, the support can be a plastic membrane, a glass slide, or a quartz chip. Commonly used methods for immobilizing DNA or oligonucleotides to solid surfaces are adsorption, covalent attachment, and *in situ* synthesis of oligos.

A.2 Materials and methods

Functionalized glass slides

For the covalent immobilization of probes on solid support, we used functionalized glass slides (PolyAn GmbH, Germany). The slides are produced with standard dimension of 25 x 75 x 1.0 mm: functionality as well as contact angle of the surface is routinely tested before shipment. For the experiments, three different types of slides having 2-dimensional (2D) and 3-dimensional (3D) functionalization are chosen.

2D-reactive glass slides are tailored for cost-effective applications and manufactured from high quality glass with an ultra-flat surface and low inherent fluorescence. The glass is coated with a thin silane layer that will covalently bind most types of bio-molecules. The defect-free surface features uniform silane layers that provide a high covalent coupling efficiency together with a very low background fluorescence. Two types of 2D slides are tested:

- 2D-Amino slides: the oligo is bound electrostatically with its 5'-phosphate group (or with another phosphate group added with an appropriate chemistry). An UV-crosslinking step is required to attach the nucleic acid covalently on the surface;
- 2D-Epoxy slides: the surface reacts immediately with a nucleophilic group, such as an amino-group linked to the oligo in a standard S_N2 reaction, forming a covalent bond.

3D glass slides are functionalized with a surface chemistry comprised of a long-chain polymer containing a defined number of reactive groups. This polymer is covalently linked to the surface of the slide without damaging the base substrate. The morphology of the functional surface and thus also the number of the reactive groups are fine-tuned within a narrow range. The principle of immobilization is the same than that of the 2D-Epoxy slides.

Probes oligonucleotides

Probe oligonucleotides were modified both in 3' and 5' termini. On 5' terminus, phosphate and amino linkers were used to allow the binding on Amino and Epoxy surfaces, respectively. On 3' terminus, Cy®3 fluorophore was added to detect the immobilized probes. It was also used two different types of spacer, named C-3 and C-12. Probe oligonucleotides were 25 bases in length. Figure A.2.1 shows a generic probe oligonucleotide while Table A.2.1 summarizes all the probes combinations of functionalization, spacers, and sequences tested.

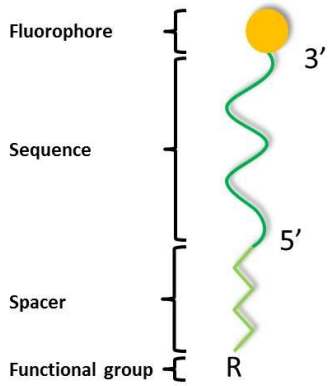

Figure A.2.1 – Generic probe oligo

5'	SPACER	SEQUENCE	3'
R-OPO_3^{2-}	C-3	A	Cy®3
R-OPO_3^{2-}	C-12	A	Cy®3
R-NH_2	C-3	A	Cy®3
R-NH_2	C-12	A	Cy®3
R-OPO_3^{2-}	C-3	A	OH
R-OPO_3^{2-}	C-12	A	OH

Table A.2.1 – Oligos tested as a probe in immobilization experiments

The sensitivity of DNA chips is clearly dependent on the efficiency of hybridization at the surface that can be improved by introducing spacer chains to attach the terminus of the probe to the grafting site. These create distance between the probes and the impenetrable surface, enhancing the hybridization process [190]. On the basis of literature study, spacers C-3 and C-12 are chosen, which differs in the number of carbon of the chain (respectively 3 and 12).

Target oligonucleotides

Target oligonucleotides were 25 bases in length and modified in their 5' terminus with 6-FAM fluorophore (6-Carboxyfluorescein). Table A.2.2 shows the target oligos tested.

5'	SEQUENCE	3'
6-FAM	A complementary	OH

Table A.2.2 – Oligos tested as target in immobilization experiments

Immobilization protocols

Immobilization protocol was slightly different for 2D-Amino and 2D or 3D-Epoxy supports. The protocol was developed on the basis of an extensive literature [191-194]. All the reagents were purchased from Sigma-Aldrich, functionalized slides were purchased from PolyAn GmbH, and oligos were provided by the group of Prof.ssa Pasqualina Buono of University of Naples Parthenope.

Immobilization on 2D-Amino slides

Probes were diluted in 100 mM, pH 8.5, Na_2CO_3/$NaHCO_3$ buffer at 0.5 and 5 µM concentrations. Diluted oligonucleotides was denatured at 100°C for 10 minutes and then immediately spotted on 8-wells 2D-Amino slides in a chamber with 70% relative humidity for 1h. Slides were dried on a hot stage at 80 °C and then exposed to UV at λ = 365 nm for 3 minutes using an UV lamp. Subsequently, slides were immersed for 2 h in a passivation solution composed by 4% acetic anhydride in dicloroethane (the reaction with an anhydride changes the surface charge from + to – and repulse any negatively charged DNA target). After incubation, slides were washed with acetone, with 100mM Tris HCl, 600mM NaCl, pH=7,5, 3 times with distilled water, then with SSC 1X + 0.2% (w/v) SDS, SSC 0.1X + 0.2% (w/v) SDS, SSC 0.1X, 2 times with distilled water and dried with compressed air. All the washes were conducted in agitation in a large volume (50 ml) of washing solution. As a control, wells treated with the same protocol except for the absence of the probes in spotting solution, were processed.

Immobilization on Epoxy slides

Immobilization protocol on Epoxy surface was the same for both 2D and 3D slides. Probes were diluted in 100 mM, pH 8.5, Na_2CO_3/$NaHCO_3$ buffer at 1 and 10 µM concentrations. Probes were denatured at 100°C for 10 minutes and then immediately spotted on 8-wells 2D and 3D-Epoxy slides in a chamber with 70% relative humidity. The incubation time was overnight. Then, the slides were dried with compressed air and immersed a passivation solution composed by 100 mM Tris-HCl + 50 mM ethanolamine at pH 9.0 for 2 hours (ethanolamine is a primary amine which reacts with the Epoxy surface in a standard S_N2 reaction, saturating the binding sites). Slides were washed 2 times with distilled water, then with SSC 4X, SSC 2X + 0.1% (w/v) SDS, SSC 0.2X, SSC 0,1X, 2 times with distilled water and dried with compressed air. All the washes were conducted in agitation in a large volume (50 ml) of washing solution. As a control, wells treated with the same protocol except for the absence of the probes in spotting solution, were processed.

Hybridization protocol

The supports were denatured in boiling water for 3 minutes, then passed in ice-cold ethanol and dried with compressed air. Subsequently, slides were incubated for 1 h at 42 °C with a pre-hybridization buffer composed by 2x SSC, 0.1% (w/v) SDS, 1% (w/v) BSA, 50% (v/v) formamide, and 0.01% (w/v) Salmon Sperm DNA, then washed with distilled water and dried with compressed air. Targets were diluted in a hybridization buffer composed by 5X SSC, 0.1% (w/v) SDS, 10% (w/v) dextran sulfate and 25% (v/v) formamide. Diluted samples were denatured at 100°C for 10 minutes and then immediately spotted on slides with a spotting volume of 2µL in a chamber at 42°C and

100% relative humidity. Incubation was overnight. Subsequently, slides were washed with SSC 2X + 0.1% (w/v) SDS, SSC 1X, SSC 0.2X, and finally with distilled water. All washes were conducted with a large volume of washing solution (50 ml) in agitation for 10 minutes. After washing, the slides were dried with compressed air. As a control, wells treated with the same protocol, except for the absence of targets in hybridization solution, were processed.

A.3 Results

Immobilization

Three immobilization protocols were developed (for the sake of brevity just the last one is reported). Figure A.2.2a shows a typical functionalized slide before starting immobilization protocol with 40 spots, each one containing oligo probes. Figure A.2.2b shows a spot on a 2D-Epoxy slide after immobilization. The image was acquired with 5X objective, which yields a field of view of ~3.37 mm^2, whereas the area of each spot is ~1.43 mm^2. A high fluorescent signal and a uniform black background are observed.

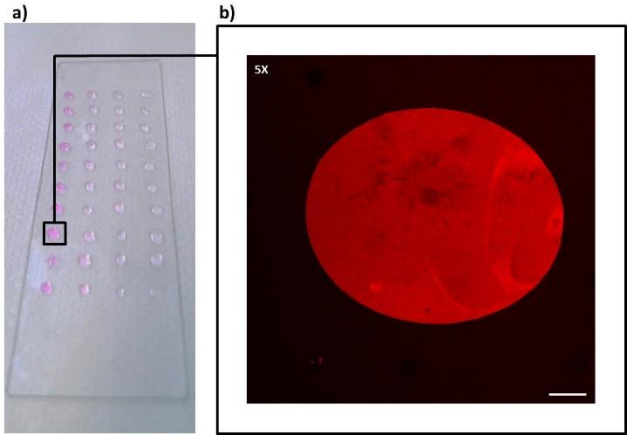

Figure A.2.2 – a) Image of a slide before immobilization protocol starting; b) Immobilization spot obtained on a 2D-Epoxy support. Image is acquired with 5X objective. Scale bar = 200 μm

To identify the best immobilization density for hybridization experiments, calibration curves were built for all the supports in a wide range of spotting solution concentrations (0.05, 0.1, 0.5, 1, 5, 10, 50, and 100 μM) immobilizing C-12 spacer oligos. In these experiments, pipetting volume was 0.4 μL. Images were acquired using different Gain parameters due to the wide range of concentrations investigated, i.e. to retain the fluorescence intensity curve between optimal values: in this way, image saturation is avoided. The correlation between Gain and the Mean Fluorescent Intensity (MFI) is verified for 3 of the 8 concentrations tested in calibration curve experiments (0.05 μM, 1 μM, 100 μM), resulting in a linear function as shown in Figure A.3.1.

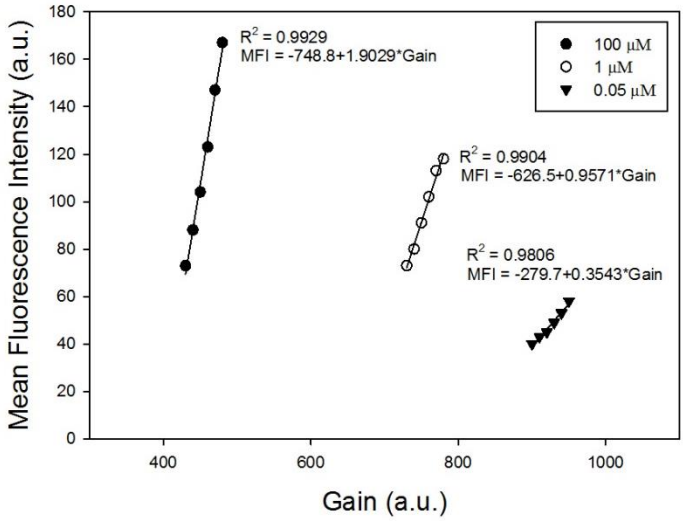

Figure A.3.1 - Plot showing linearity between Gain and MFI at three different concentrations

This linear correlation allows to acquire the images at different Gain values, normalizing the fluorescence intensities. Normalized Fluorescence Intensity was calculated as:

$$NFI = \frac{MFI}{GAIN_{ACQ}} - \frac{CFI}{GAIN_{ACQ}}$$

where CFI is Control Fluorescence Intensity (which corresponds to the MFI value of a control spot without oligos) and $GAIN_{ACQ}$ is the value of the gain parameter in microscope acquisition software. Figure A.3.2 shows a summary of calibration curves obtained on all supports spotting various probe concentrations (ranging from 0.05 to 100 μM). The plot is shown on a log-log scale fitted with a power function. The C exponent of the log-log scale represents the slope of the curve. Points relative to 0.05 and 0.1 μM were omitted because they were indistinguishable from the background.

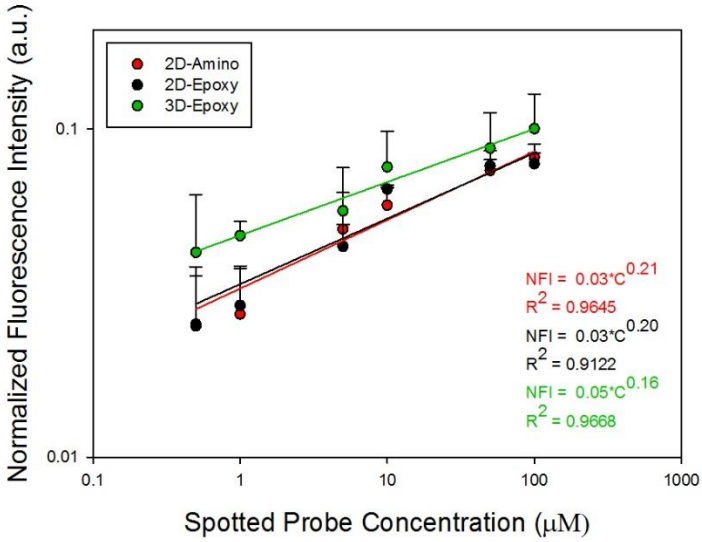

Figure A.3.2 - Summary of calibration curves obtained on all the supports. Data were obtained from three sets of experiments

Hybridization

Hybridization experiments were performed using complementary 25mer oligos functionalized on their 5' terminus with 6-Fluorescein amidite (6-FAM) fluorophore as target. As probe, blank oligos (without fluorophores), functionalized on 5' terminus with functional groups chosen on the basis of the support was used. This choice is due to avoid the overlap between Cy®3 and 6-FAM fluorophores emission signals. In fact, exciting sample with 488 nm light, absorption and emission are possible not only by 6-FAM but also by Cy®3 fluorophore, resulting in a signal overlap that could weaken, or, in low target concentration condition, even completely mask hybridization signal. Immobilization of blank probes could not be detected using direct observation in fluorescence microscopy. However, this evaluation can be indirectly obtained performing a simple hybridization experiment. In this experiment, two kinds of controls were established to ensure the immobilization of blank probes. Firstly, slides were spotted with blank and labeled probes in different positions on the same support (Figure A.3.3, left). Detection of labeled probes is indicative of the success of immobilization. Then, the surface is bathed with a hybridization solution containing the targets at 1 μM concentration. In the case of successfully immobilized and functional blank probes, the presence of green spots in correspondence of the spotted blank probe positions is expected. Figure A.3.3 (right) shows results of this experiment on a 2D-Amino support. As expected, blank spots became detectable after hybridization, due to 6-FAM modification of targets. This experiment has been successful on all the supports, confirming the functionality of surfaces and immobilization reproducibility between blank and Cy®3-modified probes. Images of other supports are not shown for the sake of brevity.

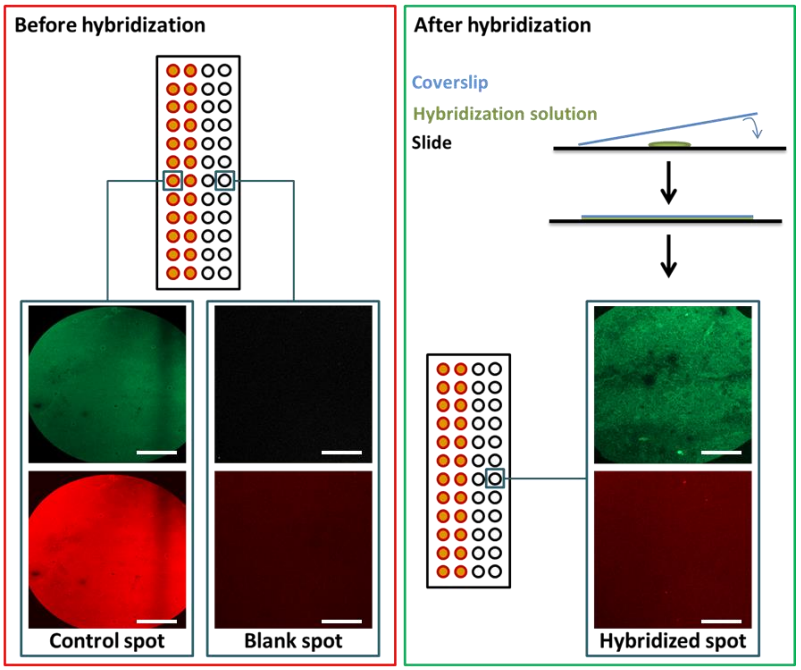

Figure A.3.3 - Images relative to a 2D-Amino support. (Left) Schematics of immobilization experiment and images of a fluorescent probe spot and a blank probe spot are shown. (Right) Schematics of the hybridization experiment and an image showing a blank hybridized spot. Same acquisition parameters compared to left blank spot image. Images acquired with 10X objective using 488 nm and 543 nm excitation laser for 6-FAM and Cy®3 respectively. Scale bars = 200 μm

To identify the best immobilization density for target capture, hybridization experiments were conducted spotting a fixed target concentration (20 μM) on different density probe spots, ranging from 0.5 to 100 μM immobilization spotting concentrations. Spot position reproducibility between immobilization and hybridization phases was obtained using a home-made alignment system. NFI was calculated as previous experiments. Even functionality of surfaces was confirmed for all the supports, hybridization experiments was not reproducible on 2D-Amino supports. For this reason, the data on these supports are not reported in the next plot. Figure A.3.4 shows hybridization curves obtained on oligo-functionalized 2D and 3D-Epoxy surfaces. As in the case of the immobilization curves, hybridization data can be fitted with a logarithmic function. However, plot was showed on log-log scale and fitted with a power function.

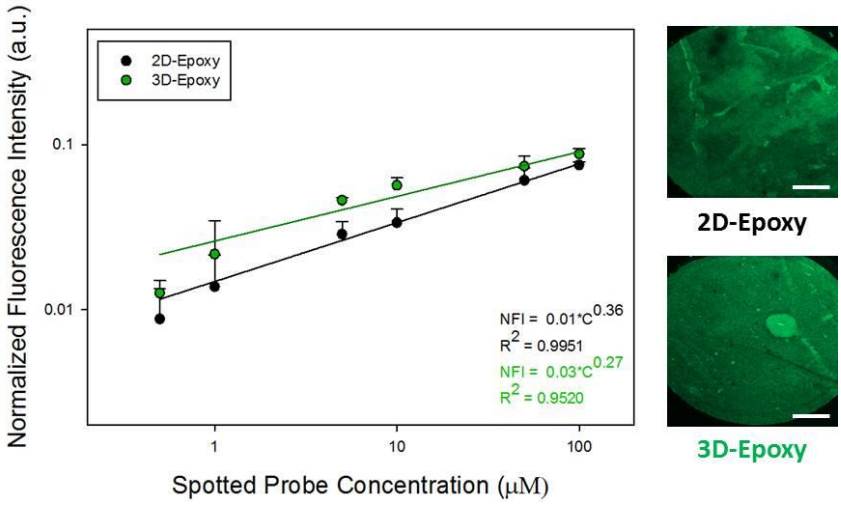

Figure A.3.4 - Hybridization curves obtained spotting a hybridization solution containing the targets at 20 μM concentration on oligo functionalized 2D and 3D-Epoxy surfaces. Data were fitted with a power function where C is the spotted probe concentration. Data were obtained from three sets of experiments. On the right, two hybridization images, acquired with 10X objective on 2D and 3D-Epoxy surfaces, are shown. Scale bars = 200 μm

A.4 Results

This work is part of a project aimed to develop a biochip for diagnostic applications. It is worth underlining that the results reported in this appendix aim to estimate the limit of detection of the final device. Thus, a short discussion on conceptual design of the biochip is provided.

Figure A.4.1 shows a comparison between immobilization and hybridization curves compared to a literature study [195]. Comparing these curves, it is not possible to perform quantitative considerations, both in immobilization-hybridization comparison and in our experiments-literature comparison. This is due to relativity of units on the y-axis (i.e. NFI), and different fluorophores and equipment used. However, it is possible to compare trends of data and to perform semi-quantitative observations. Interpretation of this plot leads to two conclusions:

- Our data are comparable with literature data; slope of the curves is different, however both immobilization and hybridization experiments show a linear dependence when fitted on a log-log plot. This trend is probably due to progressive saturation of binding sites and mass transport limitations of the system; moreover, repulsive interactions between the considered molecules, that are negative-charged, could play a role in the observed behavior;
- Regarding our results, no saturation was observed, both in immobilization and hybridization experiments. In the case of immobilization experiments, saturation could be possible spotting probe concentrations higher than 100 μM. This aspect was outside the aim of the present work, and was not investigated also due to the limited amount of materials available. In the case of hybridization experiments, the

fact that saturation is not observed leads to the conclusion that even in higher density of probes condition, steric hindrance, which could lead to hybridization inefficiency, was not observed.

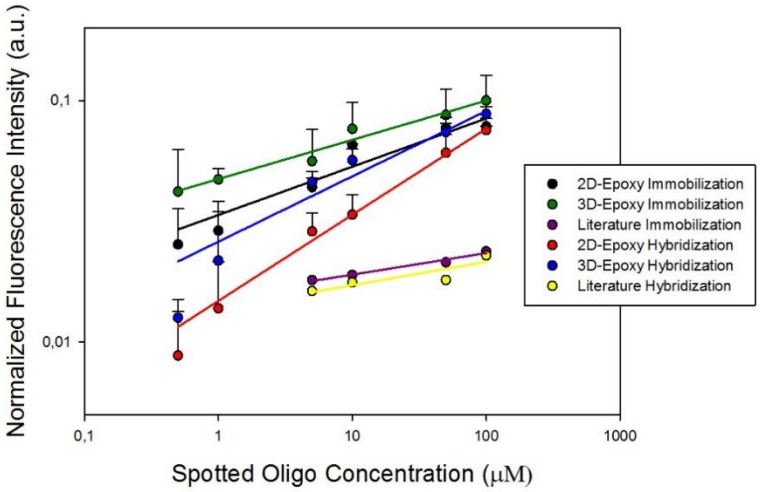

Figure A.4.1 – Comparison between immobilization and hybridization experiments on 2D and 3D-Epoxy slides compared with a literature study [195]

References

[1] R. Hoffman, L.E. Silberstein, H. Heslop and J. Weitz, *Hematology: basic principles and practice*, Elsevier Health Sciences, 2013.

[2] O.K. Baskurt and H.J. Meiselman, Blood rheology and haemodynamics, in: *Seminars in thrombosis and hemostasis*Vol. 29, New York: Stratton Intercontinental Medical Book Corporation, c1974-, 2003, pp. 435-450.

[3] A. Daly, J.S. Raval, J.H. Waters, M.H. Yazer and M.V. Kameneva, Effect of blood bank storage on the rheological properties of male and female donor red blood cells, *Clinical hemorheology and microcirculation*, **56** (2014), 337-345.

[4] Y. Zheng, J. Chen, T. Cui, N. Shehata, C. Wang and Y. Sun, Characterization of red blood cell deformability change during blood storage, *Lab on a Chip*, **14** (2014), 577-583.

[5] V. Deplano, Y. Knapp, L. Bailly and E. Bertrand, Flow of a blood analogue fluid in a compliant abdominal aortic aneurysm model: experimental modelling, *Journal of biomechanics*, **47** (2014), 1262-1269.

[6] S. Bose, R. Singh, M. Hanewich-Hollatz, C. Shen, C.-H. Lee, D.M. Dorfman, J.M. Karp and R. Karnik, Affinity flow fractionation of cells via transient interactions with asymmetric molecular patterns, *Scientific reports*, **3** (2013).

[7] E.W. Merrill, Rheology of blood, *Physiol. Rev*, **49** (1969), 863-888.

[8] G.R. Cokelet, Rheology and haemodynamics, *Annual Review of Physiology*, **42** (1980), 311-322.

[9] G. Tomaiuolo, A. Carciati, S. Caserta and S. Guido, Blood linear viscoelasticity by small amplitude oscillatory flow, *Rheologica Acta* (2015), 1-11.

[10] M. Brust, C. Schaefer, R. Doerr, L. Pan, M. Garcia, P. Arratia and C. Wagner, Rheology of human blood plasma: Viscoelastic versus Newtonian behavior, *Physical review letters*, **110** (2013), 078305.

[11] O.K. Baskurt, *Handbook of hemorheology and haemodynamics*, IOS press, 2007.

[12] Y.-c. Fung, *Biomechanics: mechanical properties of living tissues*, Springer Science & Business Media, 2013.

[13] S. Chien and K.-m. Jan, Ultrastructural basis of the mechanism of rouleaux formation, *Microvascular Research*, **5** (1973), 155-166.

[14] O. Baskurt, B. Neu and H.J. Meiselman, *Red blood cell aggregation*, CRC Press, 2011.

[15] M. Rampling and J.A. Sirs, The interactions of fibrinogen and dextrans with erythrocytes, *The Journal of physiology*, **223** (1972), 199.

[16] N. Maeda and T. Shiga, Inhibition and acceleration of erythrocyte aggregation induced by small macromolecules, *Biochimica et Biophysica Acta (BBA)-General Subjects*, **843** (1985), 128-136.

[17] C. Lacombe, C. Bucherer, J. Ladjouzi and J. Lelievre, Competitive role between fibrinogen and albumin on thixotropy of red cell suspensions, *Biorheology*, **25** (1987), 349-354.
[18] R. Ben-Ami, G. Barshtein, T. Mardi, V. Deutch, O. Elkayam, S. Yedgar and S. Berliner, A synergistic effect of albumin and fibrinogen on immunoglobulin-induced red blood cell aggregation, *American Journal of Physiology-Heart and Circulatory Physiology*, **285** (2003), H2663-H2669.
[19] K. Lee, M. Kinnunen, M.D. Khokhlova, E.V. Lyubin, A.V. Priezzhev, I. Meglinski and A.A. Fedyanin, Optical tweezers study of red blood cell aggregation and disaggregation in plasma and protein solutions, *Journal of biomedical optics*, **21** (2016), 035001-035001.
[20] H. Meiselman, B. Neu, M. Rampling and O. Baskurt, RBC aggregation: laboratory data and models, *Indian journal of experimental biology*, **45** (2007), 9.
[21] J. Armstrong, R. Wenby, H. Meiselman and T. Fisher, The hydrodynamic radii of macromolecules and their effect on red blood cell aggregation, *Biophysical journal*, **87** (2004), 4259-4270.
[22] S. Chien, Biophysical behavior of red cells in suspensions, *The red blood cell*, **2** (1975), 1031-1133.
[23] P. Steffen, C. Verdier and C. Wagner, Quantification of depletion-induced adhesion of red blood cells, *Physical review letters*, **110** (2013), 018102.
[24] H. Bäumler, B. Neu, E. Donath and H. Kiesewetter, Basic phenomena of red blood cell rouleaux formation, *Biorheology*, **36** (1999), 439-442.
[25] M. Brust, O. Aouane, M. Thiébaud, D. Flormann, C. Verdier, L. Kaestner, M. Laschke, H. Selmi, A. Benyoussef and T. Podgorski, The plasma protein fibrinogen stabilizes clusters of red blood cells in microcapillary flows, *Scientific reports*, **4** (2014).
[26] S. Asakura and F. Oosawa, On interaction between two bodies immersed in a solution of macromolecules, *The Journal of Chemical Physics*, **22** (1954), 1255-1256.
[27] R.I. Feigin and D.H. Napper, Depletion stabilization and depletion flocculation, *Journal of Colloid and Interface Science*, **75** (1980), 525-541.
[28] B. Neu and H.J. Meiselman, Depletion-mediated red blood cell aggregation in polymer solutions, *Biophysical journal*, **83** (2002), 2482-2490.
[29] G. Tomaiuolo, M. Simeone, V. Martinelli, B. Rotoli and S. Guido, Red blood cell deformation in microconfined flow, *Soft Matter*, **5** (2009), 3736-3740.
[30] G. Tomaiuolo, Biomechanical properties of red blood cells in health and disease towards microfluidics, *Biomicrofluidics*, **8** (2014), 051501.
[31] P. Canham and A.C. Burton, Distribution of size and shape in populations of normal human red cells, *Circulation Research*, **22** (1968), 405-422.
[32] S. Guido and G. Tomaiuolo, Microconfined flow behavior of red blood cells in vitro, *Comptes Rendus Physique*, **10** (2009), 751-763.
[33] N. Mohandas and P.G. Gallagher, Red cell membrane: past, present, and future, *Blood*, **112** (2008), 3939-3948.
[34] J.H. Jeong, Y. Sugii, M. Minamiyama and K. Okamoto, Measurement of RBC deformation and velocity in capillaries in vivo, *Microvascular research*, **71** (2006), 212-217.

[35] G. Tomaiuolo, D. Rossi, S. Caserta, M. Cesarelli and S. Guido, Comparison of two flow-based imaging methods to measure individual red blood cell area and volume, *Cytometry Part A*, **81** (2012), 1040-1047.
[36] S.M. Hosseini and J.J. Feng, How malaria parasites reduce the deformability of infected red blood cells, *Biophysical journal*, **103** (2012), 1-10.
[37] L. Da Costa, J. Galimand, O. Fenneteau and N. Mohandas, Hereditary spherocytosis, elliptocytosis, and other red cell membrane disorders, *Blood reviews*, **27** (2013), 167-178.
[38] A. Marcinkowska-Gapińska, J. Gapinski, W. Elikowski, F. Jaroszyk and L. Kubisz, Comparison of three rheological models of shear flow behavior studied on blood samples from post-infarction patients, *Medical & biological engineering & computing*, **45** (2007), 837-844.
[39] A.J. Apostolidis and A.N. Beris, Modeling of the blood rheology in steady-state shear flows, *Journal of Rheology (1978-present)*, **58** (2014), 607-633.
[40] C. Picart, J.-M. Piau, H. Galliard and P. Carpentier, Human blood shear yield stress and its hematocrit dependence, *Journal of Rheology (1978-present)*, **42** (1998), 1-12.
[41] E. Merrill, E. Gilliland, G. Cokelet, H. Shin, A. Britten and R. Wells Jr, Rheology of human blood, near and at zero flow: effects of temperature and hematocrit level, *Biophysical Journal*, **3** (1963), 199.
[42] G.B. Thurston, Viscoelasticity of human blood, *Biophysical journal*, **12** (1972), 1205-1217.
[43] H.A. Barnes, Thixotropy—a review, *Journal of Non-Newtonian Fluid Mechanics*, **70** (1997), 1-33.
[44] A.M. Robertson, A. Sequeira and R.G. Owens, Rheological models for blood, in: *Cardiovascular mathematics*, Springer, 2009, pp. 211-241.
[45] T. Sochi, Non-Newtonian flow in porous media, *Polymer*, **51** (2010), 5007-5023.
[46] S. Chien, Shear dependence of effective cell volume as a determinant of blood viscosity, *Science*, **168** (1970), 977-979.
[47] A.M. Forsyth, J. Wan, P.D. Owrutsky, M. Abkarian and H.A. Stone, Multiscale approach to link red blood cell dynamics, shear viscosity, and ATP release, *Proceedings of the National Academy of Sciences*, **108** (2011), 10986-10991.
[48] L. Lanotte, J. Mauer, S. Mendez, D.A. Fedosov, J.-M. Fromental, V. Claveria, F. Nicoud, G. Gompper and M. Abkarian, Red cells' dynamic morphologies govern blood shear thinning under microcirculatory flow conditions, *Proceedings of the National Academy of Sciences* (2016), 201608074.
[49] E.W. Merrill, C.S. Cheng and G.A. Pelletier, Yield stress of normal human blood as a function of endogenous fibrinogen, *Journal of Applied Physiology*, **26** (1969), 1-3.
[50] J. Jung, B.-K. Lee and S. Shin, Yield shear stress and disaggregating shear stress of human blood, *Korea-Australia Rheology Journal*, **26** (2014), 191-198.
[51] N. Casson, *A flow equation for pigment-oil suspensions of the printing ink type*, Pergamon press, 1959.
[52] A. Gaspar-Rosas and G. Thurston, Erythrocyte aggregate rheology by transmitted and reflected light, *Biorheology*, **25** (1987), 471-487.

[53] F. Yilmaz and M.Y. Gundogdu, A critical review on blood flow in large arteries; relevance to blood rheology, viscosity models, and physiologic conditions, *Korea-Australia Rheology Journal*, **20** (2008), 197-211.
[54] S. Chien, R. King, R. Skalak, S. Usami and A. Copley, Viscoelastic properties of human blood and red cell suspensions, *Biorheology*, **12** (1975), 341-346.
[55] W.J. Drasler, C. Smith 2nd and K.H. Keller, Viscoelasticity of packed erythrocyte suspensions subjected to low amplitude oscillatory deformation, *Biophysical journal*, **52** (1987), 357.
[56] G.B. Thurston, Plasma release-cell layering theory for blood flow, *Biorheology*, **26** (1988), 199-214.
[57] M.M. Alves, C. Rocha and M.P. Gonçalves, Study of the rheological behaviour of human blood using a controlled stress rheometer, *Clinical hemorheology and microcirculation*, **53** (2013), 369-386.
[58] L. Campo-Deaño, R.P. Dullens, D.G. Aarts, F.T. Pinho and M.S. Oliveira, Viscoelasticity of blood and viscoelastic blood analogues for use in polydymethylsiloxane in vitro models of the circulatory system, *Biomicrofluidics*, **7** (2013), 034102.
[59] P. Sousa, J. Carneiro, R. Vaz, A. Cerejo, F. Pinho, M. Alves and M. Oliveira, Shear viscosity and nonlinear behavior of whole blood under large amplitude oscillatory shear, *Biorheology*, **50** (2013), 269-282.
[60] J.R. Levick, *An introduction to cardiovascular physiology*, Butterworth-Heinemann, 2013.
[61] E.N. Marieb and K. Hoehn, *Human anatomy & physiology*, Pearson Education, 2007.
[62] F.M. White, Fluid mechanics, WCB, *ed: McGraw-Hill, Boston* (1999).
[63] R. Lima, T. Ishikawa, Y. Imai and T. Yamaguchi, Blood flow behavior in microchannels: past, current and future trends, *Single and two-phase flows on chemical and biomedical engineering* (2012), 513-547.
[64] H. Bruus, Governing Equations in Microfluidics, (2014).
[65] H. Goldsmith and S. Mason, Axial migration of particles in Poiseuille flow, *Nature*, **190** (1961), 1095-1096.
[66] L. Bayliss, The axial drift of the red cells when blood flows in a narrow tube, *The Journal of physiology*, **149** (1959), 593-613.
[67] G. Mchedlishvili and N. Maeda, Blood Flow Structure Related to Red Cell Flow: A Determinant of Blood Fluidity in Narrow Microvessels, *The Japanese journal of physiology*, **51** (2001), 19-30.
[68] J.H. Barbee and G.R. Cokelet, The fahraeus effect, *Microvascular research*, **3** (1971), 6-16.
[69] R. Fåhraeus, The suspension stability of the blood, *Physiological Reviews*, **9** (1929), 241-274.
[70] A. Pries and T.W. Secomb, Rheology of the microcirculation, *Clinical hemorheology and microcirculation*, **29** (2003), 143-148.
[71] R. Fåhræus and T. Lindqvist, The viscosity of the blood in narrow capillary tubes, *American Journal of Physiology--Legacy Content*, **96** (1931), 562-568.

[72] A. Pries, D. Neuhaus and P. Gaehtgens, Blood viscosity in tube flow: dependence on diameter and hematocrit, *American Journal of Physiology-Heart and Circulatory Physiology*, **263** (1992), H1770-H1778.
[73] M. Toner and D. Irimia, Blood-on-a-chip., *Annu Rev Biomed Eng*, **7** (2005), 77-103.
[74] G.M. Whitesides, The origins and the future of microfluidics, *Nature*, **442** (2006), 368-373.
[75] M. Baker and H. Wayland, On-line volume flow rate and velocity profile measurement for blood in microvessels, *Microvascular research*, **7** (1974), 131-143.
[76] A.A. Parthasarathi, S.A. Japee and R.N. Pittman, Determination of red blood cell velocity by video shuttering and image analysis, *Annals of biomedical engineering*, **27** (1999), 313-325.
[77] S. Einav, H. Berman, R. Fuhro, P. DiGiovanni, S. Fine and J. Fridman, Measurement of velocity profiles of red blood cells in the microcirculation by laser doppler anemometry (LDA), *Biorheology*, **12** (1975), 207.
[78] Y. Sugii, R. Okuda, K. Okamoto and H. Madarame, Velocity measurement of both red blood cells and plasma of in vitro blood flow using high-speed micro PIV technique, *Measurement science and Technology*, **16** (2005), 1126.
[79] H. Golster, M. Lindén, S. Bertuglia, A. Colantuoni, G. Nilsson and F. Sjöberg, Red blood cell velocity and volumetric flow assessment by enhanced high-resolution laser Doppler imaging in separate vessels of the hamster cheek pouch microcirculation, *Microvascular research*, **58** (1999), 62-73.
[80] H. Goldsmith and J. Marlow, Flow behavior of erythrocytes. II. Particle motions in concentrated suspensions of ghost cells, *Journal of Colloid and Interface Science*, **71** (1979), 383-407.
[81] A. Nakano, Y. Sugii, M. Minamiyama and H. Niimi, Measurement of red cell velocity in microvessels using particle image velocimetry (PIV), *Clinical hemorheology and microcirculation*, **29** (2003), 445-455.
[82] A. Pries, T.W. Secomb, T. Gessner, M. Sperandio, J. Gross and P. Gaehtgens, Resistance to blood flow in microvessels in vivo, *Circulation research*, **75** (1994), 904-915.
[83] Y. Suzuki, N. Tateishi, M. Soutani and N. Maeda, Deformation of erythrocytes in microvessels and glass capillaries: effects of erythrocyte deformability, *Microcirculation*, **3** (1996), 49-57.
[84] J. Sherwood, J. Dusting, E. Kaliviotis and S. Balabani, The effect of red blood cell aggregation on velocity and cell-depleted layer characteristics of blood in a bifurcating microchannel, *Biomicrofluidics*, **6** (2012), 024119.
[85] A.R. Pries and T.W. Secomb, Microvascular blood viscosity in vivo and the endothelial surface layer, *American Journal of Physiology-Heart and Circulatory Physiology*, **289** (2005), H2657-H2664.
[86] C. Hahn and M.A. Schwartz, Mechanotransduction in vascular physiology and atherogenesis, *Nature reviews Molecular cell biology*, **10** (2009), 53-62.
[87] S. Kwei, G. Stavrakis, M. Takahas, G. Taylor, M.J. Folkman, M.A. Gimbrone and G. García-Cardeña, Early adaptive responses of the vascular wall during venous arterialization in mice, *The American journal of pathology*, **164** (2004), 81-89.

[88] B.L. Langille and F. O'Donnell, Reductions in arterial diameter produced by chronic decreases in blood flow are endothelium-dependent, *Science*, **231** (1986), 405-408.
[89] O. Traub and B.C. Berk, Laminar shear stress, *Arteriosclerosis, thrombosis, and vascular biology*, **18** (1998), 677-685.
[90] E.W. Young and C.A. Simmons, Macro-and microscale fluid flow systems for endothelial cell biology, *Lab on a Chip*, **10** (2010), 143-160.
[91] L.K. Fiddes, N. Raz, S. Srigunapalan, E. Tumarkan, C.A. Simmons, A.R. Wheeler and E. Kumacheva, A circular cross-section PDMS microfluidics system for replication of cardiovascular flow conditions, *Biomaterials*, **31** (2010), 3459-3464.
[92] L.-M. Li, X.-Y. Wang, L.-S. Hu, R.-S. Chen, Y. Huang, S.-J. Chen, W.-H. Huang, K.-F. Huo and P.K. Chu, Vascular lumen simulation and highly-sensitive nitric oxide detection using three-dimensional gelatin chip coupled to TiC/C nanowire arrays microelectrode, *Lab on a Chip*, **12** (2012), 4249-4256.
[93] A.D. Wong and P.C. Searson, Live-cell imaging of invasion and intravasation in an artificial microvessel platform, *Cancer research*, **74** (2014), 4937-4945.
[94] G. Lamberti, B. Prabhakarpandian, C. Garson, A. Smith, K. Pant, B. Wang and M.F. Kiani, Bioinspired microfluidic assay for in vitro modeling of leukocyte–endothelium interactions, *Analytical chemistry*, **86** (2014), 8344-8351.
[95] M.D. Mager, V. LaPointe and M.M. Stevens, Exploring and exploiting chemistry at the cell surface, *Nature Chemistry*, **3** (2011), 582-589.
[96] J. Tarbell and L. Cancel, The glycocalyx and its significance in human medicine, *Journal of internal medicine* (2016).
[97] D.L. Cioffi, S. Pandey, D.F. Alvarez and E.A. Cioffi, Terminal sialic acids are an important determinant of pulmonary endothelial barrier integrity, *American Journal of Physiology-Lung Cellular and Molecular Physiology*, **302** (2012), L1067-L1077.
[98] S. Kelm and R. Schauer, Sialic acids in molecular and cellular interactions, *International review of cytology*, **175** (1997), 137-240.
[99] A. Pries, T. Secomb and P. Gaehtgens, The endothelial surface layer, *Pflügers Archiv*, **440** (2000), 653-666.
[100] M.J. Mitchell and M.R. King, Physical biology in cancer. 3. The role of cell glycocalyx in vascular transport of circulating tumor cells, *American Journal of Physiology-Cell Physiology*, **306** (2014), C89-C97.
[101] J.C. Rutledge, K.F. Ng, H.H. Aung and D.W. Wilson, Role of triglyceride-rich lipoproteins in diabetic nephropathy, *Nature Reviews Nephrology*, **6** (2010), 361-370.
[102] Y. Han, S. Weinbaum, J.A. Spaan and H. Vink, Large-deformation analysis of the elastic recoil of fibre layers in a Brinkman medium with application to the endothelial glycocalyx, *Journal of Fluid Mechanics*, **554** (2006), 217-235.
[103] S. Reitsma, D.W. Slaaf, H. Vink, M.A. van Zandvoort and M.G. oude Egbrink, The endothelial glycocalyx: composition, functions, and visualization, *Pflügers Archiv-European Journal of Physiology*, **454** (2007), 345-359.
[104] S. Weinbaum, X. Zhang, Y. Han, H. Vink and S.C. Cowin, Mechanotransduction and flow across the endothelial glycocalyx, *Proceedings of the National Academy of Sciences*, **100** (2003), 7988-7995.

[105] A.H. Salmon and S.C. Satchell, Endothelial glycocalyx dysfunction in disease: albuminuria and increased microvascular permeability, *The Journal of pathology*, **226** (2012), 562-574.
[106] T. Secomb, R. Hsu and A. Pries, Effect of the endothelial surface layer on transmission of fluid shear stress to endothelial cells, *Biorheology*, **38** (2001), 143-150.
[107] T. Secomb, R. Hsu and A. Pries, Blood flow and red blood cell deformation in nonuniform capillaries: effects of the endothelial surface layer, *Microcirculation*, **9** (2002), 189-196.
[108] J. Zhang, P.C. Johnson and A.S. Popel, Effects of erythrocyte deformability and aggregation on the cell free layer and apparent viscosity of microscopic blood flows, *Microvascular research*, **77** (2009), 265-272.
[109] M. Liu and J. Yang, Electrokinetic effect of the endothelial glycocalyx layer on two-phase blood flow in small blood vessels, *Microvascular research*, **78** (2009), 14-19.
[110] L. Lanotte, G. Tomaiuolo, C. Misbah, L. Bureau and S. Guido, Red blood cell dynamics in polymer brush-coated microcapillaries: A model of endothelial glycocalyx in vitro, *Biomicrofluidics*, **8** (2014), 014104.
[111] S. Suresh, J. Spatz, J.P. Mills, A. Micoulet, M. Dao, C.T. Lim, M. Beil and T. Seufferlein, Connections between single-cell biomechanics and human disease states: gastrointestinal cancer and malaria, *Acta Biomaterialia*, **1** (2005), 15-30.
[112] A.M. Dondorp, P.A. Kager, J. Vreeken and N.J. White, Abnormal blood flow and red blood cell deformability in severe malaria, *Parasitology Today*, **16** (2000), 228-232.
[113] L.H. Miller, D.I. Baruch, K. Marsh and O.K. Doumbo, The pathogenic basis of malaria, *Nature*, **415** (2002), 673-679.
[114] S. Bhatt, D. Weiss, E. Cameron, D. Bisanzio, B. Mappin, U. Dalrymple, K. Battle, C. Moyes, A. Henry and P. Eckhoff, The effect of malaria control on Plasmodium falciparum in Africa between 2000 and 2015, *Nature*, **526** (2015), 207-211.
[115] L.H. Miller, H.C. Ackerman, X.-z. Su and T.E. Wellems, Malaria biology and disease pathogenesis: insights for new treatments, *Nature medicine*, **19** (2013), 156-167.
[116] T. Smith, A. Ross, N. Maire, N. Chitnis, A. Studer, D. Hardy, A. Brooks, M. Penny and M. Tanner, Ensemble modeling of the likely public health impact of a pre-erythrocytic malaria vaccine, *PLoS Med*, **9** (2012), e1001157.
[117] A.J. Crick, M. Theron, T. Tiffert, V.L. Lew, P. Cicuta and J.C. Rayner, Quantitation of malaria parasite-erythrocyte cell-cell interactions using optical tweezers, *Biophysical journal*, **107** (2014), 846-853.
[118] G.A. Josling and M. Llinás, Sexual development in Plasmodium parasites: knowing when it's time to commit, *Nature Reviews Microbiology*, **13** (2015), 573-587.
[119] A.F. Cowman and B.S. Crabb, Invasion of red blood cells by malaria parasites, *Cell*, **124** (2006), 755-766.
[120] A.G. Craig, M.F.M. Khairul and P.R. Patil, Cytoadherence and severe malaria, (2012).
[121] C.R. Engwerda, L. Beattie and F.H. Amante, The importance of the spleen in malaria, *Trends in parasitology*, **21** (2005), 75-80.

[122] G. Nash, E. O'Brien, E. Gordon-Smith and J. Dormandy, Abnormalities in the mechanical properties of red blood cells caused by Plasmodium falciparum, *Blood*, **74** (1989), 855-861.
[123] A. Dondorp, M. Nyanoti, P. Kager, S. Mithwani, J. Vreeken and K. Marsh, The role of reduced red cell deformability in the pathogenesis of severe falciparum malaria and its restoration by blood transfusion, *Transactions of the Royal Society of Tropical Medicine and Hygiene*, **96** (2002), 282-286.
[124] H. Armah, E.K. Wiredu, A.K. Dodoo, A.A. Adjei, Y. Tettey and R. Gyasi, Cytokines and adhesion molecules expression in the brain in human cerebral malaria, *International journal of environmental research and public health*, **2** (2005), 123-131.
[125] L.B. Ochola, B.R. Siddondo, H. Ocholla, S. Nkya, E.N. Kimani, T.N. Williams, J.O. Makale, A. Liljander, B.C. Urban and P.C. Bull, Specific receptor usage in Plasmodium falciparum cytoadherence is associated with disease outcome, *PloS one*, **6** (2011), e14741.
[126] A.L. Conroy, H. Phiri, M. Hawkes, S. Glover, M. Mallewa, K.B. Seydel, T.E. Taylor, M.E. Molyneux and K.C. Kain, Endothelium-based biomarkers are associated with cerebral malaria in Malawian children: a retrospective case-control study, *PLoS One*, **5** (2010), e15291.
[127] S.J. Chakravorty, K.R. Hughes and A.G. Craig, Host response to cytoadherence in Plasmodium falciparum, Portland Press Limited, 2008.
[128] I.M. Francischetti, Does activation of the blood coagulation cascade have a role in malaria pathogenesis?, *Trends in parasitology*, **24** (2008), 258-263.
[129] I.M. Francischetti, K.B. Seydel, R.Q. Monteiro, R.O. Whitten, C.R. Erexson, A.L. Noronha, G.R. Ostera, S.B. Kamiza, M.E. Molyneux and J.M. Ward, Plasmodium falciparum-infected erythrocytes induce tissue factor expression in endothelial cells and support the assembly of multimolecular coagulation complexes, *Journal of Thrombosis and Haemostasis*, **5** (2007), 155-165.
[130] G. MacPherson, M. Warrell, N. White, S. Looareesuwan and D. Warrell, Human cerebral malaria. A quantitative ultrastructural analysis of parasitized erythrocyte sequestration, *The American journal of pathology*, **119** (1985), 385.
[131] A.M. Vogt, A. Barragan, Q. Chen, F. Kironde, D. Spillmann and M. Wahlgren, Heparan sulfate on endothelial cells mediates the binding ofPlasmodium falciparum–infected erythrocytes via the DBL1α domain of PfEMP1, *Blood*, **101** (2003), 2405-2411.
[132] R.P. McEver and C. Zhu, Rolling cell adhesion, *Annual review of cell and developmental biology*, **26** (2010), 363-396.
[133] G. Helms, A.K. Dasanna, U.S. Schwarz and M. Lanzer, Modeling cytoadhesion of Plasmodium falciparum-infected erythrocytes and leukocytes—common principles and distinctive features, *FEBS letters*, **590** (2016), 1955-1971.
[134] D.A. Fedosov, B. Caswell and G.E. Karniadakis, Wall shear stress-based model for adhesive dynamics of red blood cells in malaria, *Biophysical journal*, **100** (2011), 2084-2093.
[135] D. Fedosov, B. Caswell, S. Suresh and G. Karniadakis, Quantifying the biophysical characteristics of Plasmodium-falciparum-parasitized red blood cells in microcirculation, *Proceedings of the National Academy of Sciences*, **108** (2011), 35-39.

[136] D.A. Fedosov, H. Lei, B. Caswell, S. Suresh and G.E. Karniadakis, Multiscale modeling of red blood cell mechanics and blood flow in malaria, *PLoS Comput Biol*, **7** (2011), e1002270.
[137] M. Ho, M.J. Hickey, A.G. Murray, G. Andonegui and P. Kubes, Visualization of Plasmodium falciparum–Endothelium Interactions in Human Microvasculature, *Journal of experimental medicine*, **192** (2000), 1205-1212.
[138] M. Antia, T. Herricks and P.K. Rathod, Microfluidic Modeling of Cell− Cell Interactions in Malaria Pathogenesis, *PLoS Pathog*, **3** (2007), e99.
[139] C. Hempel, E.M. Pasini and J.A. Kurtzhals, Endothelial Glycocalyx: Shedding Light on Malaria Pathogenesis, *Trends in molecular medicine*, **22** (2016), 453-457.
[140] S.J. Rogerson, S.C. Chaiyaroj, K. Ng, J.C. Reeder and G.V. Brown, Chondroitin sulfate A is a cell surface receptor for Plasmodium falciparum-infected erythrocytes, *Journal of Experimental Medicine*, **182** (1995), 15-20.
[141] A. Dietmann, R. Helbok, P. Lackner, S. Issifou, B. Lell, P.-B. Matsiegui, M. Reindl, E. Schmutzhard and P.G. Kremsner, Matrix metalloproteinases and their tissue inhibitors (TIMPs) in Plasmodium falciparum malaria: serum levels of TIMP-1 are associated with disease severity, *Journal of Infectious Diseases*, **197** (2008), 1614-1620.
[142] O.K. Baskurt, M. Boynard, G.C. Cokelet, P. Connes, B.M. Cooke, S. Forconi, F. Liao, M.R. Hardeman, F. Jung and H.J. Meiselman, New guidelines for hemorheological laboratory techniques, *Clinical hemorheology and microcirculation*, **42** (2009), 75-97.
[143] P. Snabre and P. Mills, II. Rheology of weakly flocculated suspensions of viscoelastic particles, *Journal de Physique III*, **6** (1996), 1835-1855.
[144] A. Robertson, A. Sequeira and R. Owens, Rheological models for blood, in: *Cardiovascular Mathematics*, L. Formaggia, A. Quarteroni and A. Veneziani, edsVol. 1, Springer Milan, 2009, pp. 211-241.
[145] S. Chien, S. Usami, H.M. Taylor, J.L. Lundberg and M.I. Gregersen, Effects of hematocrit and plasma proteins on human blood rheology at low shear rates, *Journal of Applied Physiology*, **21** (1966), 81-87.
[146] D.A. Fedosov, W. Pan, B. Caswell, G. Gompper and G.E. Karniadakis, Predicting human blood viscosity in silico, *Proceedings of the National Academy of Sciences*, **108** (2011), 11772-11777.
[147] S.S. Datta, D.D. Gerrard, T.S. Rhodes, T.G. Mason and D.A. Weitz, Rheology of attractive emulsions, *Physical Review E*, **84** (2011), 041404.
[148] V. Trappe and D.A. Weitz, Scaling of the Viscoelasticity of Weakly Attractive Particles, *Physical Review Letters*, **85** (2000), 449-452.
[149] T.G. Mason, Estimating the viscoelastic moduli of complex fluids using the generalized Stokes–Einstein equation, *Rheologica Acta*, **39** (2000), 371-378.
[150] G.B. Thurston, Elastic effects in pulsatile blood flow, *Microvascular Research*, **9** (1975), 145-157.
[151] T.L. Fabry, Mechanism of erythrocyte aggregation and sedimentation., *Blood*, **70** (1987), 1572-1576.
[152] P. Gaehtgens, Distribution of flow and red cell flux in the microcirculation, *Scandinavian Journal of Clinical and Laboratory Investigation*, **41** (1981), 83-87.

[153] H.C. Kwaan and J. Wang, Hyperviscosity in polycythemia vera and other red cell abnormalities, *Seminars in thrombosis and hemostasis*, **29** (2003), 451-458.
[154] S. Sarkar and T.S. Rosenkrantz, Neonatal polycythemia and hyperviscosity, *Seminars in Fetal and Neonatal Medicine*, **13** (2008), 248-255.
[155] B.D. Adams, R. Baker, J.A. Lopez and S. Spencer, Myeloproliferative Disorders and the Hyperviscosity Syndrome, *Hematology/Oncology Clinics of North America*, **24** (2010), 585-602.
[156] H.-J. Lim, J.-H. Nam, B.-K. Lee, J.-S. Suh and S. Shin, Alteration of red blood cell aggregation during blood storage, *Korea-Australia Rheology Journal*, **23** (2011), 67-70.
[157] U. Kirkpatrick, R. Adams, A. Lardi and C. McCollum, Rheological properties and function of blood cells in stored bank blood and salvaged blood, *British journal of haematology*, **101** (1998), 364-368.
[158] A. Zydney, J. Oliver III and C. Colton, A constitutive equation for the viscosity of stored red cell suspensions: Effect of hematocrit, shear rate, and suspending phase, *Journal of Rheology (1978-present)*, **35** (1991), 1639-1680.
[159] R.B. Ami, G. Barshtein, D. Zeltser, Y. Goldberg, I. Shapira, A. Roth, G. Keren, H. Miller, V. Prochorov and A. Eldor, Parameters of red blood cell aggregation as correlates of the inflammatory state, *American Journal of Physiology-Heart and Circulatory Physiology*, **280** (2001), H1982-H1988.
[160] W.J. Drasler, C.M. Smith, 2nd and K.H. Keller, Viscoelasticity of packed erythrocyte suspensions subjected to low amplitude oscillatory deformation, *Biophys J*, **52** (1987), 357-365.
[161] R. Tran-Son-Tay, S.P. Sutera and P.R. Rao, Determination of red blood cell membrane viscosity from rheoscopic observations of tank-treading motion, *Biophysical Journal*, **46** (1984), 65-72.
[162] Y.Z. Yoon, J. Kotar, G. Yoon and P. Cicuta, The nonlinear mechanical response of the red blood cell, in: *Phys Biol*Vol. 5, England, 2008, p. 036007.
[163] T.G. Papaioannou and C. Stefanadis, Vascular wall shear stress: basic principles and methods, *Hellenic J Cardiol*, **46** (2005), 9-15.
[164] A.L. Barker, O. Konopatskaya, C.R. Neal, J.V. Macpherson, J.L. Whatmore, C.P. Winlove, P.R. Unwin and A.C. Shore, Observation and characterisation of the glycocalyx of viable human endothelial cells using confocal laser scanning microscopy, *Physical chemistry chemical physics*, **6** (2004), 1006-1011.
[165] A. Ishibazawa, T. Nagaoka, T. Takahashi, K. Yamamoto, A. Kamiya, J. Ando and A. Yoshida, Effects of shear stress on the gene expressions of endothelial nitric oxide synthase, endothelin-1, and thrombomodulin in human retinal microvascular endothelial cells, *Investigative ophthalmology & visual science*, **52** (2011), 8496-8504.
[166] M.B. Simmers, A.W. Pryor and B.R. Blackman, Arterial shear stress regulates endothelial cell-directed migration, polarity, and morphology in confluent monolayers, *American Journal of Physiology-Heart and Circulatory Physiology*, **293** (2007), H1937-H1946.
[167] H. Kataoka, A. Ushiyama, H. Kawakami, Y. Akimoto, S. Matsubara and T. Iijima, Fluorescent imaging of endothelial glycocalyx layer with wheat germ agglutinin using intravital microscopy, *Microscopy research and technique*, **79** (2016), 31-37.

[168] D.R. Potter and E.R. Damiano, The hydrodynamically relevant endothelial cell glycocalyx observed in vivo is absent in vitro, *Circulation research*, **102** (2008), 770-776.
[169] D. Chappell, M. Jacob, O. Paul, M. Rehm, U. Welsch, M. Stoeckelhuber, P. Conzen and B.F. Becker, The Glycocalyx of the Human Umbilical Vein Endothelial Cell, *Circulation research*, **104** (2009), 1313-1317.
[170] E.E. Ebong, F.P. Macaluso, D.C. Spray and J.M. Tarbell, Imaging the endothelial glycocalyx in vitro by rapid freezing/freeze substitution transmission electron microscopy, *Arteriosclerosis, thrombosis, and vascular biology*, **31** (2011), 1908-1915.
[171] M. Urushidani, Y. Sugii, K. Mogi and K. Hishida, Investigation of Near Surface Flow Field and Glycocalyx Dimension of Endothelial Cells by Confocal Micro-PIV and Super-Resolution Microscopy, in: *Proceedings of the 17th International Symposium on Applications of Laser Techniques to Fluid Mechanics, Lisbon, Portugal*, 2014, pp. 7-10.
[172] Y.-c. Fung, *Biomechanics: circulation*, Springer, 1997.
[173] A.J. Crick, T. Tiffert, S.M. Shah, J. Kotar, V.L. Lew and P. Cicuta, An automated live imaging platform for studying merozoite egress-invasion in malaria cultures, *Biophysical journal*, **104** (2013), 997-1005.
[174] T. Tiffert, H. Ginsburg, M. Krugliak, B.C. Elford and V.L. Lew, Potent antimalarial activity of clotrimazole in in vitro cultures of Plasmodium falciparum, *Proceedings of the National Academy of Sciences*, **97** (2000), 331-336.
[175] B. Rosental, U. Hadad, R. Sinay, A. Braiman, A. Porgador and Y. Pollack, Dual fluorescent labelling of the human malaria parasite Plasmodium falciparum for the analysis of the ABC type transporter pfmdr2, *Malaria journal*, **11** (2012), 371.
[176] X.Y. Yam, T. Brugat, A. Siau, J. Lawton, D.S. Wong, A. Farah, J.S. Twang, X. Gao, J. Langhorne and P.R. Preiser, Characterization of the Plasmodium Interspersed Repeats (PIR) proteins of Plasmodium chabaudi indicates functional diversity, *Scientific reports*, **6** (2016).
[177] L.M. Coronado, C.T. Nadovich and C. Spadafora, Malarial hemozoin: from target to tool, *Biochimica et Biophysica Acta (BBA)-General Subjects*, **1840** (2014), 2032-2041.
[178] M. Olivier, K. Van Den Ham, M.T. Shio, F.A. Kassa and S. Fougeray, Malarial pigment hemozoin and the innate inflammatory, (2014).
[179] G. Silva, V. Jeney, Â. Chora, R. Larsen, J. Balla and M.P. Soares, Oxidized hemoglobin is an endogenous proinflammatory agonist that targets vascular endothelial cells, *Journal of Biological Chemistry*, **284** (2009), 29582-29595.
[180] X. Liu and Z. Spolarics, Methemoglobin is a potent activator of endothelial cells by stimulating IL-6 and IL-8 production and E-selectin membrane expression, *American Journal of Physiology-Cell Physiology*, **285** (2003), C1036-C1046.
[181] S. Balaji and V. Trivedi, Extracellular methemoglobin primes red blood cell aggregation in malaria: an in vitro mechanistic study, *FEBS letters*, **587** (2013), 350-357.
[182] H. Oberleithner, M. Wälte and K. Kusche-Vihrog, Sodium renders endothelial cells sticky for red blood cells, *Frontiers in physiology*, **6** (2015), 188.

[183] O.K. Baskurt, Pathophysiological significance of blood rheology, *Turkish Journal of Medical Sciences*, **33** (2003), 347-355.
[184] G.D. Lowe, Rheological influences on thrombosis, *Best Practice & Research Clinical Haematology*, **12** (1999), 435-449.
[185] G. Lowe, A. Lee, A. Rumley, J. Price and F. Fowkes, Blood viscosity and risk of cardiovascular events: the Edinburgh Artery Study, *British journal of haematology*, **96** (1997), 168-173.
[186] R.L. Letcher, S. Chien, T.G. Pickering, J.E. Sealey and J.H. Laragh, Direct relationship between blood pressure and blood viscosity in normal and hypertensive subjects: role of fibrinogen and concentration, *The American journal of medicine*, **70** (1981), 1195-1202.
[187] R. Jay, S. Jones, C. Hill, W. Richmond, G. Viberti, M. Rampling and D. Betteridge, Blood rheology and cardiovascular risk factors in type 1 diabetes: relationship with microalbuminuria, *Diabetic medicine*, **8** (1991), 662-667.
[188] J.G. Wetmur and J. Fresco, DNA probes: applications of the principles of nucleic acid hybridization, *Critical reviews in biochemistry and molecular biology*, **26** (1991), 227-259.
[189] H.A. Stone, A.D. Stroock and A. Ajdari, Engineering flows in small devices: microfluidics toward a lab-on-a-chip, *Annu. Rev. Fluid Mech.*, **36** (2004), 381-411.
[190] A. Halperin, A. Buhot and E. Zhulina, Hybridization at a surface: the role of spacers in DNA microarrays, *Langmuir*, **22** (2006), 11290-11304.
[191] N. Zammatteo, L. Jeanmart, S. Hamels, S. Courtois, P. Louette, L. Hevesi and J. Remacle, Comparison between different strategies of covalent attachment of DNA to glass surfaces to build DNA microarrays, *Analytical biochemistry*, **280** (2000), 143-150.
[192] J. Sobek, C. Aquino, W. Weigel and R. Schlapbach, Drop drying on surfaces determines chemical reactivity-the specific case of immobilization of oligonucleotides on microarrays, *BMC biophysics*, **6** (2013), 8.
[193] Y.-H. Rogers, P. Jiang-Baucom, Z.-J. Huang, V. Bogdanov, S. Anderson and M.T. Boyce-Jacino, Immobilization of oligonucleotides onto a glass support via disulfide bonds: a method for preparation of DNA microarrays, *Analytical biochemistry*, **266** (1999), 23-30.
[194] B. Joos, H. Kuster and R. Cone, Covalent attachment of hybridizable oligonucleotides to glass supports, *Analytical biochemistry*, **247** (1997), 96-101.
[195] F. Fixe, M. Dufva, P. Telleman and C.B.V. Christensen, One-step immobilization of aminated and thiolated DNA onto poly (methylmethacrylate)(PMMA) substrates, *Lab on a Chip*, **4** (2004), 191-195.

Appendix B

Publications:

- Roberta Liuzzi, **Antonio Carciati**, Flora Ascione, Antonio Magliocca, Livia Guadagno, Sergio Caserta, Pasquale Abete, Stefano Guido. "Interactions between microstructured fluids and *stratum corneum*: pharmaceutical and cosmetic applications". International Journal of Cosmetic Science 37.1 (2015): 156-157.
- Roberta Liuzzi, **Antonio Carciati**, Sergio Caserta and Stefano Guido. "Transport efficiency in transdermal drug delivery: What is the role of fluid microstructure?" Colloids and Surfaces B: Biointerfaces 139 (2016): 294-305.
- Giovanna Tomaiuolo, **Antonio Carciati**, Sergio Caserta and Stefano Guido. "Blood linear viscoelasticity by small amplitude oscillatory flow" Rheologica Acta (2016) 55: 485.

Experiences in foreign laboratories

Visiting student research collaborator (VSRC) at University of Cambridge, Cavendish Laboratories (Prof. Pietro Cicuta). *Blood on chip for biomedical applications*, (04/08/2016 – 08/11/2016).

Conferences

- Cosminnov Cosmetic Innovation Days, Orlèans (France), 8-9/10/2013.
- 9th Annual European Rheology Conference (AERC) 2014, Nantes (France), 8-11/04/2014.
- XIII National Convention of the Italian Rheology society (SIR) - Keynote, Brescia (Italy), 7-9/09/2014.
- Stratum Corneum VIII, Cardiff (UK), 17-19/09/2014.
- Italian Soft Days, Rome (Italy), 17-18/09/2014.
- Society of Rheology (SOR) - 86th Annual Meeting, Philadelphia (USA), 5-9/10/2014.
- National Convention of the Italian Gereontology and Geriatrics (SIGG), Bologna (Italy), 26-29/11/2014.
- Smart & Green Interfaces Conference (SGIC), COST ACTION MP1106, Belgrade (Serbia), 30-01/04/2015.
- 10th Annual European Rheology Conference (AERC) 2015, Nantes (France), 14-17/04/2015.
- 15th European Colloid Student Conference (ECIS), Krakow (Poland), 8-11/06/2015.
- Smart & Green Interfaces Conference (SGIC), COST ACTION MP1106, Athens (Greece), 4-6/05/2016.

- XIV National convention of the Italian Rheology Society (SIR), Montepaone Lido (Italy), 1-4/6/2016.
- GRICU Meeting, Anacapri (Italy) 12-14/09/2016.